

UNIVERSITÀ DEGLI STUDI DI PADOVA

SCUOLA DI DOTTORATO DI RICERCA IN INGEGNERIA

INDUSTRIALE CURRICULUM ENERGIA

CICLO XXVII

Analysis, Design and Optimization

of Innovative Electrical Machines

Using Analytical and Finite Element Analysis Methods

DOTTORANDO

Michele Degano

DIRETTORE DELLA SCUOLA

Chiar.mo Prof. Paolo Colombo

COORDINATORE DEL COLLEGIO DOCENTI

Chiar.ma Prof.ssa Luisa Rossetto

SUPERVISORE DI TESI

Chiar.mo Prof. Alberto Tassarolo

CO-SUPERVISORE DI TESI

Chiar.mo Prof. Nicola Bianchi

ANNO 2014

**Analysis, design and optimization of innovative electrical
machines using Analytical and Finite Element Analysis
Method**

By

Michele Degano

Dissertation

Submitted in Partial Fulfillment of the Requirements
for the Degree of Doctor of Philosophy
in Industrial Engineering
at Department of Electrical Engineering
Padova University, 2014
Padova, Veneto, Italy

Contents

Introduzione	1
Preface	5
I Design and Optimization Techniques for PMASynRel motors	11
1 Synchronous Reluctance and Permanent Magnet Assisted Reluctance Machine	13
1.1 Background	13
1.2 Synchronous Reluctance Machine	14
1.3 Permanent Magnet Assisted Synchronous Reluctance Machine	15
1.4 Application fields	16
1.5 Basic principles	18
1.5.1 Iron saturation effect	19
2 Electric Motor Requirements and Design for Traction Application	21
2.1 Preliminary analysis and design considerations	21
2.2 IPM motors: design and analysis	22
2.3 Comparison to SPM motors	26
2.4 Electric drive	28
2.5 Conclusions	31
3 PM Volume Dimensioning in Permanent Magnet Assisted Synchronous Reluctance Motors	33
3.1 Design procedure overview	33
3.2 Analysis of the performance	35
3.3 Conclusions	37
4 Sensitivity Analysis of Torque Ripple Reduction of Synchronous Re- luctance and Interior PM Motors	39
4.1 A brief review of techniques to reduce torque ripple of SynREL and IPM machines	39
4.1.1 Reference geometries	40
4.1.2 Validation by means of experimental results	42

4.2	Analysis of torque ripple	43
4.3	Optimized Reluctance Machines under analysis	47
4.3.1	Torque ripple sensitivity	49
4.4	Sensitivity of the optimal solution	51
4.5	Effect of the PM on torque ripple	52
4.6	Conclusions	54
5	Robust Optimization of a Traction PMASR Motor According to Given Driving Cycles	55
5.1	Evaluation of the motor requirements	56
5.1.1	Driving cycles	56
5.1.2	Torque and power distributions	56
5.2	Design and optimization	57
5.2.1	Pre-optimization analysis	58
5.2.2	Optimization procedure	61
5.2.3	Evaluation of the robustness	62
5.2.4	Results	62
5.3	Conclusions	64
6	PM Synchronous Machine Comparison for Light Electric Vehicles	67
6.1	Introduction	67
6.2	Machine Design and Optimization	68
6.3	Comparison of the topologies	70
6.3.1	Constant torque capability	71
6.3.2	Flux weakening capability	72
6.3.3	Losses and efficiency	73
6.3.4	Economical comparison	74
6.3.5	Overview of the electric supply system	75
6.4	Conclusions	77
7	Synchronous Reluctance and PM Assisted Reluctance Motors for Wash- ing Machines Application	79
7.1	Introduction	79
7.2	Machine Design and Optimization	81
7.2.1	Electric motor requirements	81
7.2.2	SynRel motor design and optimization	83
7.2.3	SynRel motor performance	84
7.2.4	Introduction of ferrite PMs in the rotor flux barriers	87
II	Synchronous Reluctance Machine: Analytical Modeling	91
8	On the Analytical Estimation of the Airgap Field in Synchronous Re- luctance Machine	93
8.1	Modeling Assumption	94
8.2	Computing Stator Magneto Motive Force	95

8.3	Modeling of SynRel Motor Through Reluctance Networks	95
8.4	Computation of Reluctance Network Parameters	98
8.5	Airgap Flux Density Computation From Reluctance Network Solution	99
8.6	Validation by Finite Element Analysis	101
8.7	Conclusions	103
9	Analytical Modeling of Split-Phase Synchronous Reluctance Machines	105
9.1	Modeling Assumption	106
9.2	Motor Modeling with MEC Technique	109
9.3	Computation of Air-gap MMF Sources	110
9.4	Computation of Air-gap and Barrier Reluctances	112
9.4.1	Air-gap reluctances	112
9.4.2	Flux barrier reluctance	112
9.5	Computation of Air-gap Flux	115
9.6	Assessment Against FEA Simulation	115
9.7	Conclusions	117
III	Prototypes and Experimental Results	119
	References	121

Introduzione

In questi ultimi anni l'interesse per le macchine elettriche rotanti facenti uso di magneti permanenti ha riscontrato uno sviluppo sempre più crescente. Tali macchine rappresentano un mondo alternativo alle tradizionali macchine sincrone e ad induzione, e vengono considerate ad oggi soluzioni promettenti in svariati settori, come quello industriale, per il trasporto, come attuatori, elettrodomestici e per l'impiego in impianti di potenza.

I problemi legati all'aumento della domanda di energia elettrica ed al suo consumo, hanno generato una tendenza alla ricerca di azionamenti ad alta efficienza, spingendo la tecnologia delle macchine elettriche classiche ad ulteriori miglioramenti. L'introduzione dei magneti permanenti che utilizzano terre rare, già dagli anni 60, hanno incentivato e permesso lo sviluppo di diversi tipi di macchina innovativi. Tuttavia, l'aumento e l'instabilità del prezzo delle terre rare, tra il 2010 ed il 2013, ha diretto la ricerca verso soluzioni di macchine alternative senza magneti permanenti, o con una quantità ridotta di tali materiali, pur soddisfacendo le specifiche di progetto.

Al momento, la ricerca industriale e quella accademica sono entrambe focalizzate allo sviluppo di motori e generatori elettrici con elevate prestazioni, tra i diversi tipi di macchine elettriche esistenti, i motori sincroni a riluttanza (SynRel) ed a riluttanza assistita da magneti permanenti (PMASynRel) risultano essere degli ottimi candidati per il soddisfacimento delle specifiche energetiche e di efficienza, sempre più stringenti, che verranno richieste ai motori nel prossimo futuro.

Questo lavoro di tesi è interamente dedicato all'analisi teorica e sperimentale ed alla progettazione di motori sincroni a riluttanza (SynRel) e motori sincroni a riluttanza assistita da magneti permanenti (PMASynRel). In particolare, l'attenzione sarà posta su macchine elettriche in un campo di potenza che varia dalle centinaia di Watt alle decine di kiloWatt, principalmente per applicazioni come veicoli elettrici ed elettrodomestici.

Tali macchine presentano una serie di vantaggi tecnologici che le portano ad avere prestazioni, soprattutto nel campo degli azionamenti a velocità variabile (VSD), competitive rispetto ad esempio alle macchine ad induzione tradizionali o quelle a magneti permanenti.

La struttura semplice e robusta, l'utilizzo ridotto di magneti permanenti, i gradi di libertà nella progettazione combinate ad un'elevata densità di coppia, alta efficienza,

elevate caratteristiche di sovraccarico ed un ampio campo di velocità, sono tutte caratteristiche che hanno permesso di collocare le macchine SynRel e PMASynRel in una posizione di rilievo. Inoltre, grazie all'aumento dei convertitori moderni a frequenza variabile e sistemi di controllo digitale, le prestazioni di questo tipo di motori, in termini di coppia ed efficienza, sono diventate altamente competitive rispetto ai tradizionali azionamenti con motori ad induzione.

Gli argomenti trattati nell'elaborato di tesi sono organizzati in tre parti, ognuna composta da diversi capitoli.

La **Parte I** è composta da sette capitoli che riassumono parte delle attività di ricerca scientifica condotte durante il corso del periodo di dottorato. I primi sei capitoli saranno dedicati principalmente a macchine elettriche per veicoli da trazione, mentre il capitolo settimo, non meno importante, tratterà motori per applicazioni elettrodomestiche.

Il **Capitolo 1** di carattere introduttivo, ha lo scopo di fornire le informazioni base per la comprensione delle caratteristiche e dei vantaggi e svantaggi delle macchine oggetto di questo studio.

Nel **Capitolo 2** verranno determinati e riassunti i criteri di progetto e le specifiche elettriche dei motori SynRel e PMASynRel per applicazioni veicolari a trazione elettrica. Le prestazioni elettromeccaniche sono state valutate e confrontate, in termini di potenza e coppia, su diverse tipologie di motori. Seguirà una breve descrizione del sistema di alimentazione adatto all'applicazione che ha lo scopo di gestire efficientemente il motore al fine di soddisfare le prestazioni richieste.

Il **Capitolo 3** mette in luce l'influenza ed i benefici dell'utilizzo di magneti permanenti in ferrite sulle prestazioni delle macchine a riluttanza. Nel dettaglio, verrà evidenziata l'importanza di una valutazione attenta della quantità di magneti da utilizzare con il duplice scopo di migliorare le prestazioni e la coppia del motore.

Il **Capitolo 4** è dedicato all'analisi parametrica dei motori SynRel e PMASynRel, al fine di comprendere quali e come le variabili geometriche di progetto influenzano le prestazioni delle macchine, in particolare il loro effetto sulle oscillazioni di coppia (torque ripple). Un algoritmo di ottimizzazione ha permesso di investigare e determinare una geometria rotorica che massimizza la coppia elettromagnetica fornita dal motore e ne minimizza le pulsazioni di coppia. Una funzione di sensitività delle soluzioni, risultato dell'ottimizzazione, è stata introdotta con lo scopo di valutare l'impatto dei parametri geometrici sulle prestazioni del motore. Alcuni risultati sperimentali, su un prototipo di motore a riluttanza, verranno presentati con lo scopo di validare la progettazione elettromagnetica fatta utilizzando algoritmi di ottimizzazione combinati a strumenti di analisi agli elementi finiti.

Nel **Capitolo 5** verrà trattata la progettazione e l'ottimizzazione di un motore per applicazioni ad alta velocità considerando più regioni di lavoro nelle quali un motore elettrico per trazione normalmente opera. Una procedura per la valutazione delle regioni di funzionamento del motore sarà considerata allo scopo. Infine, verranno presentati i risultati salienti ed i vantaggi che tale metodologia comporta sulla determinazione del motore richiesto.

Ulteriori analisi su diversi motori normalmente utilizzati in applicazioni per trazione

verranno presentate nel **Capitolo 6**. In particolare, lo studio sui motori SynRel, PMASynRel ed SPM, che sono stati messi a confronto, evidenzierà quali sono le differenze in termini di prestazioni elettromeccanica ed efficienza.

Il **Capitolo 7**, ultimo di questa prima parte, metterà in evidenza quali sono i vantaggi nell'utilizzo dei motori SynRel e PMASynRel per applicazioni elettrodomestiche, in particolare lavatrici. Lo scopo principale di questo capitolo, è quello di investigare la validità di questo tipo di macchine come possibili sostitute dei motori che attualmente vengono al momento commercialmente utilizzati.

La **Parte II** è principalmente dedicata alla definizione di un modello analitico per il motore a riluttanza con la sfida di predire accuratamente il campo di induzione al traferro del motore considerando l'effetto della geometria delle barriere di flusso rotoriche. Questa parte si suddivide in due capitoli (**Capitoli 8 e 9**).

Il **Capitolo 8** riassume le ipotesi alla base del modello analitico, mostra la formulazione per il calcolo delle forze elettromotrici statoriche attraverso delle funzioni descrittive dell'avvolgimento. Segue la descrizione del circuito equivalente derivante dalla rete di riluttanze rappresentativa per un motore sincrono a riluttanza con una e due barriere di flusso per polo. Infine, il calcolo dei parametri del modello analitico, l'andamento dell'induzione al traferro ed il confronto tra tali risultati e quelli determinati dal modello analitico verranno presentati.

Nel **Capitolo 9** verranno investigate tipologie di motori sincroni a riluttanza con configurazioni di avvolgimento multiterna. L'interesse per questo tipo di soluzioni nasce dalle richieste di tolleranza ai guasti ed affidabilità oggi richiesta per molte applicazioni nel campo degli azionamenti per trazione veicolare. Dall'estensione del **Capitolo 8**, verrà introdotta una procedura analitica per modellare e simulare macchine sincrone a riluttanza con avvolgimenti di statore multiterna attraverso un circuito equivalente magnetico. Il risultato saliente di questo studio sarà la determinazione del campo di induzione al traferro che può essere determinato per qualsiasi punto di lavoro.

Nella **Parte III**, saranno presentati i risultati sperimentali sui prototipi di motori sincroni a riluttanza ed a riluttanza assistita, che sono stati presentati nel **Capitolo 7**, alla fine di validare la metodologia di progetto utilizzata.

Preface

The interest on rotating electrical machines adopting permanent magnets (PMs) has increased during the past few decades, representing now a fashionable design option in a number of fields as industrial processing, transportation, actuators, household appliances and power plants.

The issues related to an increasing electrical energy demand and consumption, have generated a tendency to research electrical drives with high efficiency, pushing electrical machines technology to further improvements. The introduction of permanent magnets based on rare earth, experienced since the 1960's, gave a great input in the development of innovative machine topologies. On the other hand, the increase and the instability of rare earth PMs price, especially between 2010 and 2013, have directed the research of rare earth free alternatives, or machines using a smaller amount of PMs.

Actually, the current trend in the industrial and academic research focused on developing high performance electric motors and generators, among different electrical machines, highlights the Synchronous Reluctance (SynRel) and the Permanent Magnet Synchronous Reluctance (PMASynRel) motors as best candidates to satisfy the future energy and efficiency requirements.

This thesis is comprehensively dedicated to theoretical and experimental analysis and design of the Synchronous Reluctance (SynRel) and the Permanent Magnet Assisted Synchronous Reluctance (PMASynRel) machines. In particular, it will be focused on electrical machines which power ratings are ranging from fraction of Watts to some hundred kWatts, for vehicular traction and house-hold appliances.

SynRel and PMASynRel motors exhibit many technical advantages, like simple and robust structure, high torque density, high efficiency, small space required for PMs, high degrees of freedom in the design, high operating speed range, high overload capability, low back EMF (null in case of SynRel motors), leading to a safe behavior in case of inverter failure. Furthermore, thanks to the appropriate vector control algorithm, the performance in terms of efficiency and torque become highly competitive.

The subject matter covered in the thesis is organized into three Parts, each including a certain number of chapters. **Part I** includes seven chapters summarizing the research activities carried out during the Ph.D. period. The first six chapters are dedicated

to electrical machines for vehicular traction, while chapter 7 investigate on motors for house-hold appliances.

Chapter 1 is mainly introductory and meant to provide the basics information to understand which are the pros and cons and the features of the machines under study.

Chapter 2 summarize the design criteria and the electrical requirements of ferrite PMASynRel machine for traction application. The electromechanical performance have been evaluated and compared, in terms of torque and power. A brief description of the electric supply system in order to accurately and efficiently manage the motor for achieving the requested performance is presented.

Chapter 3 highlights the influence and benefits of using ferrite magnets on the machine performance, emphasizing the importance of a careful evaluation of the magnet volume in order to increase the performance while reducing the used quantity.

Chapter 4 is devoted to the sensitivity analysis of the machine performance in terms of torque ripple with respect to the geometrical design. An optimization algorithm has been performed in order to investigate and determine a rotor geometry which maximize the torque and reduces the torque ripple. The impact of the geometrical parameters is taken into account and the sensitivity of the optimal solution to the geometry variation is pointed out. This chapter highlights the difficulty to get a robust geometry as far as the torque ripple reduction is concerned. Finally, a few experimental results on a Synchronous Reluctance motor prototype will be presented, compared with Finite Element Analysis simulations for validation.

Chapter 5 deals with the design and optimization of a high speed PMASynRel motor considering the driving cycles of an electric vehicle. A procedure is employed to evaluate the most effective design area, which has to be considered for the global optimization. Both results and advantages of the adopted methodology are highlighted.

Further analysis on traction machines are going to be presented in **Chapter 6**. A comparison between ferrite and sintered NdFeB PMASynRel, SynRel and a Surface mounted PM (SPM) machines performance is deeply investigated.

Chapter 7, the last of this first part, will highlight the advantages in using SynRel and PMASynRel motors for house-hold appliances. The main purpose of this chapter is to discuss the features of these motors as a valid substitute to commercial motors actually used for washing machines application.

Part II is dedicated to the analytical modeling of SynRel machines with the challenge of predicting accurately the air-gap field of the machine taking into account the effect of the rotor flux barriers. This Part is divided into two chapters.

Chapter 8 explains the hypothesis on which the analytical model is based, the calculation of stator Magneto Motive Force through winding function and describes the reluctance network equivalent circuit for a SynRel motor with one and two flux barriers per pole. The computation of the parameters of the model, the air-gap flux density and finally some comparison with Finite Element Analysis are presented.

In **Chapter 9** SynRel motors with split-phase stator winding sets supplied by multiple inverters have been investigated as an increasingly attractive solution for fault-

tolerant, rugged, magnet-free vehicle traction drives. As an extension to the previous chapter, an analytical procedure to model and simulate a SynRel motor, with a split-phase stator winding, through a magnetic equivalent circuit (MEC) technique, has been introduced. As an output, the air-gap flux density of the SynRel motor can be computed at any operating point.

Part III, finally, presents some experimental measurements carried out for two prototypes of SynRel and PMASynRel machines, with the purpose of comparing the results achieved in the motor optimization presented in **Chapter 7**.

Publications and Scientific Contributions

1. A. Tassarolo, F. Luise, P. Raffin, M. Degano, "Traditional Hydropower Plant Revamping based on a Variable-Speed Surface Permanent-Magnet High-Torque-Density Generator", *International Conference on Clean Electrical Power*, ICCEP 2011, 14–16 June 2011 Torremolinos Spain, pp. 350–356.
2. M. Degano, M. Mezzarobba, A. Tassarolo, "Analytical Calculation of Air-Gap Armature Reaction Field Including Slotting Effects in Fractional-Slot Concentrated-Coil SPM Multiphase Machines", *III International Conference on Power Engineering, Energy and Electrical Drives*, IEEE POWERENG 2011, 11–13 May 2011 Torremolinos, Spain, pp. 1–6.
3. L. Branz, M. Degano, M. De Martin, A. Tassarolo, "On the Use of Dimensioning Equations for Surface Permanent Magnet Machines", *International Symposium on Power Electronics, Electrical Drive, Automation and Motion*, IEEE SPEEDAM 2012, 20–22 June 2012 Sorrento, Italy, pp. 522–526.
4. A. Tassarolo, F. Luise, P. Raffin, M. Degano, "A Simple Approach to Air-Gap Armature Reaction Field Computation in Fractional-Slot SPM Multiphase Machines", *Journal of Energy and Power Engineering*, vol 6, n. 9 Sept. 2012, pp. 1472–1479.
5. E. Carraro, M. Degano, N. Bianchi, "Permanent Magnet Volume Minimization in Permanent Magnet Assisted Synchronous Reluctance motors", *International Conference and Exhibition on Ecological Vehicles and Renewable Energies*, EVER 2013, 27–30 March 2013 Montecarlo, Monaco, pp. 1–4.
6. E. Carraro, M. Degano, M. Mattia, N. Bianchi, "Formula SAE Competition: Electrical motor design", *IEEE International Electric Machines and Drives Conference*, IEMDC 2013, 12–15 May 2013 Chicago, IL, USA, pp. 1142–1148.
7. M. Degano, N. Bianchi, E. Fornasiero, "Sensitivity Analysis of Torque Ripple Reduction of Synchronous Reluctance and Interior PM Motors", *Energy Conversion Congress and Exposition*, IEEE ECCE 2013, 15–19 Sept. 2013, pp. 1842–1849.
8. M. Degano, E. Carraro, N. Bianchi, "Robust optimization of a traction PMASR motor according to given driving cycles", *International Conference on Electrical Machines*, ICEM 2014, 2–5 Sept. 2014, pp. 270–276.
9. A. Tassarolo, M. Degano, N. Bianchi, "On The Analytical Estimation of The Air-gap Field in Synchronous Reluctance Machine", *International Conference on Electrical Machines*, ICEM 2014, 2–5 Sept. 2014, pp. 239–244
10. M. Degano, N. Bianchi, E. Fornasiero, "Sensitivity Analysis of Torque Ripple Reduction of Synchronous Reluctance and Interior PM Motors", *IEEE Transactions on Industry Applications*, vol. *PP*, no. 99, pp. 1–10.

11. A. Tessarolo, C. Bruzzese, M. Degano and L. Branz, "Analytical Modeling of Split-Phase Synchronous Reluctance Machines", *Annual Conference of the IEEE Industrial Electronic Society*, IECON 2014, 29–1 Oct./Nov. 2014, Dallas (TX), USA
12. E. Carraro, M. Degano, M. Morandin, N. Bianchi, "PM Synchronous Machine Comparison for Light Electric Vehicles", *IEEE International Electric Vehicle Conference*, IEVC 2014, 17–19 Dec. 2014, Florence, Italy

Part I

**Design and Optimization
Techniques
for PMASynRel motors**

Chapter 1

Synchronous Reluctance and Permanent Magnet Assisted Reluctance Machine

1.1 Background

Since they were first proposed, in the early 1920s [1], Synchronous Reluctance (SynRel) motors have found little applications for many years due to their poor efficiency and power factor when supplied from the grid. During the 1990s, with the advent of modern variable-frequency converters and digital control systems, these motors disclosed their potentialities as possible competitive alternatives to traditional induction motor drives [2], [3].

Furthermore, optimized rotor designs were proposed to achieve better power factor values [4]. In recent years, a large amount of work has been carried out to optimize SynRel motor performance in terms of torque pulsations [5]-[6], copper losses [7], core losses [8]-[9] and overall efficiency [10]. Presently, SynRel motors appear strongly attractive in many fields, like vehicle traction [11]-[12] and household appliances [13]-[14], due to the widely-recognized benefits they bring in terms of [15]: rugged construction, high-speed capabilities, absence of excitation winding, removed or strongly reduced need for permanent magnets. Improvements in the machine torque density can be, in fact, obtained with limited use of rare-earth permanent magnets or low-cost ferrite ones, in the so-called permanent-magnet-assisted SynRel configurations [16]-[17].

Due to the exponential price increase of rare earth, interest is rising around synchronous reluctance (SynRel) machines and permanent magnet assisted reluctance SynRel (PMASynRel) motors. Compared to IPM motors, PMASynRel machines seem to be promising alternatives, because they combines the advantages of the pure reluctance geometry with IPM motors, leading to high saliency machines with a minimum PM volume. This last feature is very desirable in a view of reducing the machine cost. Between the magnets topology, ferrite seems an interesting candidate with their low cost and quite interesting performances [18]. In the following sections a brief explanation of these motors features is going to be presented.

1.2 Synchronous Reluctance Machine

SynRel motor principle of operation lies on the different reluctance (magnetic anisotropy) that the rotor exhibits along orthogonal d and q axes [1], [3]. Such anisotropy can be obtained in different ways, such as by suitably shaping rotor outer profile [1], [4]; however, the most widespread SynRel design includes a round rotor with uniform mechanical air gap and appropriately designed flux barriers [19]-[20]. Rotor flux barriers can be shaped according to different possible geometries [19]. The most typical ones, shown in Fig. 1.1, are the so-called C-shape (Fig. 1.1 a) and the circular (or round) shape (Fig. 1.1 b).

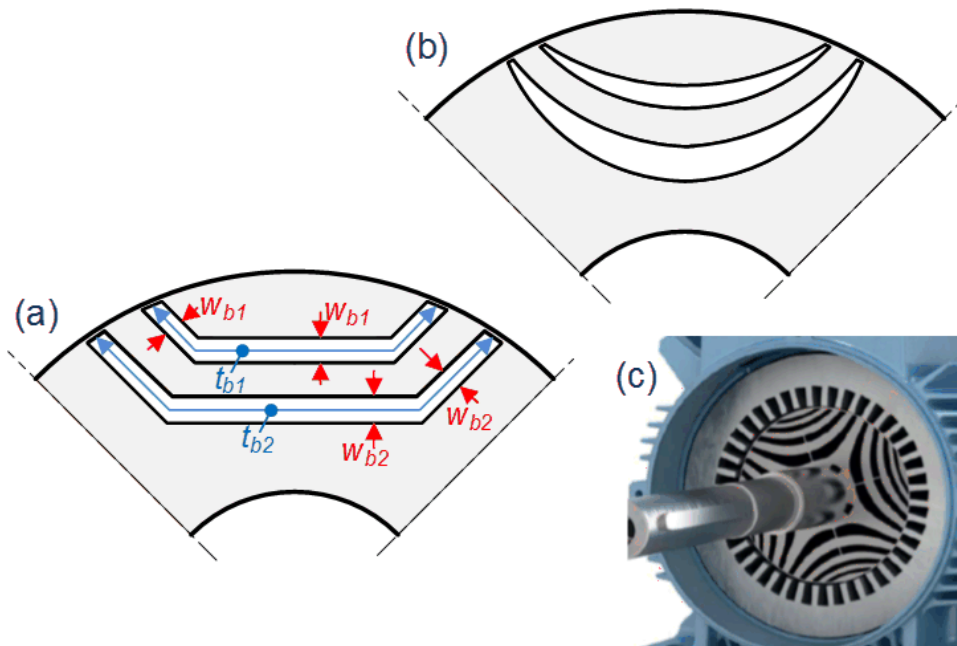


Figure 1.1: (a) SynRel rotor with C-shaped barriers; (b) SynRel rotor with circular barriers; (c) example of SynRel motor with circular barriers.

The former case, wherein the barrier is composed of one or more straight segments, is particularly suitable for Permanent-Magnet Assisted SynRel (PMASynRel) motors as it allows for simple accommodation of parallelepiped-shaped permanent magnets inside the barrier [7], [8], [15]-[17], [21]; round barriers, instead, are preferably employed in permanent-magnet-free SynRel machines [4], [10], [11], [14], [19].

In order to exhibit a proper torque, the SynREL machine is characterized by a small air gap and a high anisotropic rotor. Several rotor flux barriers force the flux lines to flow through given iron paths.

In Table 1.1 the main advantages and disadvantages for the SynRel motors are summarized.

Table 1.1: SynRel Motor Main Features

<i>Advantages</i>	<i>Disadvantages</i>
Well suited for overload (robust configuration)	Limited power factor
Good flux weakening capability	High torque ripple
Widely suited for zero and low speed sensorless control	Higher volume with respect to PM machines
Quite suited for high speed sensorless control sensorless control	Noise and Vibration (if torque ripple is not minimized)
Low maintenance	Poorly suited for energy recovering
High operating speed range	-
Null/Low Bemf	-
Cost effective (no PMs)	-

1.3 Permanent Magnet Assisted Synchronous Reluctance Machine

For the purpose to saturate the iron bridges (both inner and outer) and to increase the power factor, permanent magnets (PMs) are sometimes inset within the flux barriers. In this case, the machine is referred to as PM assisted synchronous reluctance machine (PMASynRel), or interior permanent magnet (IPM) machine [22, 23].

They exhibit comparable performance to surface mounted PM machines (SPM) needing a limited amount of high cost rare earth magnets, such as NdFeB or SmCo, otherwise requiring filling the flux barrier with ferrite, so making possible the development of a low cost solution [18, 24].

It is well known that the use of PMs can increase the efficiency and power density of electric motors. However, there are several issues associated with high-performance rare-earth PMs, particularly if the price increase of the neodymium and restrictions on market supply in the last decade have to be taken into account (see Fig. 1.2).

Therefore, ferrite PMs used in industrial electric motors may be a low-cost alternative. The main drawback of the latter is the much lower energy density (up to ten times lower). Therefore, motors integrating ferrite PMs have to be optimized in order to achieve the same performance of conventional PMSMs.

PMASynRel motors exhibit many technical advantages, like simple and robust structure, high operating speed range, high overload capability, low back Electro Motive Force (EMF), leading to a safe behaviour in case of inverter failure.

On the contrary, the most important drawback of reluctance machines is the higher torque ripple [25]. A reduction of the torque ripple can be achieved by means of suitable choice of the number of the flux barriers with respect to the number of slots or an appropriate design of the flux barrier geometry, in addition to the step skewing [26, 27].

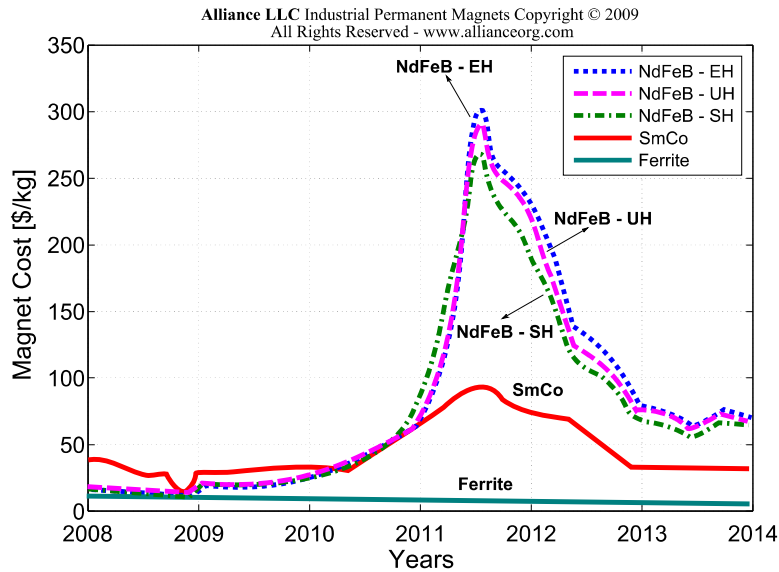


Figure 1.2: Permanent Magnets price trend during the past decade.

1.4 Application fields

The advantages highlighted are becoming crucial for those non-industrial application, as the electric vehicles and household appliances. High performance and compactness are often the winning characteristics of such machines as respect to the induction machines.

Referring to the automotive field, variable speed drives as PM synchronous machine are adopted to improve the overall performance of the vehicles. With respect to traditional IMs, SynRel motors are showing a higher torque density (approximately 15-20%) and an increased average efficiency (5-10%).

Table 1.2: SynRel Motor Main Features

<i>Advantages</i>	<i>Disadvantages</i>
Limited use of PMs.	High torque ripple
Cost-effective with ferrite PMs.	rotor design is crucial
Excellent flux weakening performance	High torque ripple
Well suited for full speed sensorless control	Higher volume with respect to PM machines
Good power factor	Noise and Vibration (if torque ripple is not minimized)
Low maintenance	Poorly suited for energy recovering
High efficiency	-
High Torque Density	-

Adopting SynRel technology, as illustrated in Fig. 1.3, it is possible to design the motor for:

- the same frame size and better efficiency;
- smaller frame size and equal efficiency;
- an in-between solution with slightly higher efficiency and slightly smaller frame size.

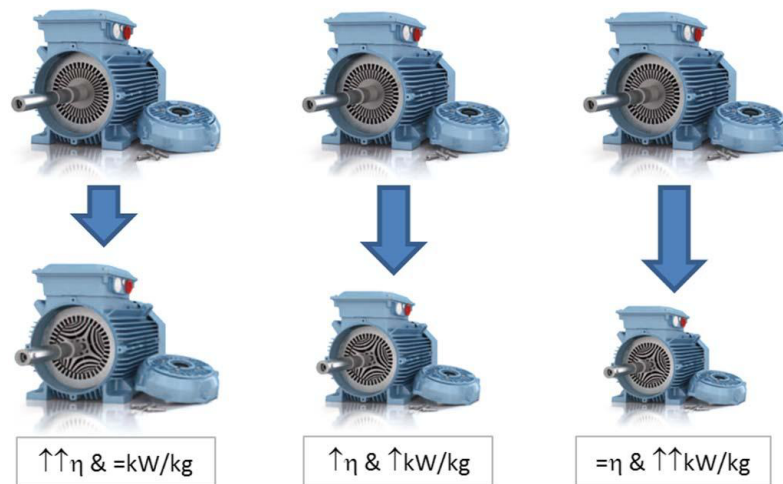


Figure 1.3: Frame size versus efficiency and power density in SynRel motors.

In Fig. 1.4, the expected loss reduction when considering the same and smaller and reduced frame sizes, in relation to a reference Squirrel Cage Induction Motor (SCIM) frame size, is shown. The new rotor has neither magnets nor windings and, thus, suffers virtually no power losses-which makes it uniquely cool. In general, for the same frame size, a 25% reduction in the overall losses with respect to IE3-class SCIMs can be assumed¹. Therefore, there is the possibility of a significant efficiency gain if the standard frame size is used.

The design flexibility due to the absence of rotor winding excitation and the variety of PM sizes and characteristics allow to achieve several features, e.g. fault-tolerance and flux-weakening capability. However the recent trend is to select those configurations that allow to minimize the PM utilization. It is also due to the issues related to PM temperature de-rating, mechanical stress, and PM reliability. The PM synchronous reluctance machine or interior PM machine is, among the others, a promising candidate to satisfy the traction requirements. Thanks to its anisotropy rotor structure is able to provide torque not only due to the PM flux.

¹ABB Review, Corporate J., pp. 1-80, Jan. 11, 2012.

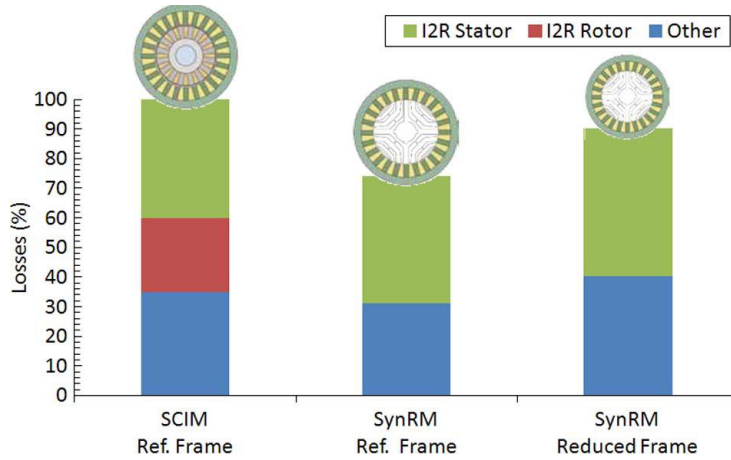


Figure 1.4: Same stator size, different rotor type: loss reduction (note: stator copper losses slightly increase, and rotor losses are reduced to zero).

1.5 Basic principles

The reluctance machine is characterized by the absence of PMs; however the air barriers create a different magnetic behaviour along the two rotating axes. As an example Fig. 1.5 shows a 4 poles and 24 slots SynRel machine, whose rotor is characterized by three flux-barriers per pole. Fig. 1.5 highlights the different magnetic flux paths of the two flux components, in particular it can be noted that the magnetic circuit in q-axis component λ_q does not include the air barriers. Generally a higher number of flux-barriers per pole increases the rotor anisotropy.

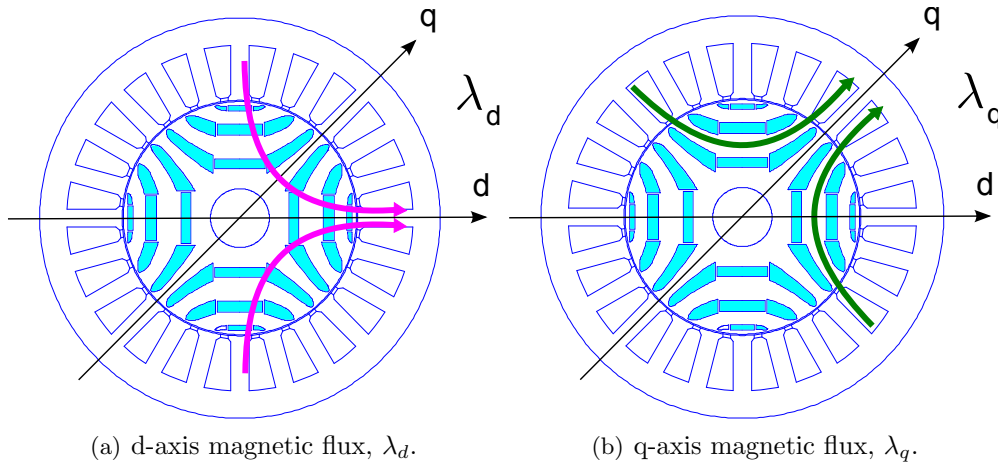


Figure 1.5: Magnetic flux trajectory according to the direct and quadrature axes in a 4 poles SynRel rotor configuration.

The synchronous anisotropic machines are characterized by a rotor structure that yields a magnetic anisotropy, or rather a different magnetic behaviour along the polar and inter-polar axes.

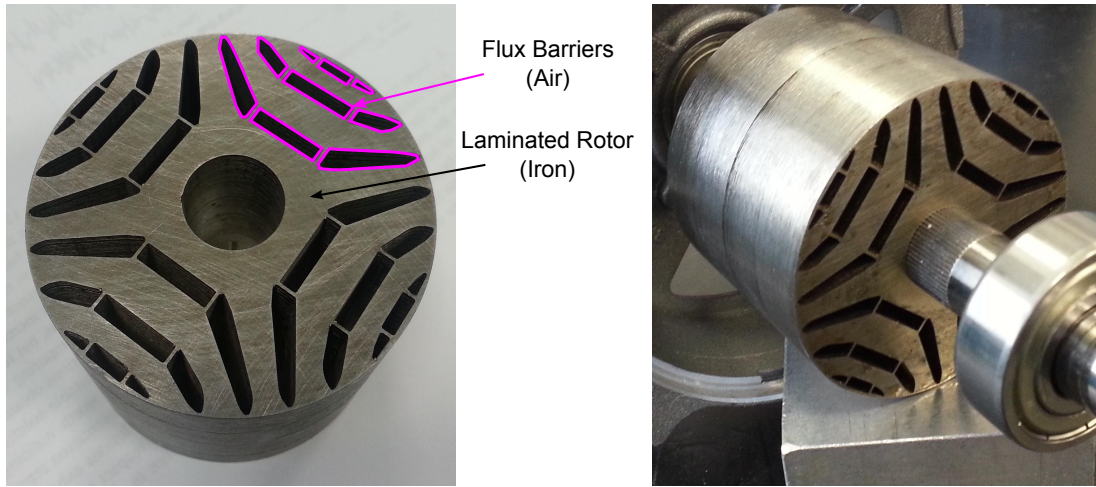


Figure 1.6: 4 poles SynRel rotor prototype photos.

Fig. 1.6 shows a SynRel machine prototype: it highlights the air barriers structure, the iron ribs, and rotor iron laminations.

First of all it is not possible to characterize the machine with only one value of self-inductance and mutual-inductance because their values varies as a function of the rotor position. Furthermore, it is necessary to take into account the effects due to the iron magnetic saturations in order to thoroughly study the performance of the electric motor.

1.5.1 Iron saturation effect

Considering the iron saturation, the magnetic characteristics (i.e. the flux linkage as function of the current) can not be expressed through linear equations and constant values of inductances [28]. In fact the cross saturation effects of the d-axis current axis and the q-axis flux and vice versa introduces more complex relations. At first the cross saturation effect can be neglected so assuming that PM flux linkage is only in d-axis and $\Lambda_{mg} = \lambda_d(0)$ (zero in case of SynRel machine). The magnetic characteristics have to be described by the following equations:

$$\lambda_d(t) = \Lambda_{mg} + \lambda_{d,i}(i_d(t)) \quad (1.1)$$

$$\lambda_q(t) = \lambda_{q,i}(i_q(t)) \quad (1.2)$$

In Fig. 1.7 an example of ideal and real magnetic characteristics of both axes are reported. In particular it is highlighted the non linear effect due to high currents in the flux linkage.

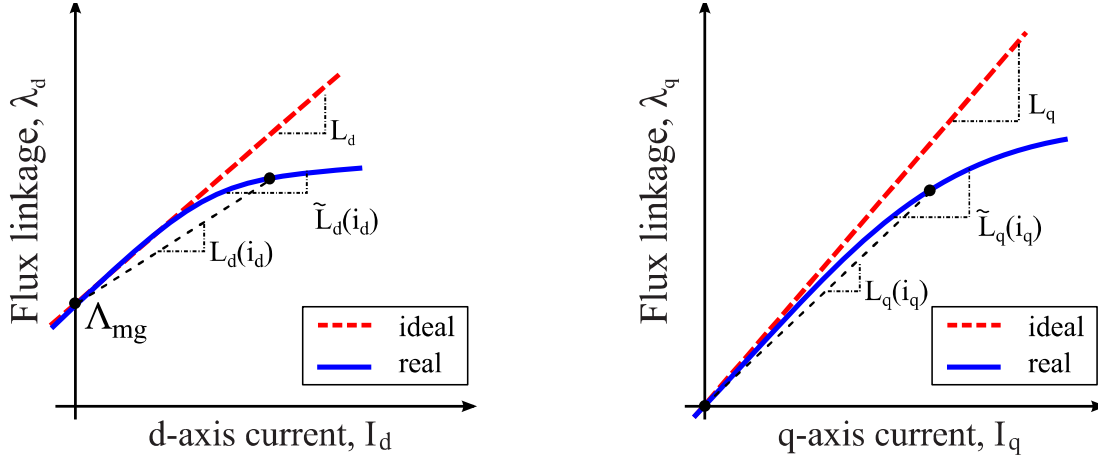


Figure 1.7: Magnetic d- and q-axes flux linkages as functions of I_d and I_q current respectively, in ideal and real cases.

With iron saturation differential inductances are defined as the slope of the magnetic characteristic at a particular current:

$$\tilde{L}_d(i_d(t)) = \frac{d\lambda_d(i_d(t))}{di_d(t)} \quad (1.3)$$

$$\tilde{L}_q(i_q(t)) = \frac{d\lambda_q(i_q(t))}{di_q(t)} \quad (1.4)$$

Instead, the apparent inductances are defined as the slope of the straight line which connects one point of the magnetic characteristic with the point $(0, \lambda_{mg})$, in d-axis case, or point $(0, 0)$ in q-axis case:

$$L_d(i_d(t)) = \frac{\lambda_d(i_d(t)) - \lambda_{mg}}{i_d(t)} \quad (1.5)$$

$$L_q(i_q(t)) = \frac{\lambda_q(i_q(t))}{i_q(t)} \quad (1.6)$$

With this considerations the torque equation can be write as:

$$m(i_d(t), i_q(t)) = \frac{3}{2}p \left[\lambda_d(i_d(t))i_q(t) - \lambda_q(i_q(t))i_d(t) \right] \quad (1.7)$$

by using the equations 1.5 and 1.6 it becomes:

$$m(i_d(t), i_q(t)) = \frac{3}{2}p \left[\Lambda_{mg}i_q(t) + [L_d(i_d(t)) - L_q(i_q(t))]i_d(t)i_q(t) \right] \quad (1.8)$$

In Chapter ?? the effect of the non linearities and the cross saturation on the motor parameters will be deeply investigated through FE analysis and measurements on a SynRel prototype.

Chapter 2

Electric Motor Requirements and Design for Traction Application

In this chapter, a preliminary analysis has been carried out in order to define the motor electrical requirements. The analysis is based upon the performance required by the various dynamic events that a Formula SAE car has to satisfy. Two different stator geometries, with the same number of slots and different outer diameter, have been considered as further constraints. For each stator laminations and a given gear ratio, two IPM motors has been developed and optimized with the objective to minimize the torque ripple. The best candidate, in terms of final mass and performance, has been scaled for a double gear ratio and finally compared with two equivalent outer diameter and stack length surface mounted permanent magnet (SPM) motors. One is characterized by the same lamination steel, while the second is equipped with a fractional slot concentrated winding (FSCW). Finally, some considerations on the power supply inverters has been presented. Several parts of this project have been presented by the author in international conferences. In particular, in this Chapter, the work presented in [29] is widely described.

2.1 Preliminary analysis and design considerations

The 2013 Formula SAE edition introduces important electrical constraints and specifications in the design of a traction system for an Electric Vehicle (EV). The electrical constraints that limit the degrees of freedom in the design of electric motors for traction are: (i) the maximum power that can be developed by the battery pack, equal to 85 kW and (ii) the maximum DC voltage, lower of 300 V or 600 V depending on the competition. Considering the previous constraints, the requested torque vs. speed is evaluated in order to achieve excellent performance during the "Acceleration" event as well as the maximum speed. Assuming an uniformly accelerated motion during the $s = 75$ m-track of the "Acceleration" competition in a top time of $t = 4$ s, the predicted acceleration is equal to

$$a = \frac{2 \cdot s}{t^2} \cong 10 \text{ m/s}^2 \quad (2.1)$$



Figure 2.1: MG0712, formula SAE car, year 2012, Race UP team, University of Padova, Italy. Courtesy of Prof. Giovanni Meneghetti.

The total mass of the vehicle inclusive of the 80 *kg*-pilot is assumed, prudentially, in the order of 400 *kg*. Consequently, the total traction force is

$$F_n = m \cdot a \cong 4000 \text{ N} \quad (2.2)$$

The consequent evaluation of the maximum frictional force tire-road, assuming a frictional coefficient $\mu_f = 2$ and two driven rear-wheels, must ensure the capacity to transfer the traction force without wheel slip. It results

$$F_{MAX} = \frac{1}{2} \cdot m \cdot g \cdot \mu_f \cong 4000 \text{ N} \quad (2.3)$$

Considering a wheel diameter $D_w = 500 \text{ mm}$, the rated torque per each wheel is finally

$$T_{wn} = \frac{1}{2} \cdot F_n \cdot \frac{D_{wn}}{2} \cong 500 \text{ Nm} \quad (2.4)$$

The requested maximum speed is $v_{MAX} \cong 140 \text{ km/h}$, equivalent to a rotation wheel speed $n_w \cong 1480 \text{ rpm}$. Two different gear ratios, 1 : 4 and 1 : 8, have been selected. The rated torque T_n and maximum speed n_{MAX} have been evaluated consequently. According to the 85 *kW* power limitation, two traction motors have been analysed. The predicted base speed n_B has been evaluated in order to achieve a rated power of $P_n = 40 \text{ kW}$ for each unit. Finally, the DC bus rated voltage V_{DCn} has been fixed to the lowest value established by SAE rules, 300 *V*. Although a lower voltage, for e.g. 48 *V*, allows automotive class components to be employed [30, 31], high voltage yields a reduction of the size of the power supply system and line connections.

The resultant motor specifications are reported in Table 2.1.

2.2 IPM motors: design and analysis

Two existing $Q = 36$ slot stator laminations, one with an outer diameter $D_e = 337 \text{ mm}$ (A) and the second $D_e = 276 \text{ mm}$ (B), has been considered in the design of the electric

Table 2.1: Motor specifications.

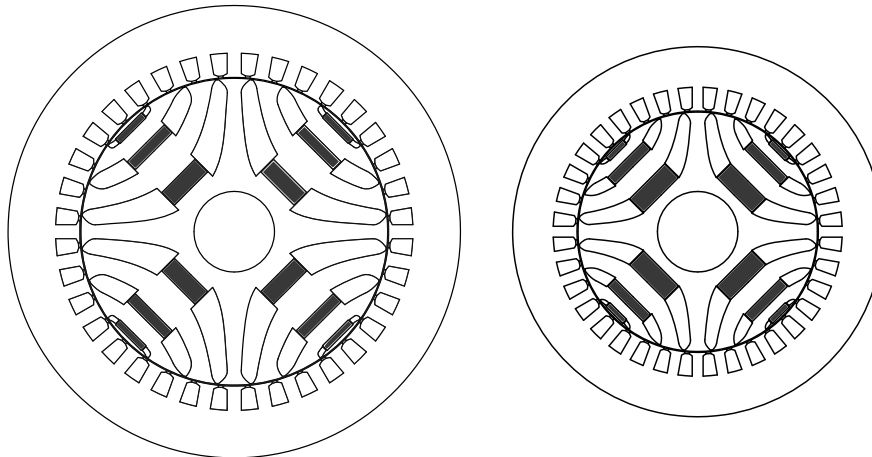
Gear ratio	1 : 4	1 : 8	Unit
n_{MAX}	6000	12000	<i>rpm</i>
n_B	~ 3000	~ 6000	<i>rpm</i>
T_n	125	63	<i>Nm</i>
P_n	~ 40	~ 40	<i>kW</i>
V_{DCn}	300		<i>V</i>

Table 2.2: Motor specifications.

Lamination type	A	B	Unit
Q	36	36	–
D_e	337	276	<i>mm</i>
D	230	180	<i>mm</i>
S_{slot}	183.2	148.0	<i>mm</i> ²

motors. The corresponding air gap diameter D and slot area S_{slot} are reported in Table 2.2.

These lamination geometries are in accord to the overall dimensions of a 600 cm^3 4-cylinder ICE that equips an existing Formula SAE conventional race car and that will be replaced by electric motors. In order to reduce the maximum supply frequency, the number of poles has been selected to $2 \cdot p = 4$. As a consequence, an Integral Slot Distributed Winding (ISDW) has been designed. This winding arrangement proves to be the most effective solution when an high anisotropic rotor is adopted, because, comparing to Fractional Slot Concentrated (FSCW), it drastically increases the saliency ratio [32, 33]. On the basis on the geometry constraints and a gear ratio 1 : 4, two motors,

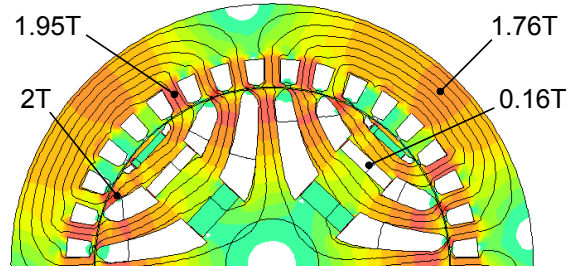


(a) IPM-A: 36-slot 4-pole, outer diameter 337 mm. (b) IPM-B: 36-slot 4-pole, outer diameter 276 mm .

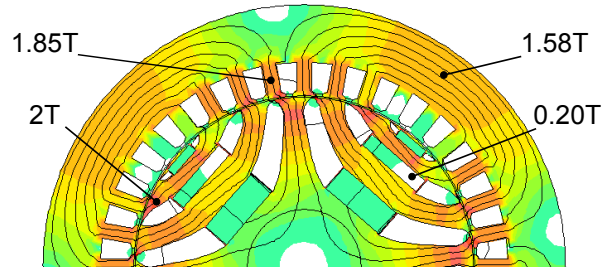
Figure 2.2: IPM designs.

IPM-A ($D_e = 337 \text{ mm}$) and IPM-B ($D_e = 276 \text{ mm}$), have been designed, as reported

in Fig. 2.2. The rotor structure is characterized by three symmetrical flux barriers per pole, filled by ferrite (remanence flux density $0.4 T$ @ $20^{\circ}C$, knee flux density $0.1 T$ @ $20^{\circ}C$, recoil permeability 1.05 , density $4800 kg/m^3$).



(a) IPM-A: 36-slot 4-pole, $D_e = 337 mm$.



(b) IPM-B: 36-slot 4-pole, $D_e = 276 mm$.

Figure 2.3: IPM machines: flux density map at rated load.

The geometry has been tuned and analysed by means of 2D FEA. The stack length L_{stk} has been scaled in order to achieve the rated torque T_n , taking full advantage of the iron, working up to the knee of the iron $B - H$ characteristics, as reported in Fig. 2.3. However, the flux density maps show some critical areas for the demagnetization in the PMs, although their values are higher than the knee value of $0.1 T$ at $20^\circ C$.

In the same loading condition, a Non-dominated Sorted Genetic Algorithm (NSGA) has been performed in order to minimize the torque ripple. Since the stator geometries are fixed, only the rotor structure has been optimized for both designs. The optimization variables considered are the flux barrier angles and the ratio between air and iron path along the q -axis. At the end of the automatic procedure, the minimum torque ripple is 12%, achieved in IPM-B, while IPM-A exhibit an higher value, around 18%.

The number n_{cs} has been changed in order to set the base speed close to the requested $3000 rpm$, ensuring the feasibility of double layer winding. The rated current I_n , rated current density J_n (assuming a fill factor of 0.4), PM flux linkage Λ_{PM} and the characteristic current I_{ch} have been computed as well as the machine masses (copper G_{Cu} , PMs G_{PM} , stator iron G_{Fes} , rotor iron G_{Fer} , total iron G_{Fe} , total G).

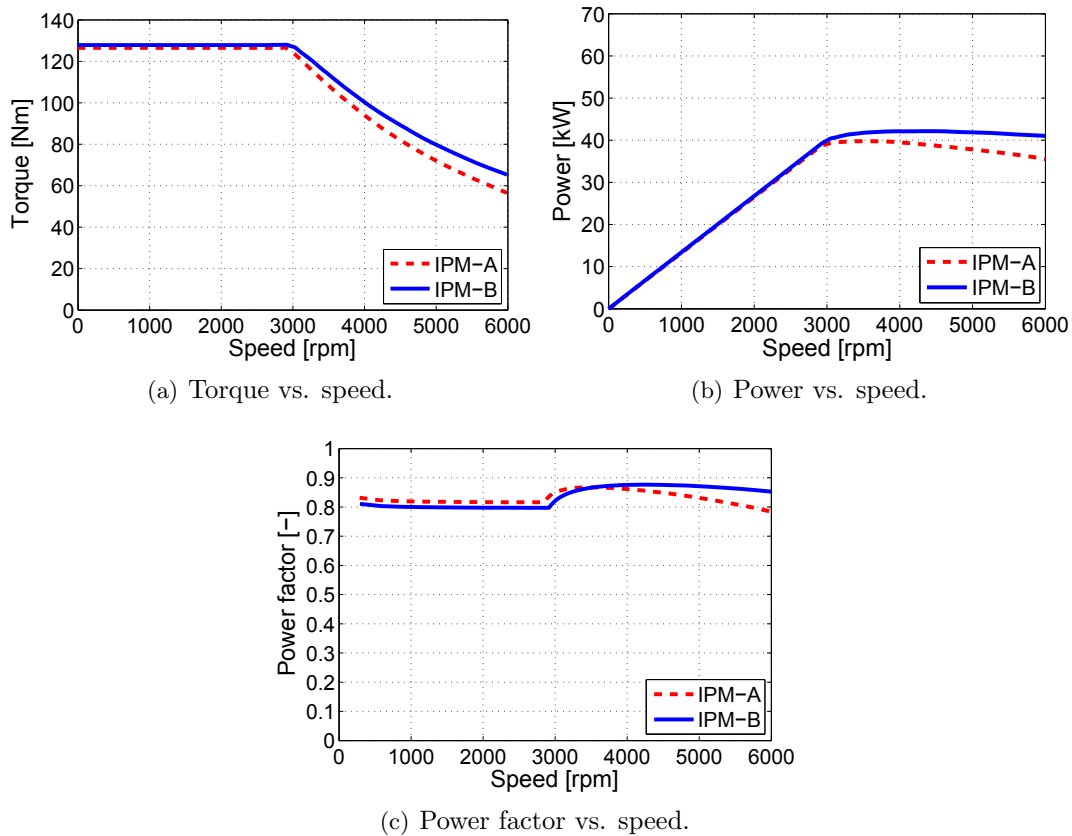


Figure 2.4: Performance comparison.

Both machines exhibit similar torque, power and power factor (PF) characteristics, as reported in Fig. 2.4. Table 2.3 summarizes the main electromechanical results. IPM-

A presents an overload current density of about 12% higher than that in IPM-B, while the current is slightly higher. However, due to the selected number of series conductors per each slot n_{cs} , the rated current densities values implies an adequate cooling system. If this increases the complexity of the systems, on the other hand it yields to reduce the machine mass, improving the car dynamic performance. Conversely to NdFeB, the ferrite PM has got a positive reversible temperature coefficient of coercivity. This yields to increase the demagnetization strength as the temperature increases, leading to better car dynamic performance.

Analysis proves that a characteristic current (given by the ratio between PM flux linkage and q -axis inductance) closes to the rated current, yields the machine to show an excellent Constant Power Speed Range (CPSR) [34]. Although this condition is not verified by the considered motors, due to the limited requested FW ratio (2 : 1), the performance over the base speed is well suited. As shown in Figs. 4b, 4c, the higher value of the characteristic current of IPM-B produces a slightly better CPSR and power factor than those of IPM-A.

Finally, the mass of both machines is equal, emphasizing that there are not substantially advantages selecting higher stator diameters. However, due to the higher air gap diameter, the impact of the end winding on the copper mass in IPM-A is two times higher than that in IPM-B.

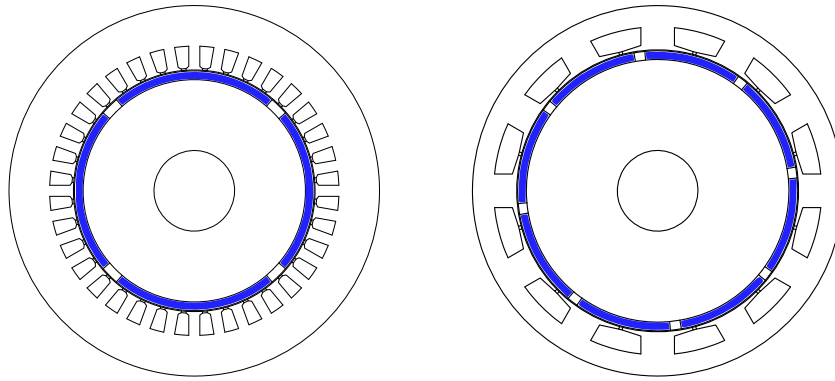
Table 2.3: Key machine parameters summary, gear 1 : 4.

Design	IPM-A	IPM-B	Unit
D_e	337	276	<i>mm</i>
D	230	180	<i>mm</i>
L_{stk}	50	80	<i>mm</i>
n_{MAX}	6000	6000	<i>rpm</i>
n_B	2857	2915	<i>rpm</i>
T_n	125	125	<i>Nm</i>
I_n	133	127	<i>A_{RMS}</i>
J_n	14.5	12.9	<i>A_{RMS}/mm²</i>
Λ_{PM}	29.2	32.5	<i>mVs</i>
I_{ch}	30	48	<i>A_{RMS}</i>
n_{cs}	8	6	—
G_{Cu}	7.9	5.8	<i>kg</i>
G_{PM}	0.9	1.4	<i>kg</i>
G_{Fes}	15.9	18.0	<i>kg</i>
G_{Fer}	8.9	8.4	<i>kg</i>
G_{Fe}	24.8	26.4	<i>kg</i>
G	33.6	33.6	<i>kg</i>

2.3 Comparison to SPM motors

In order to achieve a further reduction of the masses, a gear ratio 1 : 8 has been considered, leading to a scaling of the stack length of an half. As IPM-A become

practically not feasible in terms of 2D FEA analysis, due to the noticeable effects of the end winding, only the smaller stator, called IPM-B', has been evaluated. This design has been compared with two equivalent size SPM machines, as reported in Fig. 2.5. The first, SPM-B, equipped with the same 36-slot stator and 4-pole rotor, while the second, SPM-C, presents a 12-slot and 8-pole, addressing with a FSCW. The PM used in the machine is NdFeB (remanence flux density $1.1 T @ 20^{\circ}C$, knee flux density $0.1 T @ 20^{\circ}C$, recoil permeability 1.05, density $7500 kg/m^3$).



(a) SPM-B: 36-slot 4-pole, outer diameter 276 mm. (b) SPM-C: 12-slot 8-pole, outer diameter 276 mm.

Figure 2.5: SPM designs.

A load simulation has been performed in order to evaluate the flux density levels at rated load, as reported in Fig. 2.6. The number n_{cs} of SPM machines has been changed in order to include the requested torque vs. speed curve up to the maximum speed $12000 rpm$. As expected and reported in Fig. 6.3, it is exhibited by IPM-B'.

Regarding the electromechanical characteristics, SPM-B shows a wider FW range than SPM-C, about 60% higher. In order to meet the final torque in SPM-B and especially SPM-C, their base speeds has been increased highly, thus requiring an higher phase current. It is worth noticing that IPM-B' and SPM-B have approximately the same rated slot current. Both SPM machines shows characteristic current higher than the rated current, yielding to a torque vs. speed characteristic with a zero torque at the maximum speed. Regarding the PF trends, SPM machines ensure a better value than IPM machines, higher than 0.9 up to almost $12000 rpm$. On the other hand, it shows a great reduction trend when higher speeds are required.

The evaluation of the masses shows that the lowest values are achieved with IPM-B' and SPM-C. It is worth noticing that, contrarily to IPM machines, the rotor mass of SPM motors can be further reduced introducing flux barriers in proximity of the rotor shaft, without affecting the motor performance. This is especially true for the high pole number machine, SPM-C, for which a predicted reduction of about 30% is achievable.

The previous arguments emphasize as the most promising candidates the IPM-B' and SPM-C. The first machine exhibits the best torque and power vs. speed trends,

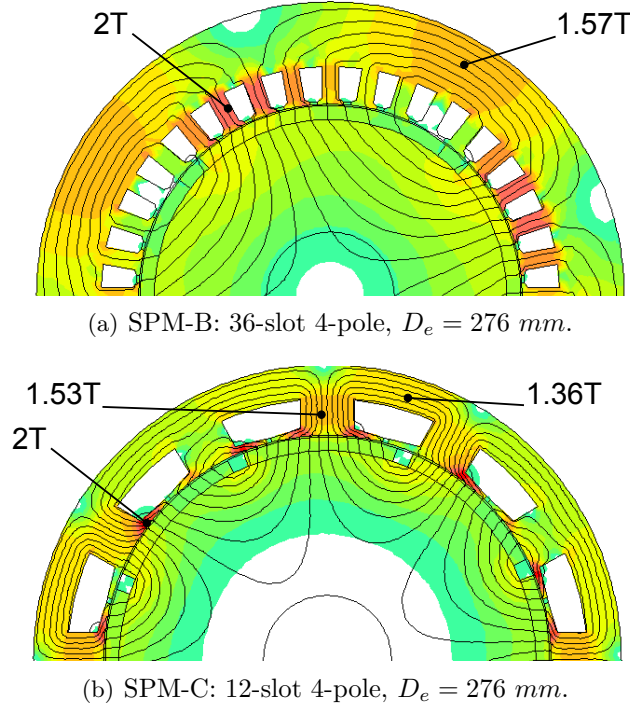


Figure 2.6: SPM machines: flux density map at rated load.

especially in FW operation. The SPM-C machine, although does not show a suitable traction characteristic, offer its own advantage in view of a reduction of the motor mass due to the combination between the FSCW and the SPM configuration.

2.4 Electric drive

In order to reduce the car mass, a simple power-train architecture has been selected. It is composed by synchronous electric machine (EM) directly connected at the rear wheel by a fixed gear, a bi-directional single stage power converter and a battery pack. The block scheme of the system is shown in Fig. 6.6.

The power converter, that has been adopted for this electric vehicle, is a simple but effective single stage three phase inverter. Its DC bus is directly connected to the vehicle Energy Storage System (ESS) whose voltage V_{DC} is fixed to 300 V. The main power converter characteristics are reported in Table 6.2.

A losses analysis has been carried out in order to estimate the inverter efficiency. The losses in a power converter are the conduction losses and the switching losses in its devices. The estimate efficiency has been computed by using the device characteristics [35]. In IGBT devices the switching losses $P_{switching}$ and conduction losses $P_{conduction}$ have been calculated by following formulae [36]

$$P_{switching} = (E_{ON} + E_{OFF}) \cdot f_{sw} \quad (2.5)$$

$$P_{conduction} = v_{ON} \cdot i_D \quad (2.6)$$

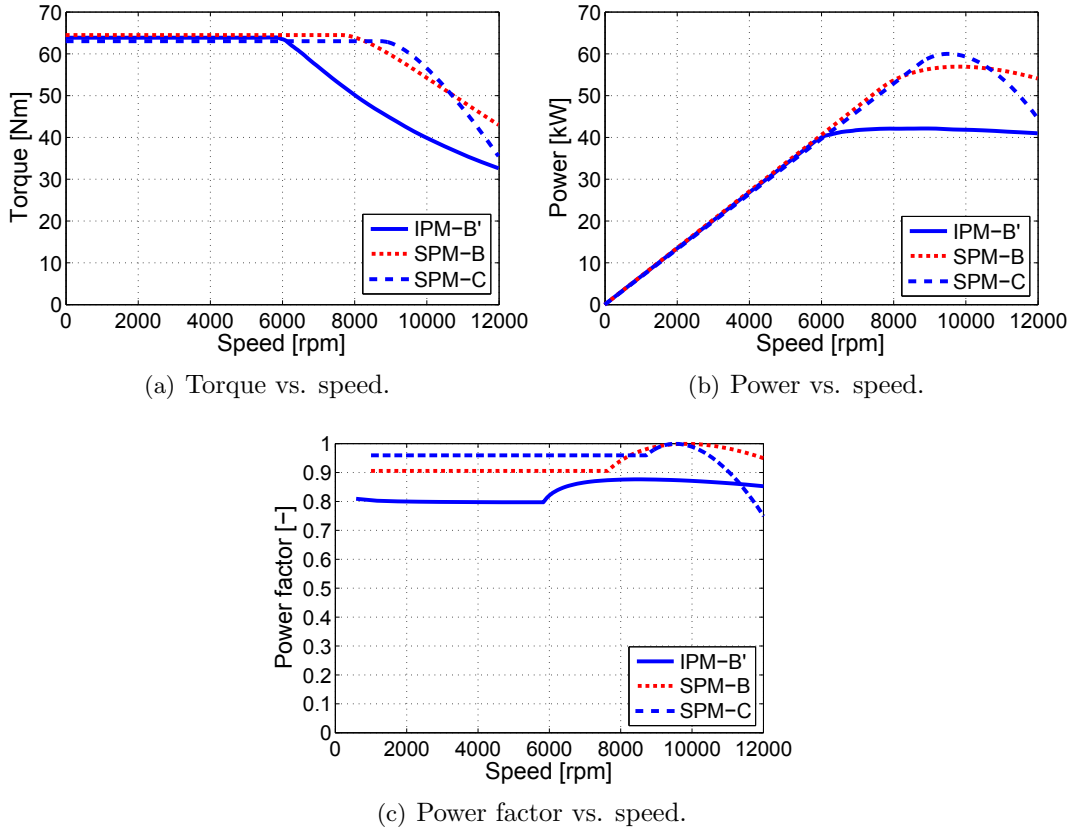


Figure 2.7: Performance comparison.

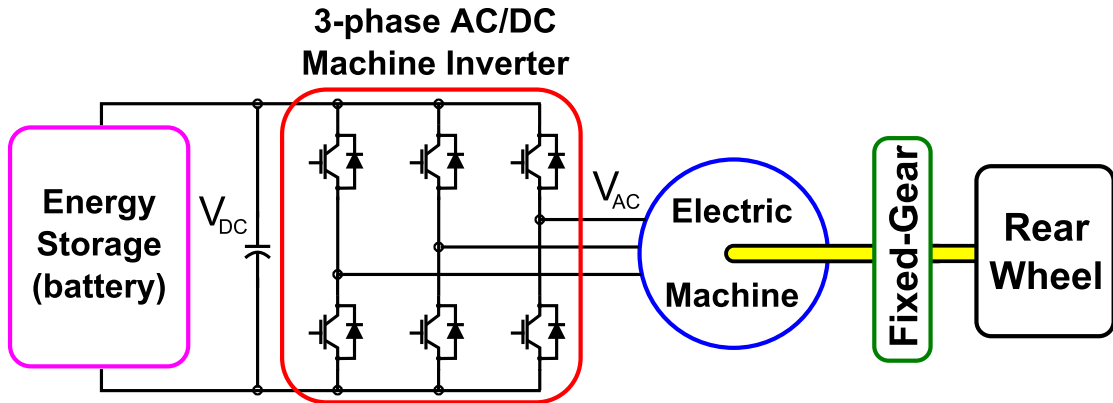


Figure 2.8: EV power-train sketch overview.

where v_{ON} is equal to $2 V$ when the devices is in conduction, i_D is the device current, f_{sw} is the switching frequency, E_{ON} is the turn-on switching energy and E_{OFF} is the turn-off switching energy. These energies are roughly proportional to the device current and as an example are $E_{ON} = 16 mJ @ 150 A_{RMS}$ and $E_{OFF} = 8 mJ @ 150 A_{RMS}$. The converter constant efficiency loci are reported in the torque vs. speed plane of Fig. 2.9

Table 2.4: Key machine parameters summary, gear ratio 1 : 8.

Design	IPM-B'	SPM-B	SPM-C	Unit
D_e	276	276	276	<i>mm</i>
D	180	180	210	<i>mm</i>
L_{stk}	40	40	40	<i>mm</i>
n_{MAX}	12000	18320	13280	<i>rpm</i>
n_B	5832	7639	8717	<i>rpm</i>
T_n	63	63	63	<i>Nm</i>
I_n	127	156	168	A_{RMS}
J_n	12.9	13.2	11.2	A_{RMS}/mm^2
Λ_{PM}	13.6	101	43.8	<i>mVs</i>
I_{ch}	30	163	425	A_{RMS}
n_{cs}	6	5	13.5	–
G_{Cu}	5.0	5.0	2.1	<i>kg</i>
G_{PM}	0.7	1.0	1.1	<i>kg</i>
G_{Fes}	9.0	9.0	6.0	<i>kg</i>
G_{Fer}	4.2	5.8	8.5	<i>kg</i>
G_{Fe}	13.2	14.8	14.5	<i>kg</i>
G	18.9	20.8	17.7	<i>kg</i>

Table 2.5: three-phase inverter parameters.

Parameter	Value
Number of phases	3
Type of switch	IGBT
Switching frequency	10 <i>kHz</i>
Dead time	2 μ <i>s</i>
Maximum DC bus voltage	300 <i>V</i>
Rated AC current	180 A_{RMS}
Rated AC voltage	120 V_{RMS}

for the most promising candidates, IPM-B' and SPM-C. It highlights that IPM-B' drive exhibits higher efficiency starting from 4000 *rpm* with respect to SPM configuration. This is due to a lower rated current (about 70%). From the base speed working point, the converter efficiency of SPM-C machine decreases and the PF reduces, as previously mentioned.

In order to choose a proper ESS, a few preliminary consideration are introduced. With the rated total power fixed to 80 *kW* it is necessary an ESS size of about 8–10 *kWh* [37]. Considering the ESS data reported in [37], the mass of the battery has been estimated to be about 80 *kg* and 140 *kg* for Li-ion and Ni-MH technology respectively. Fig. 2.10 shows a typical spider-chart for the two battery type, representing the multi-objective function that allows to choose the best ESS. A comparison of the two solutions with the goal to choose the best trade-off between cost, volume and mass, emphasizes as the best candidate the Li-ion type, especially in the perspective of a minimization of

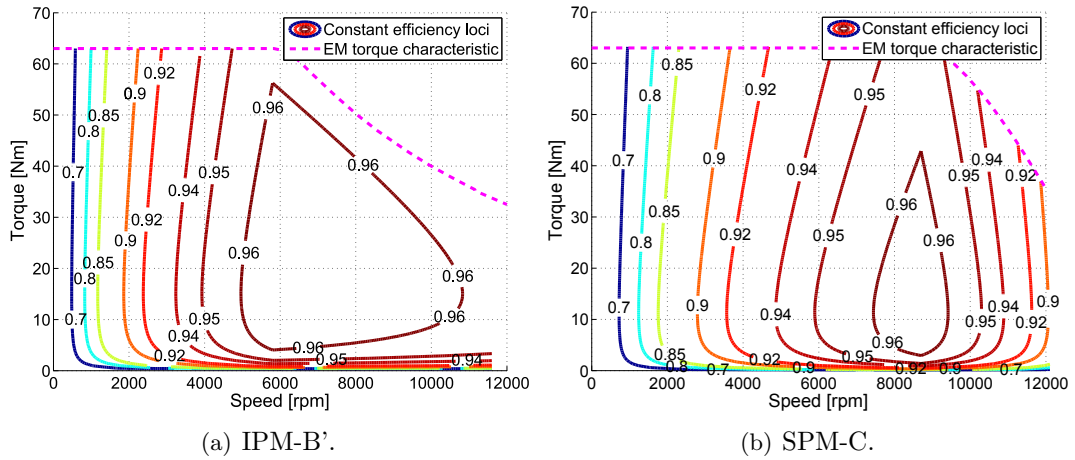


Figure 2.9: Power converter efficiency map.

the total mass.

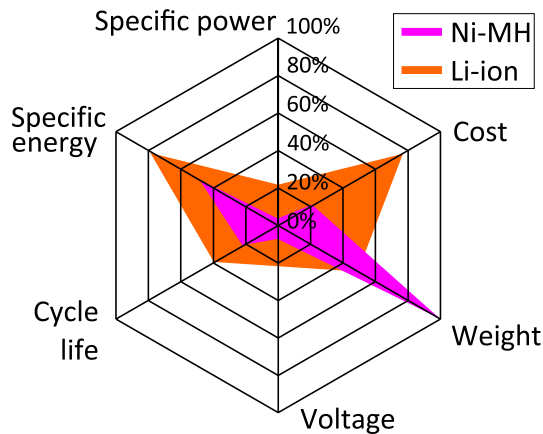


Figure 2.10: Batteries comparison.

2.5 Conclusions

This research confirms the feasibility of the realization of an high performance ferrite IPM motor for a formula SAE EV. The motor specifications have been estimated in accordance with the performance requirements of the competition and two gear ratios have been considered in order to achieve a size reduction. On the basis of different stator laminations, two ISDW IPM motors, with the same number of slots and poles, have been designed, optimized in terms of torque ripple and compared. Finally, a further comparison has been carried out with two equivalent size rare earth SPM machines, one equipped with the same stator lamination and number of poles, while the second is provided with a FSCW.

The results highlight that the proposed IPM design exhibits the best torque vs. speed trend for the application. Even if the proposed SPM machines show the highest torque density, especially for the FSCW configuration, the electromechanical performance over the base speed prove to be not suitable although the short FW area. In order to satisfy the torque requirements at high operating speed, a reduction of the number of conductors proves to be necessary. This is an important drawback because it yields to an increase of the phase current, making mandatory an oversizing of the power supply system (inverter and ESS). For these reasons this research emphasizes that the proposed IPM design is the most suitable solution because combines high performance in a wide speed range with a cost reduction due the adoption of rare-earth free magnet.

Chapter 3

PM Volume Dimensioning in Permanent Magnet Assisted Synchronous Reluctance Motors

This chapter presents a comparison of the performance of synchronous reluctance motors suitable for automotive applications. A 36-slot, 4-pole SynR motor, equipped with a multiple barrier rotor, has been considered as reference machine. Three different PMA SynRs, with the same rotor structure of the SynR machine but different PM dimension, have been analysed for comparison. Fig. 3.1 shows the considered geometries. This research aims to highlight the influence and benefits of using ferrite magnets on the machine performance, emphasizing the importance of a careful evaluation of the magnet volume in order to increase the performance while reducing the used quantity. Several parts of this project have been presented by the author in international conferences. In particular, in this Chapter, the work presented in [38] is widely described.

3.1 Design procedure overview

The stator design procedure is the same of that of induction motors (IM) or IPM machines. The rotor design, instead, has several degrees of freedom. The shape, the thickness of the flux barriers and their angle are important design variables in order to achieve suitable performance [21, 27, 18].

Regarding the winding topology, a strong interest focused on Fractional Slot Concentrated Winding (FSCW). Comparing to Distributed Winding (DW), they exhibit important advantages, such as manufacturing simplicity and higher power density. On the other hands, this winding carries an higher Magneto Motive Force (MMF) harmonic content that can yield to a drastic increase of the rotor losses [26]. This phenomenon could lead to a noticeable reduction of the efficiency, especially in high speed operation. Finally, the anisotropy achievable in a FSCW machine is lower [32, 33, 39], limiting one of most important peculiarity of reluctance machine, the saliency ratio. For these reasons a non-chorded DW has been selected for the designs.

The main constraint of the machine is represented by the dimensions of stator lam-

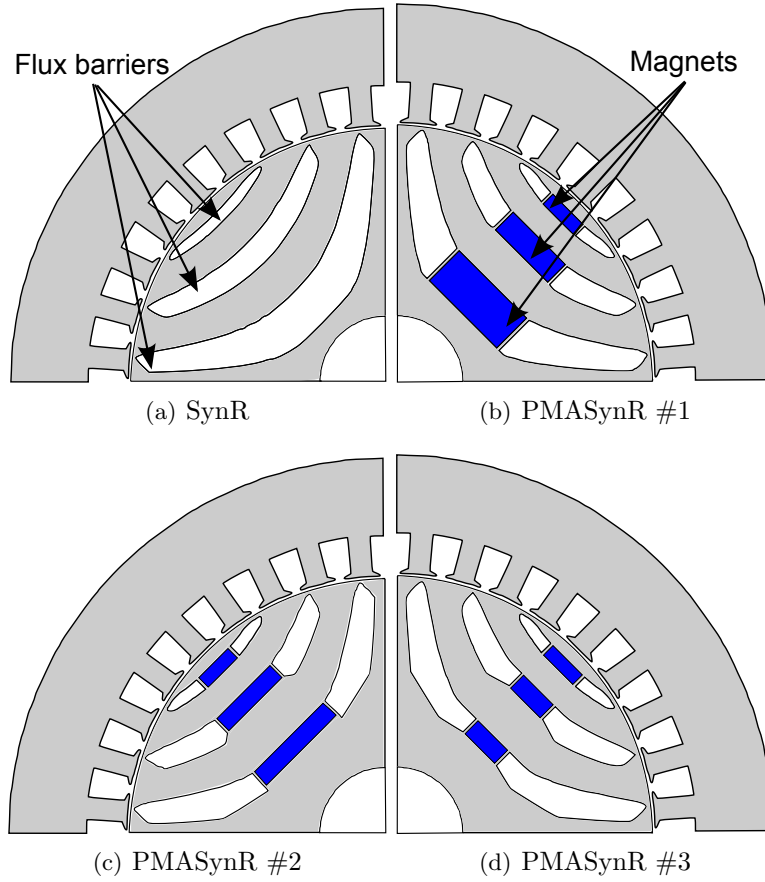


Figure 3.1: Sketch of SynR and PMASynR motors equipped with three flux barriers per pole and different PM dimensions.

Table 3.1: Machine constraints summary.

Maximum speed	8000 rpm
Base speed	1700 rpm
Rated torque	240 Nm
DC rated voltage	300V
Current density	6A/mm ²
Number of slots	36
Number of poles	4
Airgap diameter	230 mm
Outer diameter	337 mm
Airgap height	0.7 mm

Table 3.2: Ferrite PM parameters summary,

Remanence flux density	0.4 T @ 20Â°C
Knee flux density	0.15 T (0.25 T design) @ 20Â°C
Recoil permeability	1.05

ination. As reported in Table 3.1, a 36-slot 4-pole stator is considered, with the inner diameter equal to 230 mm. The airgap height is constrained to 0.7 mm.

A SynR machine, equipped with a three flux barriers rotor, has been firstly studied by means of Finite Element Analysis (FEA). The stack length has been scaled according to the requested rated torque (240 Nm) and the design current density (6 A/mm²). The number of series conductors per each slot has been selected equal to 3, in order to achieve a base speed close to 1700 rpm at the rated voltage (300 V DC bus).

Since the torque ripple is high, an automatic optimization procedure, based on a Non-dominated Sorted Genetic Algorithm (NSGA), has been performed with the objective of minimize the torque ripple changing the flux barrier angles and the ratio between air and iron path along the q -axis. The best solution, with a torque ripple of 16.9%, without skewing, has been selected.

Table 3.3: PM dimensions of PMASynR geometries.

1 st	7 × 21mm	7 × 21mm	7 × 21mm
2 nd	12 × 35mm	9 × 35mm	9 × 21mm
3 rd	20 × 45mm	9 × 45mm	9 × 21mm

The SynR motor has been considered as baseline geometry and compared with three PMASynR motors. The ferrite PM dimensions, shown in Table 3.3, has been selected in order to be suitable for each flux barrier. The 1st flux barrier is that closer to the periphery of the rotor, while the 3rd is that close to the rotor shaft.

PMASynR #1 represents the first analysed machine while, in the subsequent configurations, a minimization of the PM quantity has been performed as follows. In PMASynR #2 the PM widths are not changed, while their heights has been reduced, nearly halving the PM volume. The last configuration, PMASynR #3, has uniform PM widths, equal to those in the 1st flux barrier, while the heights remain constant, as in the previous one. This yields to a reduction of the PM volume of about 65%.

3.2 Analysis of the performance

The current space vector trajectory has been evaluated by means of FEA, changing the d - and q - axis currents and computing the d - and q - axis flux linkages and torque. Fig. 3.2 shows this trajectory for the machines, according to the Maximum Torque Per Ampere (MTPA) locus and Flux Weakening (FW) up to the maximum speed (8000 rpm). It is worth noticing that the FW trajectory for PMASynR motors does not include the Maximum Torque Per Volt (MTPV) locus and it proves to be not substantially affected by the chosen variation of the PMs dimension. The resultant base speed, for both typologies, is around 1700 rpm.

Fig. 3.3 shows the resultant current vs. speed behaviour. Due to the previous different current trajectories, these trends are completely different in FW operation, and for the PMASynR motors, the control provides to keep the current on the rated value limit up to the maximum speed.

In constant torque speed range, due to the presence of PM flux linkage Λ_{PM} and so an additional PM torque, the rated current for all PMASynR machines is about 7%

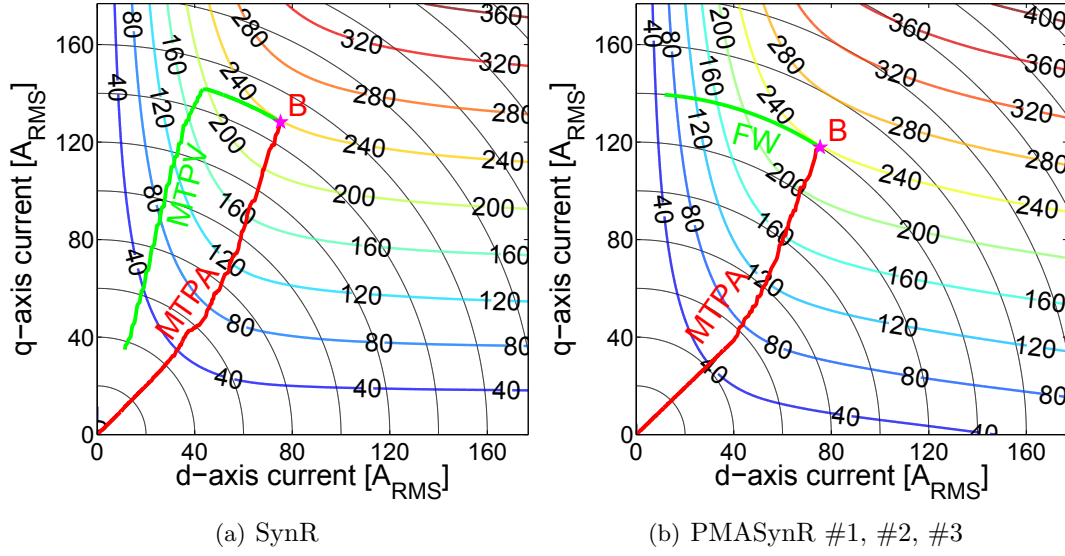


Figure 3.2: Current space vector trajectory: constant torque contour map.

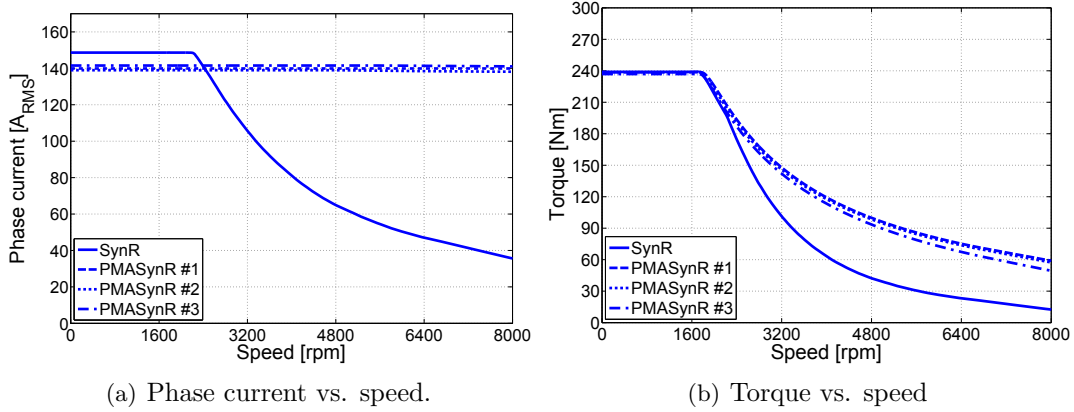


Figure 3.3: Current and Torque vs. speed behavior.

lower. It is equal to $140 A_{RMS}$, in comparison of $150 A_{RMS}$ of SynR motor. Moreover, the contribution of the reluctance torque component to the total does not change. As reported in Table 3.4, the saliency ratios in the base point ξ_B , equal to the ratio between the d - and q - axis apparent synchronous inductances, L_{dB} and L_{qB} respectively, are essentially unchanged.

The torque and power vs. speed characteristics are shown in Figs. ??, 3.4 respectively. The introduction of the PM causes the PMASynR motors to exhibit a satisfactory Constant Power Speed Range (CPSR). In particular the best CPSR is achieved for PMASynR #1 and #2. This excellent FW behaviour is confirmed by the values of the characteristic current I_{ch} , reported in Table 3.4, that result close to the rated current I_n ($I_{ch} = \Lambda_{PM}/L_q = I_n$) [34].

Finally, Fig. 3.4 shows a comparison between the Power Factor (PF) trends. All

Table 3.4: Main motor parameters.

Motor	SynR	PMASynR		
		#1	#2	#3
Λ_{PM} (mVs)	0	72.3	70.0	40.8
L_{dB} (mH)	4.4	4.3	4.4	4.4
L_{qB} (mH)	0.41	0.41	0.45	0.45
ξ_B (-)	10.7	10.5	9.8	9.8
I_{ch} (A _{RMS})	0	139	122	70

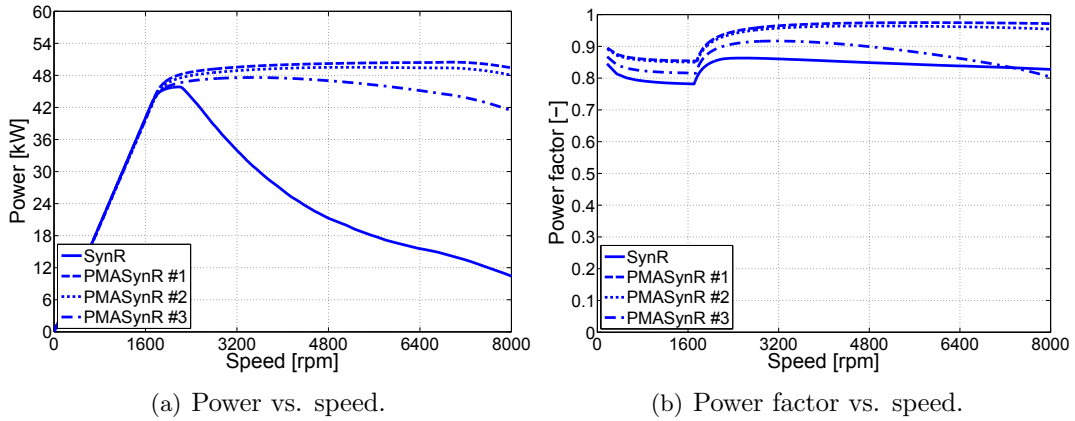


Figure 3.4: Power and Power Factor vs. speed behavior.

the machines exhibit a PF higher than about 0.8 in the whole speed range. Anyway, the performance of PMASynR, in particular #1 and #2, are higher and similar to each other, reaching, in FW, values around 0.95. This behaviour is caused by the effect of compensation of Λ_{PM} , that adding to the q -axis flux linkage component $L_q \cdot I_q$, rotate the resultant flux linkage vector out of phase close to 90 degrees with respect the current vector. On the contrary, the PF of the PMASynR #3 decrease significantly at high speed range, reaching the same values of SynR machine. This trend emphasizes that this last selected PM dimensions does not yield to an optimal compensation.

Among the three considered PMASynR geometries, #2 proves to be the optimal design, because it combines a significant reduction of the ferrite PM, without affecting the performance in terms of torque, CPSR and PF.

3.3 Conclusions

In this chapter the influence of the ferrite PM quantity on the performance of a PMASynR motors has been investigated, highlighting the trade-off between the minimization of the magnet and motor performance. Three PMASynR configurations, based on a SynR motor optimized in terms of torque ripple, have been considered. A FEA has been carried out in order to evaluate and compare the electromechanical performance. The insertion of the ferrite in the SynR geometry improve the PF and CPSR, satisfying the rated power requirements at maximum speed, without substantially increase the machine cost, due

the low price of the ferrite. The minimization of the PM volume is to envisage. On the other hands, it is essential to assess the compromise between the loss of the performance with the optimization of the used PM quantity.

Chapter 4

Sensitivity Analysis of Torque Ripple Reduction of Synchronous Reluctance and Interior PM Motors

Adopting a rotor configuration characterized by several flux barriers per pole, there is a high influence of the rotor geometry on the machine performance, in terms of both average torque and ripple. Therefore, an optimization is often required to the aim of determining a rotor geometry achieving a high and smooth torque. The optimal geometry should guarantee good performance for various operating points (i.e., changing the current amplitude and phase). In addition, small geometry variations, due to mechanical tolerance, wear of the machine tools, manufacturing or assembling inaccuracy, and so on, should only marginally affect the performance of the optimal machine. This chapter investigates this aspect, showing the results of various optimizations carried out on different machines. The impact of various geometry parameters is taken into account. The difficulty to get a robust geometry as far as the torque ripple reduction is highlighted. Finally, a few experimental results on a Synchronous Reluctance motor prototype will be presented, compared with Finite Element Analysis simulations for validation. Several parts of this project have been presented by the author in international conferences. In particular, in this Chapter, the work presented in [40] is widely described.

4.1 A brief review of techniques to reduce torque ripple of SynREL and IPM machines

A common drawback of the SynREL and IPM machines is their high torque ripple [25]. This is caused by the interaction between the spatial harmonics of magneto-motive force (MMF) due to the stator currents and the rotor geometry. The main harmonic of stator MMF is synchronous with the rotor and produces the average electromagnetic torque. The other harmonics are not synchronous and cause variations of the flux across the flux barriers, that is, oscillations of the rotor magnetic potential. The main effect is a

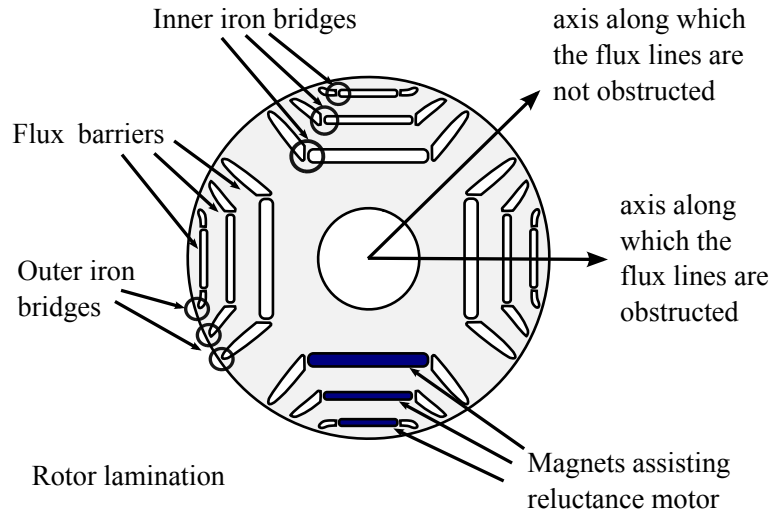


Figure 4.1: Sketch of a four-pole synchronous reluctance rotor with three flux barriers per pole. The synchronous PM assisted reluctance motor is achieved when PMs are inset in the flux barriers.

high torque ripple.

In [27] it has been shown that the rotor skewing (commonly adopted in PM machines [41, 42]) is not enough to smooth the torque. In any case, only a step-skewing is possible when PMs are used: the rotor is split in two or more parts, each of them is skewed with respect to the others. It has been also shown that a reduction of the torque ripple can be achieved by means of a suitable choice of the number of flux barriers with respect to the number of stator slots. In this case the flux barrier ends are uniformly distributed along the airgap (similarly to the stator slot distribution). In [43] and then in [44], the flux barriers are shifted from their symmetrical position. In this way, a sort of compensation of the torque harmonics is achieved. This technique is similar to that proposed in [45] for cogging torque reduction in surface-mounted PM motors.

Alternatively, a strategy to compensate the torque harmonics of the SynREL motor is presented in [21] by adopting two different flux barrier geometries in the same lamination, the resulting motor is referred to as "Machaon" motor (the name of a butterfly with two large and two small wings), since the flux barriers of the adjacent poles are large and small alternatively. A picture of a "Machaon" rotor lamination is shown in Fig. 4.2. In this case, not only the geometry of the flux-barriers is different in the adjacent poles, but also the number of the flux-barriers per pole. In the middle of each flux barrier, small PMs (the assisting PMs) can be added so as to saturate the iron bridges and to increase the power factor.

4.1.1 Reference geometries

Besides investigating the torque behavior, it is important to establish the influence of the various design parameters. Fig. 4.3 shows the main variables in the design space:

- D is the inner diameter;



Figure 4.2: Photo of a Machaon rotor lamination, characterized by the combination of two and three flux barriers per pole.

- h_{so} is the slot opening height;
- w_{so} is the slot opening width;
- g is the airgap;
- ϑ_{b1} , ϑ_{b2} , and ϑ_{b3} are the flux barrier angles;
- L_{air} is the total thickness of the three flux barriers along the rotor q -axis;
- $L_{air} + L_{fe}$ represents the rotor radius.

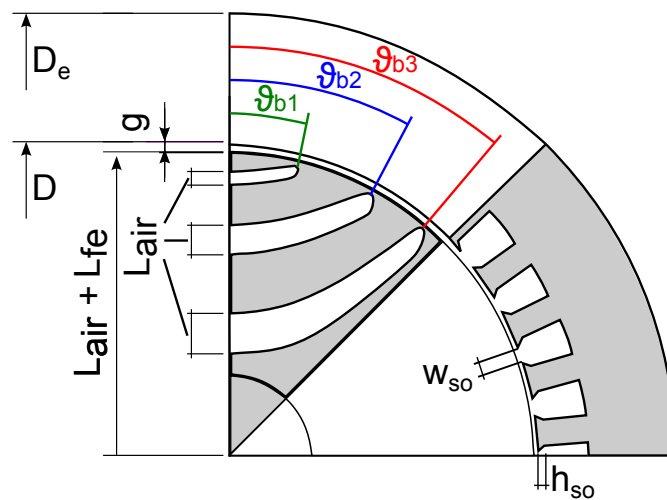


Figure 4.3: Layout of the variable parameters.

Three different 36-slot 4-pole SynREL machines are considered in this study. Table 4.1 reports the main dimensions. Two of them (*A* and *C*) have a symmetrical rotor, while the third one (*B*) has a Machaon rotor structure. In order to guarantee a proper saliency ratio an Integral Slot Distributed Winding (ISDW) has been chosen. Since these machines present an high anisotropic rotor, has been demonstrated that this winding arrangement is the most effective solution comparing to Fractional Slot Concentrated winding (FSCW) [33, 32]. The saturation of the machine is strongly dependent by the

Table 4.1: Main geometrical dimensions

Motor	<i>A</i>	<i>B</i>	<i>C</i>	<i>unit</i>
D_e	340	200	135	mm
D_{re}	230	125	80	mm
L_{stk}	250	70	60	mm
<i>Poles</i>	4	4	4	-
<i>Slots</i>	36	36	36	-
g	0.7	0.5	0.3	mm
k_{air}	0.4	0.4/0.45	0.4	mm
T_n	260	20	7	Nm

thickness of the flux barriers. It is common to define an insulation coefficient k_{air} as a ratio between L_{air} and the iron thickness along the rotor q -axis (neglecting shaft radius). Each flux barrier's thickness (reported in Table 4.1) has been determined through FE test simulations, in order to obtain a desired saturation level of the iron paths.

The thickness of the iron bridges of each rotor has been chosen according to the maximum speed required for each application. For the sake of comprehension, referring to Fig. 4.1, the inner iron bridges has mainly to guarantee a robust structure and resist to the centrifugal forces insisting on rotor parts. Also the outer iron bridges, in the following sections called iron ribs, even if they are less mechanically stressed with respect to the outer ones, have a structural function. Some details on the impact of the iron ribs thickness with respect to torque ripple are highlighted in Section 4.2.

4.1.2 Validation by means of experimental results

Before comparing the torque behavior of different solutions, the finite element predictions are compared with experimental results. Several tests have been carried out and the results are compared with finite element (FE) simulations. As an example, referring to motor B, Fig. 4.4 shows the comparison between experimental measurements and the simulation results. Under low load condition the comparison confirms the satisfactory agreement between test results and predictions. Under high load condition, FEA overestimates the torque, probably due to a slightly different saturation effect of the iron. The offset on the average torque is lower than 4% and the waveforms resulting from FE simulation and measurements are showing the same oscillation.

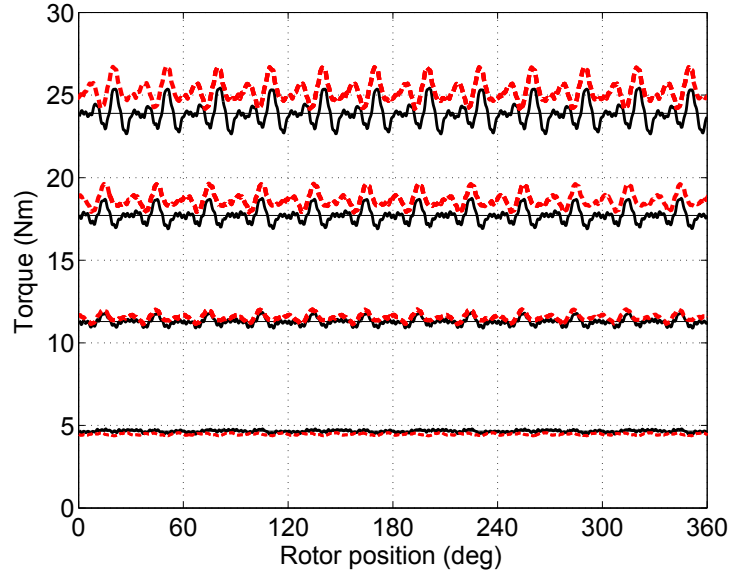


Figure 4.4: Torque versus rotor position: experimental results (continuous line) vs FE simulation (dashed line), motor B).

4.2 Analysis of torque ripple

Torque behavior is calculated by means of finite element analysis, moving the rotor of 60 electrical *degrees*, corresponding to a torque ripple period for a three-phase machine. The stator windings are fed by given I_d and I_q currents. The electromagnetic torque is computed by means of the Maxwell stress tensor along the airgap surface. As previously mentioned, the main difficulty in designing a SynREL motor is to achieve an acceptable torque ripple. Torque ripple amplitude is defined as

$$\Delta T = \frac{T_{max} - T_{min}}{T_{avg}} \quad (4.1)$$

An example of torque vs. angular position for the motor A, is shown in Fig. 4.5. Fig. 4.5 also shows how the torque ripple varies according to the variation of flux barrier angles. A small variation from 37.5 to 39 degrees, of the third flux barrier angle ϑ_{b3} , has been considered.

It can be noticed that while the average torque remains almost the same (the variation is less than 4%), the variation of the third flux barrier angle can affect significantly the torque ripple (ΔT varies from 32 to 40.7%). To highlight the impact of such a variation it is useful to analyze the harmonic content of the torque ripple as shown in Fig. 4.6. In 36-slot 4-pole machine the higher torque ripple amplitudes are expected for harmonic of order 18, 36 etc which are the slot harmonics. The first configuration exhibits high torque harmonics corresponding to the order 18 and 36 (the slot harmonics). The second configuration exhibits a low torque harmonic of order 18, but a high harmonic of order 36 (amplitude of about 30 Nm over an average torque of 260 Nm). The variation in the rotor flux-barrier geometry yields an appreciable change in the torque harmonic distribution.

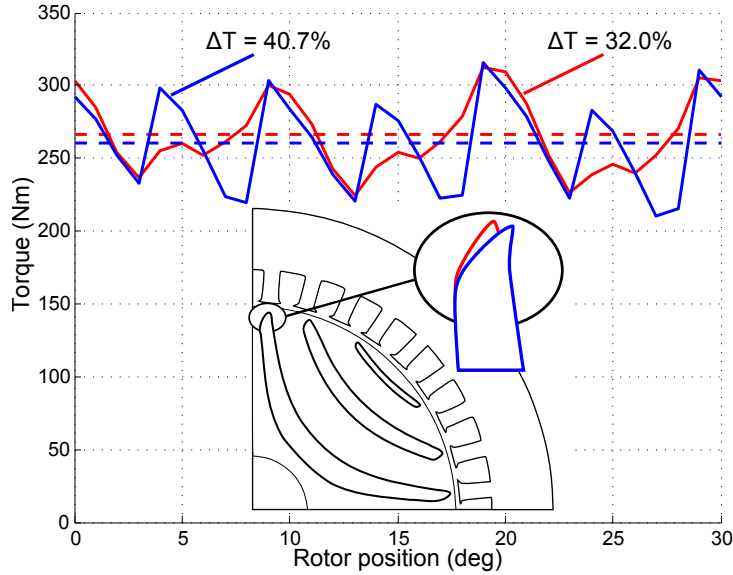


Figure 4.5: Ripple torque due to a variation of the flux barrier angles in the airgap region (motor A).

Similar analysis has been carried out on other motors. For instance let us refer to the motor C with $\vartheta_{b1} = 14.6 \text{ deg}$, $\vartheta_{b2} = 26.3 \text{ deg}$ and $\vartheta_{b3} = 39 \text{ deg}$. A variation of two flux barrier ends is considered, with $\vartheta_{b2} = 26.1 \text{ deg}$ and $\vartheta_{b3} = 38.6 \text{ deg}$ respectively. As shown in Fig. 4.7, the amplitude of low order harmonics changes significantly.

Always referring to motor C, another interesting comparison can be done for different airgaps, when the flux barrier ends angles are fixed ($\vartheta_{b1} = 14.6 \text{ deg}$, $\vartheta_{b2} = 26.3 \text{ deg}$ and $\vartheta_{b3} = 39 \text{ deg}$). The different harmonic contents are shown in Fig. 4.8. Increasing the airgap from 0.2 to 0.4 mm, it is noticed the torque harmonic of 18th order growth and a smoothing effect for higher harmonics. A further effect of the airgap increase is the reduction (about 15%) of the average torque and a consequent worsening of the relative torque ripple of about 5%. These results highlight that small variations in rotor geometry cause substantial change in motor performance. For this reason, it is interesting to investigate the variation of the several design variables SynREL and PMAREL motors present. To this aim, it is useful to represent the variation of the torque ripple due to different combinations of design variables on a plane.

At first, for a given flux barrier angle ϑ_{b3} (38.8 deg) the impact of the flux barrier angles ϑ_{b1} and ϑ_{b2} on torque ripple is considered. The torque ripple resulting from FE analysis is represented on the variable plane shown in Fig. 4.9. In this case, the variation of ϑ_{b1} and ϑ_{b2} gives different effects on torque ripple.

The variation of the first barrier angle ϑ_{b1} does not change the torque ripple significantly. On the contrary, the variation of ϑ_{b2} causes a variation up to 20% in the considered range. It is worth noticing that a 0.5 deg variation of ϑ_{b2} (this is highlighted by black circles, from the optimal to the changed solution) leads to a variation of torque from 10 to 26%. Anyway, Fig. ?? shows that the resultant average torque seems to be not strongly affected by the flux barrier angles, remaining almost constant for each ϑ_{b1}

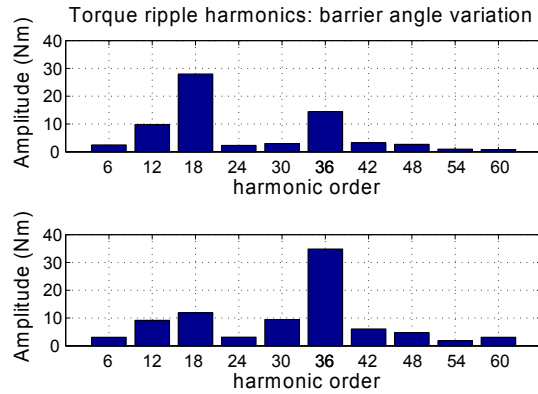


Figure 4.6: Torque ripple harmonics comparison due to a variation of ϑ_{b3} harmonic order refer to an electrical period, Motor A of Fig. 4.5

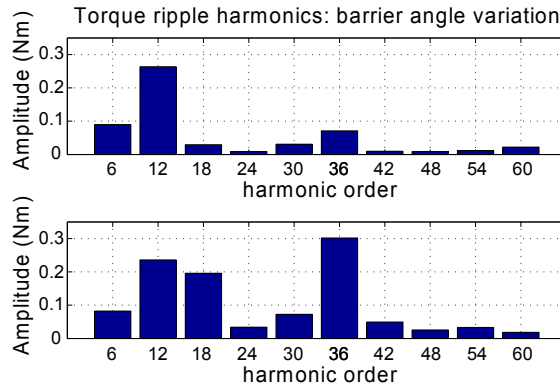


Figure 4.7: Torque ripple harmonics comparison due to a variation of ϑ_{b2} and ϑ_{b3} . Motor C, with symmetrical rotor.

and ϑ_{b2} combination. Similar results can be represented considering a variation of ϑ_{b2} and ϑ_{b3} , while ϑ_{b1} is fixed (14.8 deg), as represented in Fig. 4.10. The influence of the flux barrier angles on torque ripple depends on both ϑ_{b2} and ϑ_{b3} . For some values of ϑ_{b3} , the variations of ϑ_{b2} yield no effect on torque ripple, as shown in the bottom part of Fig. 4.10. For some other values of ϑ_{b3} , the angle ϑ_{b2} has to be selected properly in order to minimize the torque ripple, as shown in the top part of Fig. 4.10. It is also worth noticing that a generic variation of 0.3 deg for ϑ_{b2} yields a higher torque ripple with respect to the same variation of ϑ_{b3} . Anyway, the average torque results to be not significantly affected by flux barrier angles variation. It is worth noticing that, while other techniques used with the aim of reducing the torque ripple affect the average torque developed by the motor (e.g. shifting, shaping, skewing, step-skewing), the suitable choice of the flux barrier angles yields a reduction of the torque ripple only (as confirmed by the results obtained). The average torque remains fundamentally constant during the optimization process. Combining the representation of all the flux barrier angles of Figs. 4.9 and 4.10, a set of variables giving an optimum solution can be carried

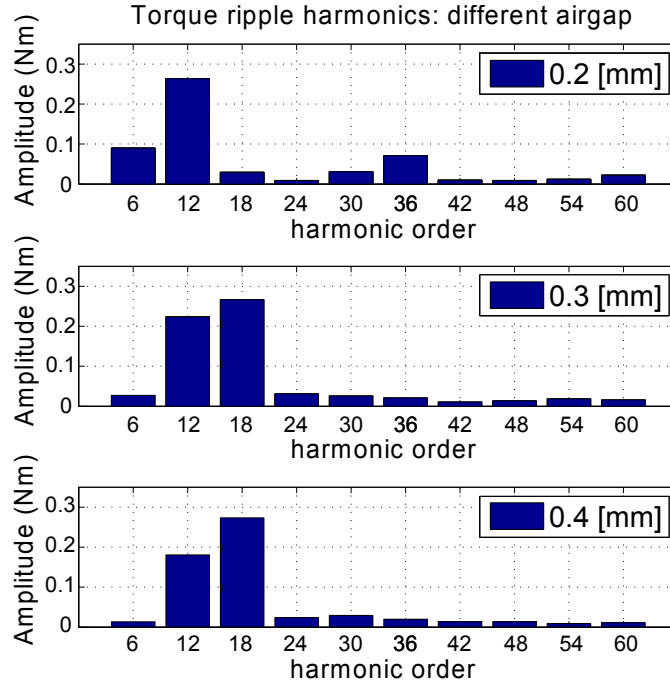


Figure 4.8: Torque ripple harmonics comparison due to variation of the airgap. Harmonic content of ripple torque referred to an electrical period: different airgap considered (Motor C).

out. Such a solution is matching the final result given by the optimization process (as discussed in Section 4.3). The results presented above are important in the first stage of the design process. They highlight those variables which have more influence on motor performance (i.e. ϑ_{b2} and ϑ_{b3}) with respect to the others.

Fig. 4.11 shows the percentage torque ripple as a function of the rotor outer diameter D_{re} (considering a fixed inner stator diameter) and the iron rib thickness. The larger D_{re} the smaller the airgap. Referring to the motor C, a variation of D_{re} from 78.6 to 79.6 mm, corresponds to an airgap variation between 0.75 and 0.2 mm respectively. For smaller airgap the influence of the iron ribs on the torque ripple is negligible. On the contrary the rib thickness exhibits a heavy influence on the torque ripple for large airgap values (D_{re} lower than 78.9 mm). Once again, for larger iron ribs, the torque ripple increases and the airgap could have some influence on it. It is also important to notice that there is an optimal airgap that minimizes the ripple (in this case 0.3 – 0.35 mm for motor C). It has been also noticed that the inner iron bridges instead have no effect on torque ripple. However, their thickness have to be minimized in order to avoid an average torque reduction and at the same time improve the power factor. Fig. 4.11 shows the influence of the same variables on the average torque. The influence of the airgap is dominant with respect to the rib thickness. Similar results has been carried out for motor A. The oscillation of the torque with respect to the average value is also affected by other parameters related to the stator configuration at the air gap.

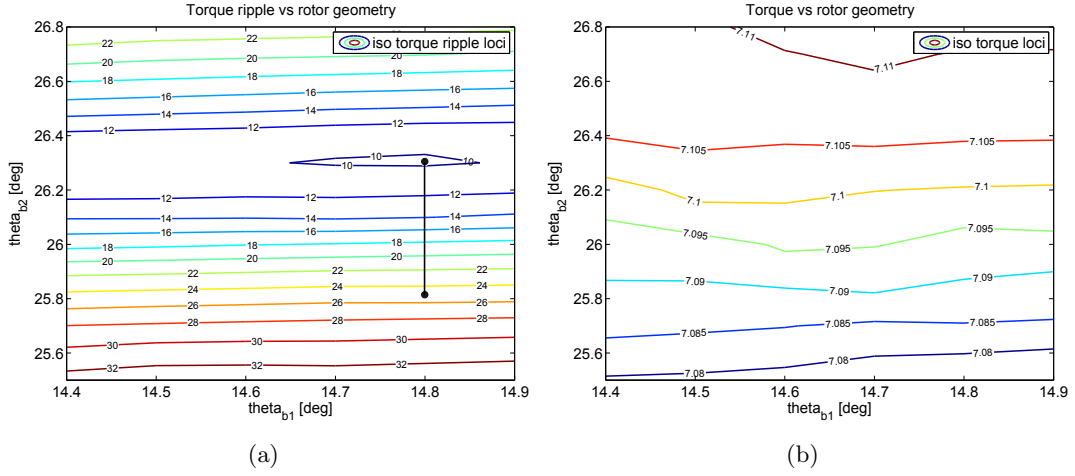


Figure 4.9: Percentage torque ripple (a) and average torque (b) as a function of the design variables ϑ_{b1} and ϑ_{b2} , with $\vartheta_{b3} = 38.8$ deg (Motor C).

For example, there is a negligible impact of the slot opening height h_{so} . On the contrary, the larger the slot opening width w_{so} the greater the torque ripple.

4.3 Optimized Reluctance Machines under analysis

Once the main motor dimensions has been fixed, from the application constraints or by means of analytical design, an optimization of the motor is becoming a common practice. The optimization variables have to be selected. The choice of the variables, together with their number, is a key task to obtain a suitable final solution. Due to the high impact of both rotor and stator design parameters on the torque behavior, genetic algorithms (GA) optimizations have been carried out, considering the minimization of the torque ripple as objective function.

Table 4.2: Optimization results (motor C)

Barrier angle	<i>Initial</i>	<i>Final</i>	<i>unit</i>
ϑ_{b1}	12.5	14.8	deg
ϑ_{b2}	27.5	26.3	deg
ϑ_{b3}	37.5	38.8	deg
ΔT	48.4	10.5	%

In particular, a strong impact of the angles of the flux barrier ends (i.e. ϑ_{b1} , ϑ_{b2} , ϑ_{b3}) has been found, as shown in the previous section. For this reasons, it makes sense to focus deeply on flux barrier geometry. As an example, Fig. 4.12 reports the

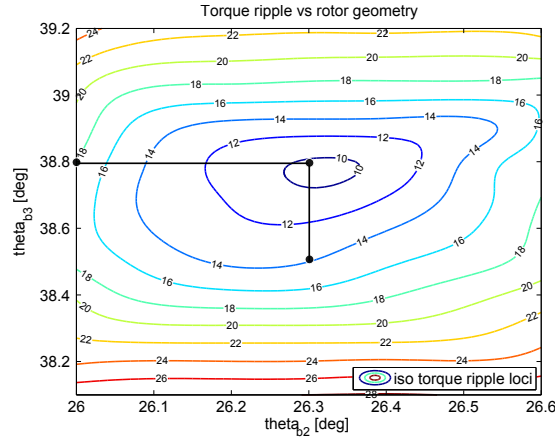


Figure 4.10: Percentage torque ripple for different design variables: ϑ_{b2} and ϑ_{b3} with $\vartheta_{b1} = 14.8 \text{ deg}$ (Motor C).

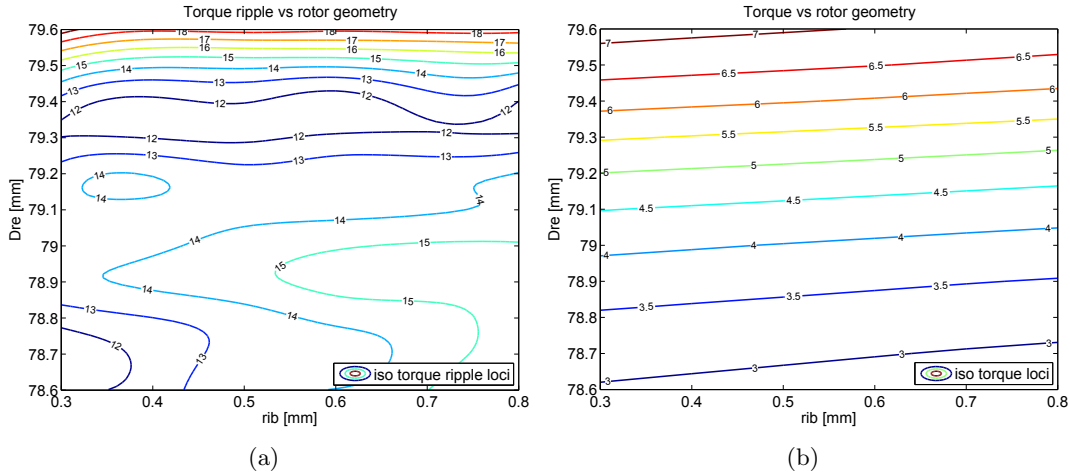


Figure 4.11: Percentage torque ripple (a) average torque (b) as a function of the airgap and the iron ribs thicknesses (motor C).

torque behavior versus rotor position is reported for the initial geometry and for the final (optimized) solution. The main optimization input and output data are given in Table 4.2. Fig. 4.13 and Fig. 4.14 show the optimization results for the SynREL motors A and C, with symmetrical rotor geometry. The angles of the flux barrier ends (the variables of the optimization) are plotted versus the corresponding torque ripple (the objective of the optimization). According to the objective of the torque ripple minimization, the best solutions are those on the left hand side of the figures. It is worth noticing that any variable converges to an optimal value in a tight range of variation. Thus, a set of best flux barrier angles can be done. The final optimization solutions for motors A and C, gives a ΔT of about 16.5% and 10.5% respectively. The obtained ripples agree with typical values of relative torque ripple ΔT for SynREL and PMAREL machines (without rotor skewing). A skewing of the rotor geometry,

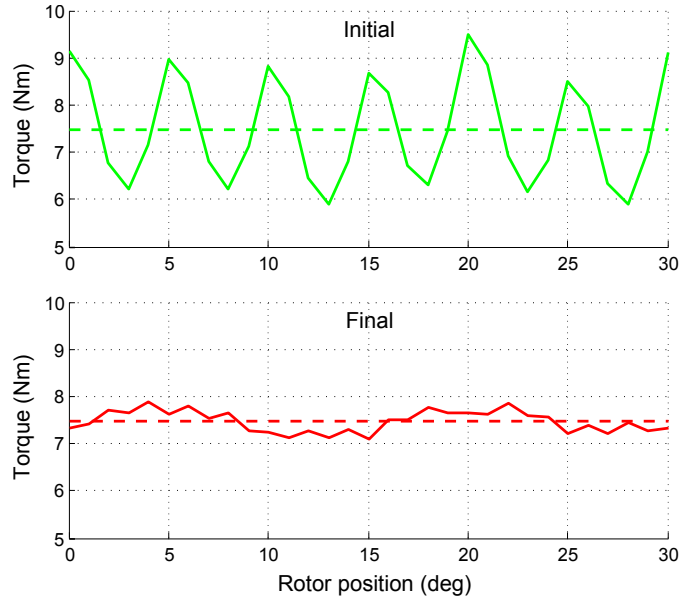


Figure 4.12: Torque vs. rotor position behaviors before and after optimization (motor C): initial and final geometry.

applied to the optimized motor (with $\Delta T = 10.5\%$), led to a further reduction of torque oscillation, slightly reducing the average torque. The same results are achieved for different motors, including the Machaon structure. In this case there are six flux barrier angles. The representation of Fig. 4.13 and Fig. 4.14 emphasizes that torque ripple increases (it almost doubles) with slight variations of flux barrier angles (they seem to be almost constant on the left hand side of the figures). In other words, slight variations of flux barrier angles cause a completely different behavior of the torque. This confirms the specific results shown in Figs. 4.5 to 4.8. These results highlight that once the optimal geometry is achieved, it is worth to evaluate the 'robustness' of such a solution. It is desirable that torque ripple results to be minimum even when occurring small variations of the working operating conditions (e.g., variation of current amplitude or phase) or small variations of the geometry (i.e. due to mechanical tolerance, wear of the machine tools, manufacturing or assembling inaccuracy, and so on). The sensitivity of the solutions found will be defined in Section 4.4.

4.3.1 Torque ripple sensitivity

At the end of the GA optimization, of both symmetric and Machaon configurations, several considerations about the torque ripple sensitivity to the parameters can be carried out. As a first step, the distance between two solutions is defined. A solution in the design space, e.g. the vector \vec{x} , is characterized by its n_v variables (e.g., $x_1 = \vartheta_{b1}$, $x_2 = \vartheta_{b2}$, $x_3 = \vartheta_{b3}$). The distance between the vector \vec{x}' and the vector \vec{x}'' results in

$$d(\vec{x}', \vec{x}'') = \sqrt{\sum_{i=1}^{n_v} (x_i'^2 - x_i''^2)} \quad (4.2)$$

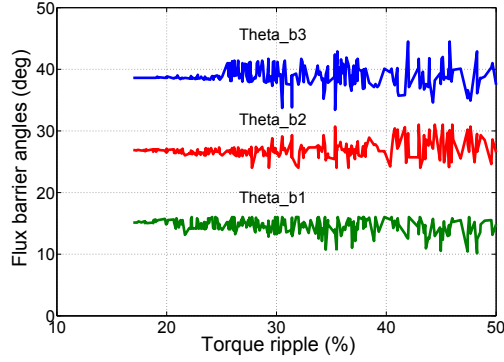


Figure 4.13: Optimization direction of the flux barrier angles referring to the torque ripple (motor A).

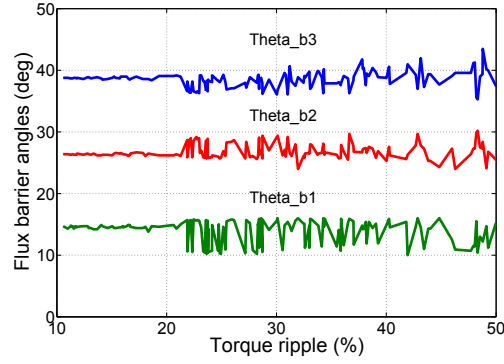


Figure 4.14: Optimization direction of the flux barrier angles referring to the torque ripple (motor C).

Let us refer to the geometry which exhibits the minimum torque ripple, resulting from the GA minimization. It is defined by the vector $\vec{\tilde{x}} = (\tilde{x}_1, \tilde{x}_2, \dots, \tilde{x}_n)$. The fluctuation of the torque ripple is computed according to the variation of the geometry with respect to the optimal solution $\vec{\tilde{x}}$, so as to evaluate the rate of change of the ripple with the deviation from the optimal solution, $\vec{\tilde{x}}$. Particularly important is the distance of a generic solution \vec{x} from the optimal solution:

$$d(\vec{x}, \vec{\tilde{x}}) = \sqrt{\sum_{i=1}^{n_v} (x_i^2 - \tilde{x}_i^2)} \quad (4.3)$$

Figs. 4.15 and 4.16 show the torque ripple versus the distance from the optimal solution, which corresponds to the point characterized by geometry variation equal to zero. Fig. 4.15 refers to a symmetric rotor, Fig. 4.16 to a Machaon rotor. In the latter case, the distance is computed according to six flux barrier angles. The solutions obtained for the Machaon rotor gives a high number of solutions exhibiting low torque ripple as results comparing the black circles in Figs. 4.15 and 4.16. At distance zero, there is the optimal solution $\vec{\tilde{x}}$ and the torque ripple is the minimum ripple, found by means of the

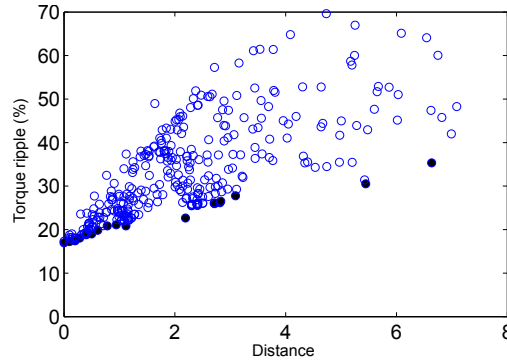


Figure 4.15: Torque ripple vs distance for a symmetric configuration (motor A).

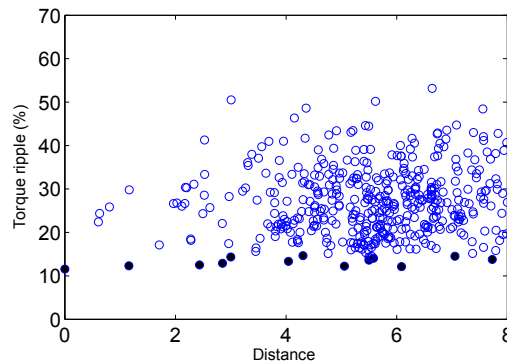


Figure 4.16: Torque ripple vs distance for a Machaon configuration (motor C).

GA optimization. As the distance from the optimal solution increases, the torque ripple increases, too. Such behavior is evident for both configurations.

It is also worth noticing that the torque ripple increases rapidly even for small geometry variations. The upper limits of such representations correspond to the worst case solutions, i.e. the set of solutions exhibiting the highest sensitivity of torque ripple with respect to geometry variations. Among the two configurations, the rate of change is slightly lower with the Machaon rotor. The Machaon configuration reduces some torque harmonics that cause torque oscillation. Therefore, such a solution results to be slightly more robust from the sensitivity point of view.

4.4 Sensitivity of the optimal solution

In order to evaluate the impact of the variables on the machine performance of the SynREL motor, an evaluation of the sensitivity is presented, according to the criteria given in [46]. This is an inexpensive evaluation since it is based on the analysis of all the solutions found during the GA optimization process.

At first, a perturbation space is defined in the design variable space, based on the definition of a hypercube in n_v dimensions.

The basic idea is to estimate the maximum variation rate of the torque ripple (the

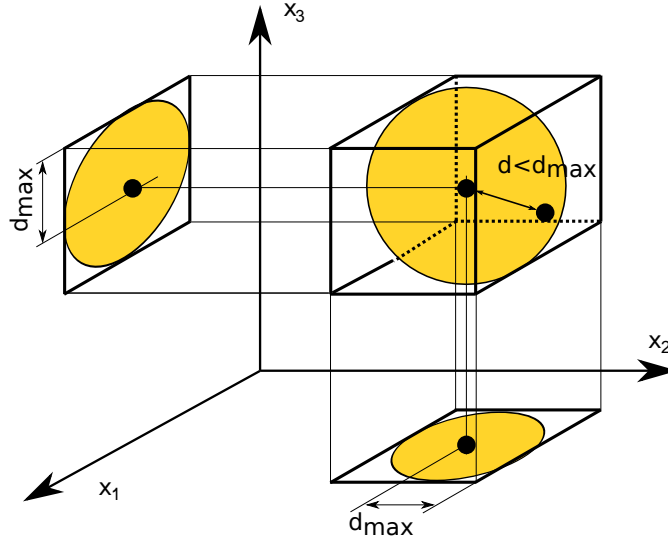


Figure 4.17: Design vector centered in the hypercube space of the feasible solutions.

objective function) in a perturbation space (the n_v -dimension hypercube) centered in a given design vector \vec{x} and composed of a number of feasible design vectors. For a given design vector \vec{x} , the associated hypercube is formed by all design vectors whose distance d from \vec{x} is lower than a fixed positive threshold.

Comparing all design points within the hypercube, the maximum and minimum value of the torque ripple is evaluated, i.e. ΔT_{max} and ΔT_{min} . Then, the sensitivity of the torque ripple in the design point \vec{x} is defined as their difference divided by the torque ripple achieved in the design point \vec{x} , center of the hypercube, that is, $\Delta T(\vec{x})$. It is

$$s(\vec{x}) = \frac{\Delta T_{max} - \Delta T_{min}}{\Delta T(\vec{x})} \quad (4.4)$$

Therefore, such a sensitivity can be evaluated in all the design space, adopting the information from the solutions of the GA optimizations that have been carried out. Fig. 4.18 shows the sensitivity defined in (4.4). The sensitivity to geometrical tolerances is higher and higher as the torque ripple is reduced. The lower the ripple torque, the higher the sensitivity. It becomes almost 10 times for the lower torque ripple. From the analysis, it seems that asymmetric rotor is slightly more robust than symmetric rotor, however the sensitivity to geometrical tolerances is high also in this case.

4.5 Effect of the PM on torque ripple

As said in the introduction PMs are commonly inset within the rotor flux barriers to saturate the iron bridges, improving the PF and the constant power speed range [38]. In this section the effect of the PM on the torque ripple is investigated. The PMAREL configurations considered, are based on the SynREL optimized motors (A and B) presented in section 4.1.1. At first, the central part of the SynREL motors A

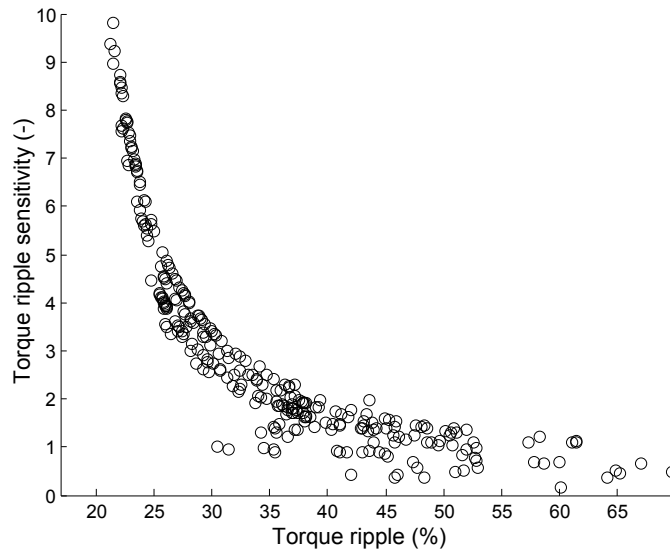


Figure 4.18: Torque ripple sensitivity versus the percentage torque ripple.

and B has been filled with ferrite PMs as shown in Fig. 4.1. The map of the torque ripple behavior has been carried out increasing the PM dimensions by steps.

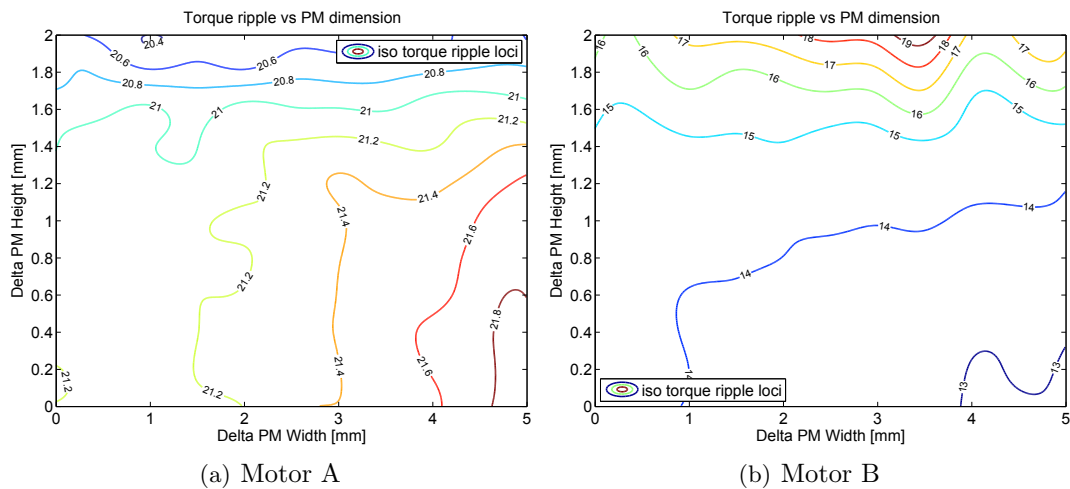


Figure 4.19: PM dimensions effect on torque ripple.

Fig. 4.5 and Fig. 4.5 show the contour plots of the torque ripple, considering a variation of the PM height (vertical axis) and width (horizontal axis) referring to motor A and B respectively. It can be noticed that small variations of the PMs dimensions have a negligible impact on torque ripple. On the contrary, depending on the machine size, the impact of an increment of the PM height is higher. Referring to motor B (smaller than A), increasing the PM height of 2 mm yields a torque ripple variation from 13 to 18% (see Fig. 4.5).

4.6 Conclusions

This chapter deals with the torque ripple reduction of SynREL and PMAREL machines. It is shown that torque ripple is strongly affected by stator and rotor geometry and by current phase and amplitude. Moreover, small geometry variations cause high torque ripple oscillations when "non-robust" solutions are adopted.

A detailed analysis of the design variables that have higher impact on the motor torque has been carried out showing their behavior for three different machines.

A novel method to evaluate the sensitivity of the torque ripple over all the design space has been presented, based on the analysis of the solutions resulting from the optimization process. The analysis highlights the difficulties found in the design, even when an optimization procedure is carried out. It also provides some suggestions to be adopted in designing SynREL or PMAREL motors, to achieve more robust solutions as far as the torque ripple sensitivity is concerned. The analysis carried out for three different motor sizes shown the main parameters that have to be taken into account when designing a SynREL motor.

The effect of the PMs on the torque ripple has been investigated, showing a slightly greater impact of the PM height and a dependence on the machine size. In particular, the PMs dimension effects on torque ripple are significant for small motors. The measures on a prototype are in good agreement with the results predicted by means of finite element analysis.

Chapter 5

Robust Optimization of a Traction PMASR Motor According to Given Driving Cycles

The progressive electrification of the private transport systems is becoming an established reality in the international scenario since it is seen as the most promising solution to reduce air pollution, oil dependency and to improve energy efficiency. As for convention internal combustion engine vehicles, the performance of an electric vehicle are strictly related to the driving conditions of the car in which the motor is installed. On the other hand, the optimization procedure of the electric motors does not consider in detail the actual working conditions. For this reason, when the machine works, it becomes mandatory to optimize the design in the most profitable areas in which the motor operates, in order to improve the overall performance. On this basis, some recent researches [47, 48, 49, 50] have introduced new design and optimization techniques for traction motors, in order to enhance the efficiency against a defined driving cycle. On the other hand, none of the previous researches have investigated neither the optimization of the torque ripple, nor the robustness of the solution, over the aforementioned driving cycle. In this chapter an optimization procedure of a Permanent Magnet Assisted Synchronous Reluctance (PMASR) motor for traction application is presented, considering a city and a highway driving schedule. The motor is equipped with a 36-slot 4-pole and an integral slot distributed winding. A high grade ferrite is considered. The interest in ferrite-based PMASR motors [18, 24, 51, 52] is spreading in the last years, as a consequence of the instability and the increase of the price of rare earth magnets. Moreover, it provides a high flux weakening operating range, which is usually an important requirement in traction applications. Conversely, the most important drawback is the intrinsically higher torque ripple [25] that can be reduced by means of different strategies, such as an optimization of the shape of the flux barriers and skewing [27, 53]. In this chapter a novel optimization strategy, that takes into account both high efficiency and low torque ripple performance, has been introduced analyzing the robustness of the solutions over the

whole driving cycle. Several parts of this project have been presented by the author in international conferences. In particular, in this Chapter, the work presented in [54] is widely described.

5.1 Evaluation of the motor requirements

5.1.1 Driving cycles

The motor performance have been assessed on the basis of two US driving cycles used to measure the fuel consumption and gas emission of light-duty vehicles.

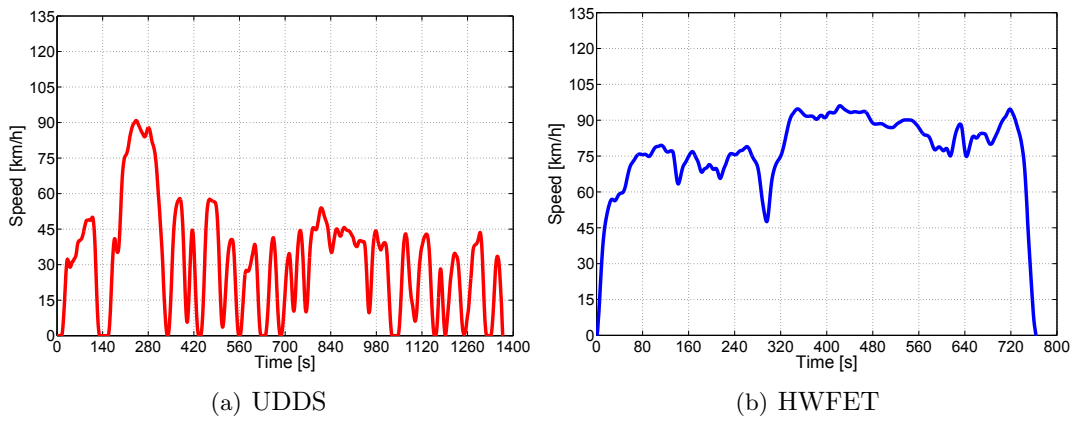


Figure 5.1: Driving cycle speed vs. time profiles.

The first, the Urban Dynamometer Driving Schedule (UDDS), reported in Fig. 5.1(a) is suitable for city driving. The cycle simulates an urban route of about 12km with frequent stops with a maximum speed of about 91km/h . It includes 23 stops over a period of 23min for an average speed of 32km/h . The second, the Highway Fuel Economy Driving Schedule (HWFET), is reported in Fig. 5.1(b). It represents the highway driving cycle. It is characterized by a no-stop operation over a route of 16km , with an average speed and a top speed of 77km/h and 97km/h , respectively [55].

5.1.2 Torque and power distributions

These driving cycles have to be performed by a medium size car with a mass of about $m = 1500\text{kg}$, equipped with two high speed PMASR motors. Each of them is connected to the respective wheel, with a diameter of $D_w = 500\text{mm}$, by means of a gearbox with a $1 : 8$ ratio. According to the method proposed in [56], the motor torque vs. speed distributions have been evaluated on the basis of the traction forces F_t computed, from the inertia force F , friction force F_f and drag force F_d , as reported in eqs. (5.1) - (5.4). The grading force has not been accounted since the route covered by the vehicle is flat.

$$F_t = F + F_f + F_d \quad (5.1)$$

$$F = m \cdot a \quad (5.2)$$

$$F_f = 0.01 \cdot \left(1 + \frac{v}{44.4}\right) \cdot m \cdot g \quad (5.3)$$

$$F_d = \frac{1}{2} \cdot c_x \cdot S \cdot v^2 \quad (5.4)$$

where v is the car speed, a is the car acceleration, g is the gravitational acceleration. The frontal area and the drag coefficient, have been estimated on the basis of the average values of a typical medium size car, which are $S = 1.85m^2$ and $c_x = 0.4$ respectively.

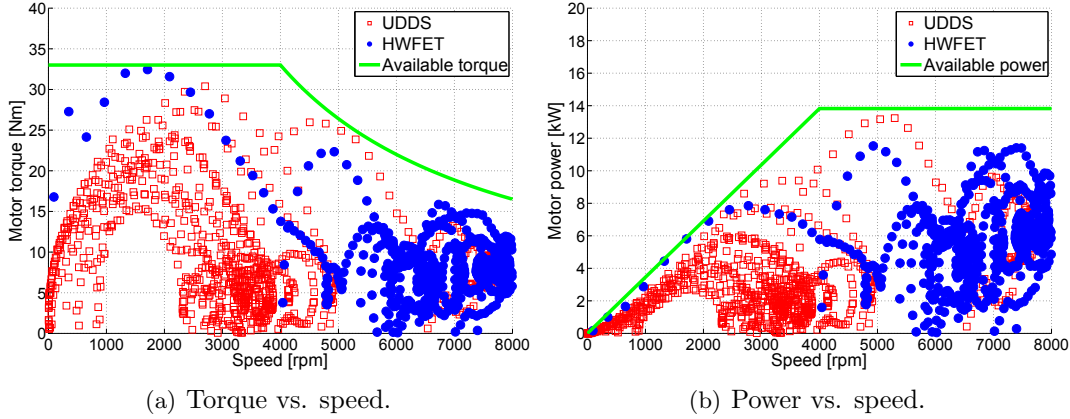


Figure 5.2: Electromechanical characteristics.

The torque and power vs. speed distributions, for both the driving cycles, are reported in Fig. 5.2. Since the optimization has been performed in the motor operation, the regenerative working area has been neglected in the present analysis.

The target available torque and power curve are highlighted, assuming a hyperbolic trend over the base speed such as to ensure an ideal constant power speed range. The motor has to develop a rated torque of about $33Nm$ up to the base speed of about $4000rpm$, with a maximum speed in the order of $8000rpm$.

It is worth noticing that, for both the driving cycles, the machine operates mainly at low torque. The RMS torque, that provides an assessment of the thermal state of the machine, is about $11Nm$ for the UDDS and $9Nm$ for the HWFET. It follows that, even if the motor has to be designed for the rated torque, the optimization have to be effectively addressed in low torque operation.

Two representative operating torque-speed points, the first for the city, the second for the highway driving, have been computed. These points, in which the machine works for most of the duration of the driving cycle, are $5Nm$ at $3500rpm$ for the UDDS and $7.5Nm$ at $7000rpm$ for the HWFET.

5.2 Design and optimization

A 36-slot 4-pole PMASR, integral slot distributed winding design, has been considered. The main motor dimensions comes on the basis of an existing prototype [57], reported in Fig. 5.3(a) and designed and optimized for an automotive application. The outer and airgap diameter are $200mm$ and $125mm$ respectively, while the airgap height is equal

Table 5.1: Representative operating points of the driving cycles.

Name	Symbol	UDDS	HWFET	Unit
Torque	T	5	7.5	Nm
Speed	n	3500	7000	rpm
Current density	J	2.2	3	A_{RMS}/mm^2
Current angle	α_{ie}	53	73	$^\circ$
Frequency	f	116	233	Hz

to $0.35mm$. The prototype has been manufactured and tested. As shown in [57], a good agreement between the experimental results and Finite Element Analysis (FEA) is achieved.

As reported in Table 5.1, the city and highway operating points, evaluated in 5.1.2, correspond to specific space current vectors and frequencies. As shown in Fig. 5.3(c) the city driving point is located along the maximum torque per ampere locus, while the HWFET is in Flux Weakening (FW) working point.

5.2.1 Pre-optimization analysis

On the basis of the aforementioned stator lamination and the requested motor specification, a new optimized design has been evaluated. The machine has been designed in order to meet the target torque and power profile ensuring a safe demagnetization at the operating temperature of $150^\circ C-180^\circ C$, working at the rated current density of $9A/mm^2$. The stack length and the number of conductors have been then adjusted in order to meet different rated torque specifications and providing a base speed around the target value of $4000rpm$. An optimization algorithm has been performed to the aim of minimizing torque ripple and losses. Furthermore, an evaluation and optimization of the robustness of the machine has been carried out. The robustness is a concept complementary to the sensitivity. A robust machine is defined as that design that has minimum sensitivity to the variations of the system parameters [58, 59, 40], that can be dimensional or operational (working conditions). This latter parameter topology is considered in the current analysis. In other words, the optimization has been set to minimize the torque ripple T_r and the losses P_l in both UDDS and HWFET operating points (7.1-5.8). Finally, as reported in (5.9) and (5.10), the requested design has to exhibit comparable performance as regards the torque ripple and losses for both operating conditions. Thus, their difference ΔT_r and ΔP_l , has to be minimized. The objective functions are defined as:

$$\min(T_{rUDDS}) \quad (5.5)$$

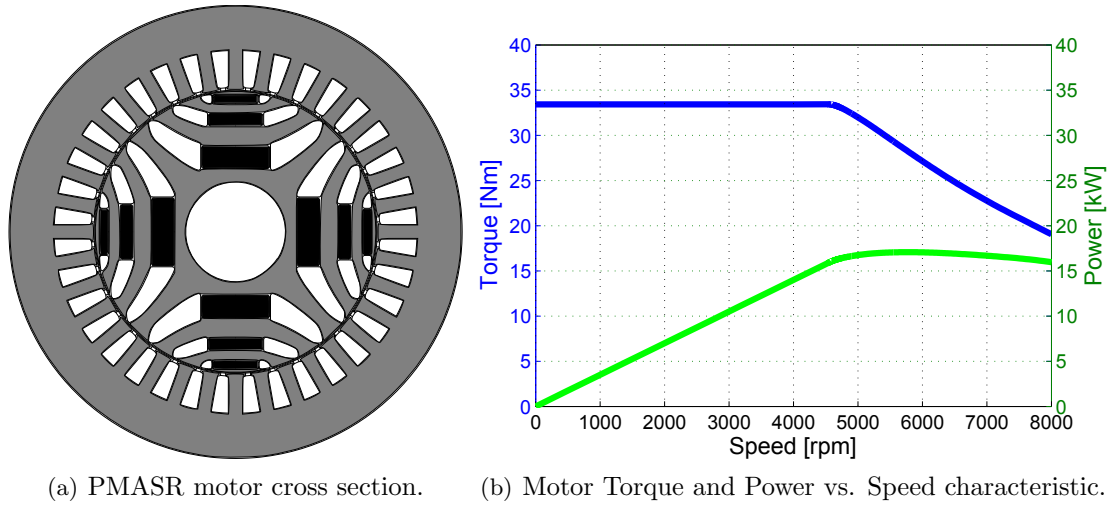
$$\min(T_{rHWFET}) \quad (5.6)$$

$$\min(P_{UDDS}) \quad (5.7)$$

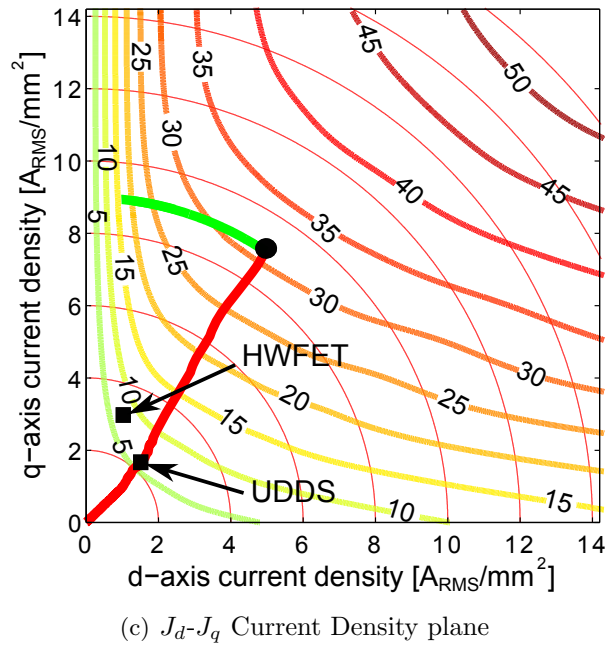
$$\min(P_{lHWFET}) \quad (5.8)$$

$$\min(P_{UDDS})\min(\Delta T_r) = \min|T_{rUDDS} - T_{rHWFET}| \quad (5.9)$$

$$\min(P_{lHWFET})\min(\Delta P_l) = \min|P_{UDDS} - P_{lHWFET}| \quad (5.10)$$



(a) PMASR motor cross section. (b) Motor Torque and Power vs. Speed characteristic.



(c) J_d - J_q Current Density plane

Figure 5.3: PMASR motor prototype.

Before selecting the optimization variables, it is important to consider their influence with respect to the objective functions just defined. The sketch in Fig. 5.4 shows the main geometrical parameters that have been considered for the current study of this PMASR motor.

The airgap, the inner and the outer stator diameter, D , D_r and D_e respectively, together with the electric loading have been kept as geometry constraints, thus ensuring a limited variation of the torque along the operation trajectory. It is well known that the motor performance are influenced by several parameters, since PMASR motors have intrinsically many degrees of freedom (especially the rotor geometry).

The torque ripple is determined by the interaction between the spatial harmonics of

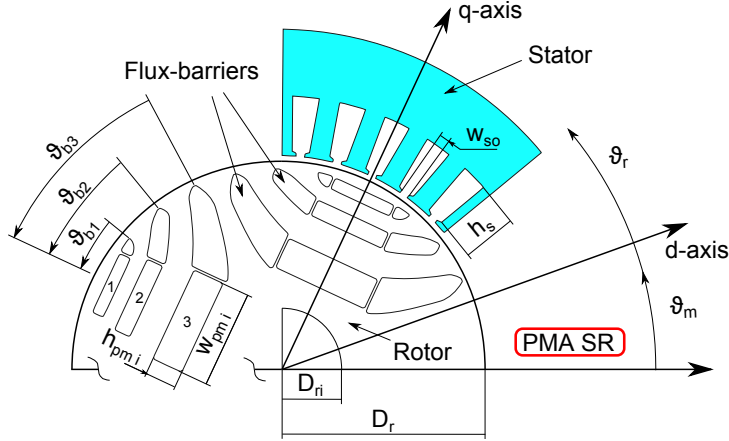


Figure 5.4: PMA SR geometrical variables.

magneto-motive force (MMF) due to the stator currents and the rotor geometry and it is one of the main drawbacks of these motors. In [40] it has been shown that the torque ripple is very sensitive to the geometry along the airgap region. For instance, there is a strong impact of the angles of the flux barrier ends (i.e. θ_{b1} , θ_{b2} , θ_{b3} assuming a three layer rotor).

Other influent parameters are the slot opening width w_{so} and the iron bridges height (also called iron ribs) h_{rib} . The first is suitable to be optimized, even if there is a minimum threshold to be considered, depending on the diameter of the elementary conductor that has to be placed into the stator slot. The second parameter has to be designed with respect to the mechanical stress due to the mechanical forces arising at high rotational speed.

Regarding the thickness of the flux barriers and the permanent magnet dimensions, some considerations can be done. The portion of air (or PMs) with respect to the iron along the q -axis, is known as insulation coefficient. This parameter is defined as follows: where h_{pmi} is PM thickness of the i -th flux barrier, D_r is the rotor diameter, D_{ri} is the shaft diameter. The choice of k_{air} is strongly related with two main design specifications. The first is the saturation level desired in the machine, which effects has been deeply investigated in [57]. The second is a high saliency ratio ξ , in order to guarantee a proper reluctance torque.

Conversely, PM dimensions have to be chosen taking into account the demagnetization, that can occur when the machine is working in deep flux weakening condition (high speed). Let us remember that the main role of the PMs in this type of motors is to saturate the iron bridges as well as enhance the power factor. For this reasons, in order to explore the effect of the most influent parameters of both rotor and stator of the PMA SR under study, the optimization variables have been selected as follows:

- the flux barriers end angles θ_{b1} , θ_{b2} , θ_{b3} ;
- the air coefficient k_{air} ;
- the slot opening w_{so} ;

Table 5.2: Input variables range properties.

Name	Symbol	Boundaries		Unit
		Lower	Upper	
Flux barrier angle 1	θ_{b1}	13	16	$^\circ$
Flux barrier angle 2	θ_{b2}	25	28	$^\circ$
Flux barrier angle 3	θ_{b3}	38	40	$^\circ$
Insulation coefficient	k_{air}	0.35	0.45	–
Slot opening	w_{so}	1	4	<i>mm</i>
Slot height	h_s	12	22	<i>mm</i>
Tooth width	w_t	4	8	<i>mm</i>

- the slot height h_s ;
- the tooth width w_t .

Table 5.2 reports the key parameters of the prototype, which have been considered in the optimization process, and the variable range between the lower and upper boundary.

5.2.2 Optimization procedure

Fig. 5.9 shows a scheme of the optimization steps.

The number of individuals N in the design of experiments table, are used as the initial population. The sequence of initial individuals has been determined using a pseudo random Sobol criteria. The Sobol method creates sequences of n -tuples that fill the n -dimensional design space more uniformly than a random sequence. The purpose of this work, apart from satisfying the objective function constraints, it is also to achieve an explorative optimization over all the parameters space. This allows to find out possible local minima. Thus, the experiments are uniformly distributed in the design space. Once the input motor variables are set, an automatic and parametric procedure has been design to build the geometry by FEMM. The FEA results are then post-processed in order to determine the torque ripple and the motor losses for both UDDS and HWFET working points.

The optimization algorithm MOGA-II has been chosen with the aim of achieving a fast Pareto convergence. It is based on Multi Objective Genetic Algorithm (MOGA) and works on a set of design configurations that are periodically updated when one generation is completed. The algorithm type is a generational evolution. MOGA-II is an efficient multi-objective genetic algorithm that uses a smart multi-search elitism. The concept of elitism enhances the convergence properties towards the true Pareto-optimal set. This operator is able to preserve some solutions without bringing premature convergence to local-optimal frontiers. These are the closest to the Pareto front and the ones that have the best dispersion. Elitism is introduced storing all non-dominated solutions discovered so far, beginning from the initial population.

The operators of crossover, mutation and selection have been set in order to provide robustness and efficiency to the optimizer. At each step of the reproduction process, one operator is chosen and applied to the current individual. A new set of variables, selected among the boundaries reported in Table 5.2, is then reassigned and the FEA is computed for the next generation.

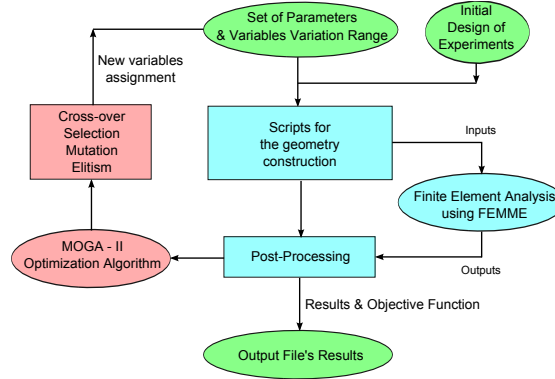


Figure 5.5: Optimization Process flow chart with MOGA-II.

5.2.3 Evaluation of the robustness

Let us define two homogeneous objective functions, y_1 and y_2 , as shown in Fig. 5.6. The robustness locus curve, representing the set of designs that exhibit the same value of the objective functions for a given point, can be described by the linear relationship $y_2 = y_1$. Considering the general solution (y_1^*, y_2^*) in the design space, a representative distance of this combination to the robustness curve can be evaluated along the straight line perpendicular to the above mentioned curve. As shown in (5.11), the coordinate of the intersection point $(\langle y^* \rangle, \langle y^* \rangle)$ is equal to the mean value of the two objective functions.

Every solution, that exhibits the same mean value, lies on the same straight line perpendicular to the robustness locus. The distance of the solution (y_1^*, y_2^*) to the intersection point $(\langle y^* \rangle, \langle y^* \rangle)$ is defined as,

$$d = \sqrt{(y_1^* - \langle y^* \rangle)^2 + (y_2^* - \langle y^* \rangle)^2} \quad (5.11)$$

As a consequence, among solutions that present the same mean value, i.e. lying on the same straight line perpendicular to the robustness locus, the most robust solution is the one showing the lowest distance d from the mean value.

5.2.4 Results

Fig. 5.7 reports, for each iteration, the value of the torque ripple and the losses corresponding to the UDDS and HWFET operating points. Since the optimization procedure is aimed to find a robust designs, the distribution of the points are concentrated around the robustness curves.

As shown in Fig. 5.7(a), the torque ripple distribution exhibits a high variation, in particular in the region above the robustness locus. The reason of this effect, is mainly due to the higher torque ripple in flux weakening operation [60], i.e. in the HWFET point. It is also worth noticing that the average distance, between the solutions and the robustness locus, is very high. This confirms that torque ripple is very sensitive to the geometrical parameters variation.

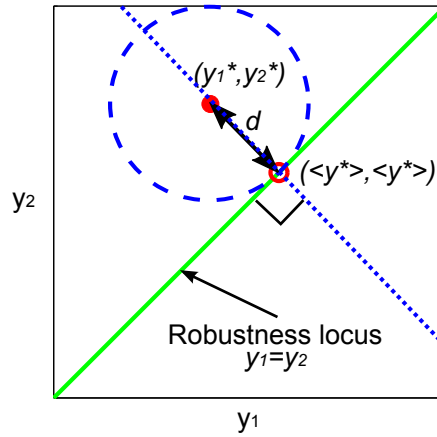


Figure 5.6: Concept of the robustness for a 2 - objective functions design space.

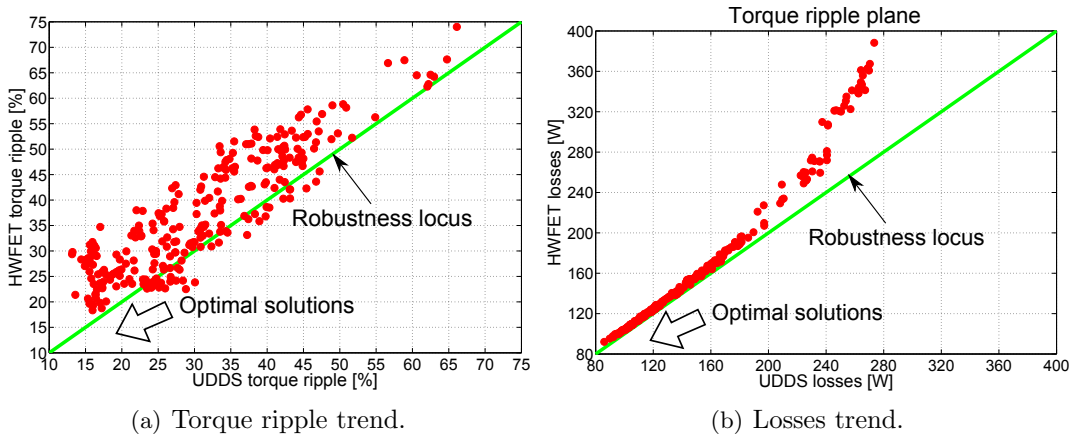


Figure 5.7: Torque ripple distribution in UDDS and HWFET cycle.

Similarly to the torque ripple, Fig. 5.7(b) reports the losses distribution. In this case the optimization results are more concentrated along the robustness locus. The solutions are shifted above for all cases due to the higher contribution of the iron losses in the high speed HWFET operating point with respect to the UDDS. Finally, the losses distribution diverges gradually from the robustness locus once the power loss exceeds 200W. For lower values, the distance d is very small, showing that losses are less sensitive to the geometrical variation within the range of variables.

Fig. 5.8 shows the trend of the distance of the solution with respect of the robustness locus vs. the mean torque ripple and the losses, evaluated in the UDDS and HWFET points, according to the concept introduced in Sec. 5.2.3.

In Fig. 5.8(a), the most representative robust designs for the torque ripple are highlighted with blue filled circles, between A and B . These points exhibit the highest robustness, since the distance d from the robustness locus is approximately zero, while the mean torque ripple, in UDDS-HWFET operation, increases from A to B . Always

referring to Fig. 5.8(a), the solution C is the one which exhibits a mean torque ripple lower than 20% and the lower distance d from the robustness curve. The corresponding losses are highlighted in Fig. 5.8(b). It is worth noticing that the robust designs for the torque ripple are not entirely the robust solutions under the losses point of view. For e.g. the solution A, that is robust in terms of torque ripple, shows a noticeable distance from the robustness losses curve, while the B exhibits good robustness for both torque ripple and losses.

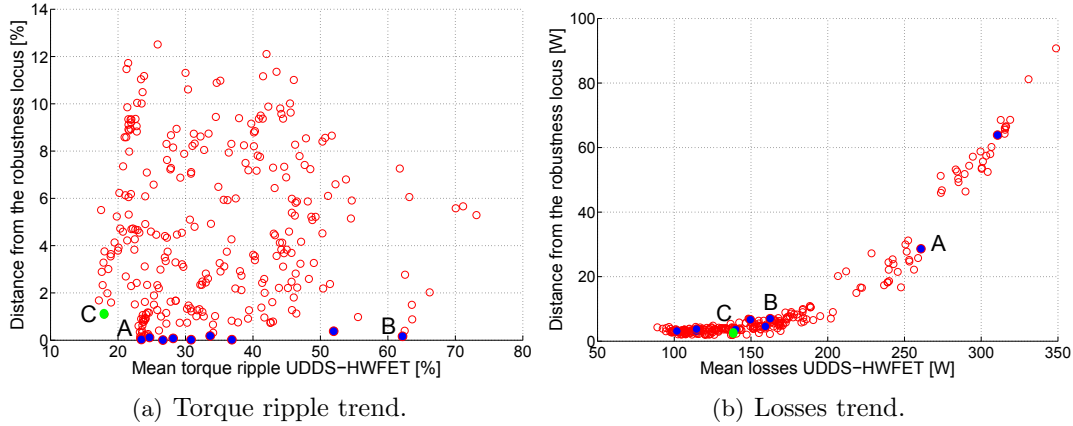


Figure 5.8: Distance of the solution from the robustness locus in UDDS and HWFET cycles.

In order to facilitate the optimal solution selection, Fig. 5.9 reports the mean torque and losses trend of the most robust solutions. This representation confirms that a solution with a robustness that satisfied one of the two objective functions does not necessarily satisfy the other. As usual, the selection of the best solution is a tradeoff between the results that better satisfy all the objective functions. In this case, considering these motor topologies and the application, the best compromise among the losses variation is resulting in design C , which is robust and presents the lower torque ripple and losses values for both the considered driving cycles.

5.3 Conclusions

In this chapter the optimization of a PMASR motor for traction has been investigated, considering the most profitable working area according to two different driving cycles, the first for the city driving USSD and the second for the highway driving HWFET. The electromechanical specification and the most profitable working areas have been predicted. The analysis of the geometrical parameters to be considered as optimization inputs has been done, and a proper variable range has been selected.

The design has been optimized by means of MOGA-II genetic algorithm aimed to the minimization of the torque ripple and the losses in the considered driving cycles. The difference between torque ripple and losses has been introduced as additional objective functions, in order to obtain comparable performance for the two representative working points. The robustness has been defined in order to find the best solution in the design space.

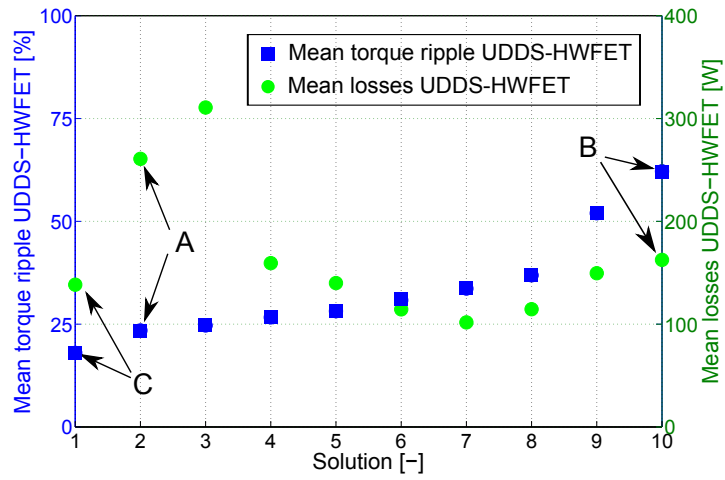


Figure 5.9: Mean torque ripple (blue squares) and losses (green points) trend of the most robust solutions.

The analysis of the optimized solutions emphasizes that a robust solution for the torque ripple could be not a robust solution with respect to the losses. The best candidate has been selected as a tradeoff between the lower torque ripple and the more robust results. This method is suitable for the analysis over a wider range of representative points where the motor normally operates during a driving cycle.

Chapter 6

PM Synchronous Machine Comparison for Light Electric Vehicles

The research of rare-earth free alternatives, such as ferrite, hot pressed NdFeB Permanent Magnet Assisted Synchronous Reluctance (PMASR) motor or pure reluctance motor, has potentially interesting implications especially in the perspective of industrial mass production. This work shows the comparison between a sintered NdFeB PMASR, ferrite PMASR, Synchronous Reluctance (REL) and a Surface mounted PM (SPM) machines with the same overall dimensions, winding arrangement and power supply size. The electromechanical performance have been evaluated and compared, in terms of torque and power. Finally, this research provides a description of the electric supply system in order to accurately and efficiently manage the motors for achieving the requested performance.

6.1 Introduction

The current trend in the research of high performance electric motor for traction application highlights the Permanent Magnet (PM) synchronous motor as one of the best candidate [61, 62, 63, 64, 32, 65, 66], due to the high torque density, high efficiency, high degree of freedom in the design of the motor [53]. On the other hand, the increase and the price instability of rare earth PMs, such as NdFeB and SmCo, is pushing heavily the research of rare earth free alternatives. The most interesting solution is represented by the synchronous Reluctance machines (REL).

They are suitable for traction application due to the robust structure, high operating speed range, high overload capability, no electro motive force, leading to a safe behavior in case of inverter failure.

Thanks to an appropriate vector control algorithm, the performance in terms of efficiency and torque become competitive [67]. Conversely, the drawbacks of reluctance machines are the intrinsically higher torque ripple[25] and low power factor. A reduction of the torque ripple can be achieved by means of a careful choice of the number

and the geometry of the rotor flux barriers, in addition to the skewing [27, 53] while an increase of the power factor is achievable by the insertion of PMs in the anisotropic rotor structure. This last configuration is known as Permanent Magnet Assisted Synchronous Reluctance (PMASR). It exhibits comparable performance to Surface mounted PM machines (SPM) needing a limited amount of expensive rare earth magnets. The same capability can be achieved filling the flux barrier with ferrite PMs, obtaining a low cost solution [18, 24].

Four different machine topologies have been considered and compared in terms of electromechanical performance and efficiency in the whole operating area. All the machines share the same stator geometry, overall dimensions and number of poles. The ferrite PMASR motor has been developed and optimized to maximize the torque density, minimize the torque ripple and PM volume and it has been considered as reference machine. All the machines are fed by the same power supply system, which rating represent a further constraint in this analysis. Finally, the efficiency of inverter coupled with the machines, has been investigated and some considerations are reported.

6.2 Machine Design and Optimization

A 36-slot stator lamination geometry is given as a constraint. The outer diameter D_e and the airgap diameter D are 276 mm and 180 mm, respectively. The airgap is fixed to $g = 0.7$ mm. The slot area is $S_s = 148$ mm², the fill factor is assumed to be $k_{fill} = 0.4$ while the peak current density has been fixed to $J_{MAX} = 13$ A_{RMS}/mm². The stack length is constrained to 40 mm. A M470–50 steel grade is considered for the lamination. Finally, a 300 V DC bus feeds the traction system.

The specifications, used for the motor design, are computed on the basis of the dynamic performance requested for a Light Electric Vehicle (LEV). This car, currently in development, is designed for a racing competition.

The main electromechanical requirements are summarized as follows:

- Peak torque, $T_{MAX} = 60$ Nm.
- Base speed, $n_B = 6000$ rpm.
- Maximum speed, $n_{MAX} = 12000$ rpm.
- Flux weakening range, 1 : 2 [29].

With the aim of reducing the maximum supply frequency and thus the iron losses, the number of poles has been selected to $2 \cdot p = 4$. On the other hand, unlike PMASR machines with a high number of pole, designs with lower number of poles exhibit a higher anisotropy [68]. An integral slot distributed winding has been considered. This winding arrangement proves to be the most effective solution when a high anisotropic rotor is adopted. A high saliency ratio is expected especially if compared to a Fractional Slot Concentrated Winding (FSCW) solution [33, 32].

The motor topologies, considered in this analysis, are shown in Fig. 6.1. The PMASR motors of Figs. 6.1(a) and 6.1(b) are characterized by a symmetrical rotor with three flux barriers per pole. The PMASR-A is filled with ferrite (remanence flux density

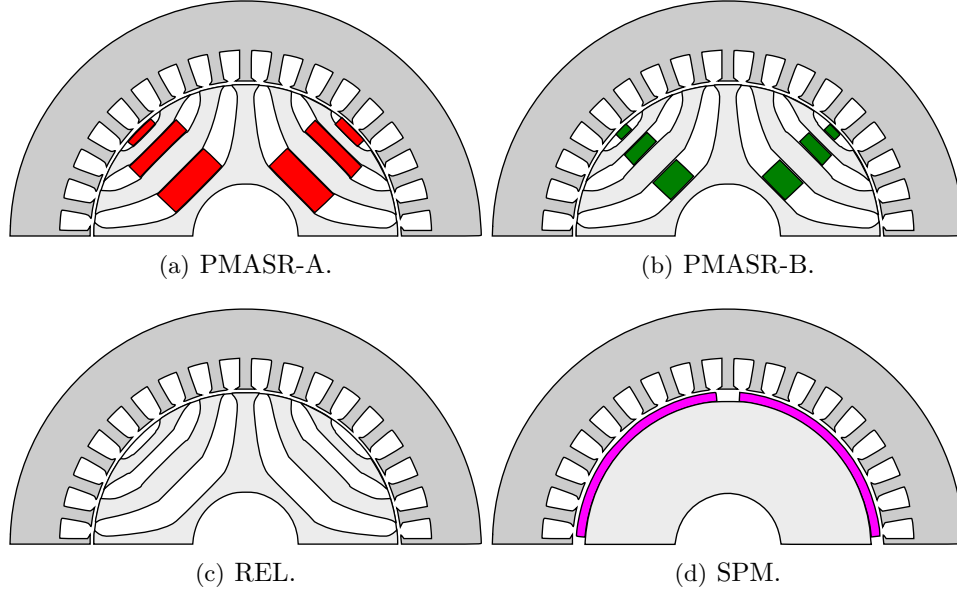


Figure 6.1: Motor sketches.

0.4 T @ 20 °C, knee flux density 0.1 T @ −40 °C, recoil permeability 1.05, density 4800 kg/m³). In PMASR-B a more valuable NdFeB PM has been used (remanence flux density 1.1 T @ 20 °C, knee flux density 0.1 T @ 140 °C, recoil permeability 1.05, density 7500 kg/m³). PMASR-A has been considered as reference machine. The torque ripple, the torque density and the PM volume, have been optimized under peak load condition by means of a multiobjective non-dominated sorted genetic algorithm. The stator geometry has been fixed during the optimization procedure and the optimization variables are the flux barrier angles and the insulation ratio [69], defined as follows,

$$k_{air} = \frac{2 \cdot \sum_i t_{bi}}{D_r - D_{sh}} \quad (6.1)$$

where t_{bi} is the thickness i -th of the flux barrier, D_r is the rotor diameter and D_{sh} is the shaft diameter.

Moreover, for each iteration, the PM demagnetization levels at the peak current density have been verified in order to provide effective solutions. A motor design is accepted when the minimum flux density in the PM is higher than the flux density at the knee of the BH curve (the demagnetization test temperature is considered, −40°C).

Finally, an optimal solution has been selected. It shows a peak torque of 60 Nm with a torque ripple of 14 %. The number of conductors per each slot, series configuration, n_{cs} , has been changed in order to adjust the base speed close to the requested target of 6000 rpm.

On the basis of the PMASR-A rotor lamination, a PMASR-B and a REL topology, shown in Figs. 6.1(b) and 6.1(c), have been introduced. Finally, a SPM machine, reported in Fig. 6.1(d), has been designed. It is equipped with a rotor characterized by 4 C-shape NdFeB PMs. It is important to highlight that the minimum PM thickness

has been evaluated in order to ensure a safe demagnetization under deep flux weakening operation.

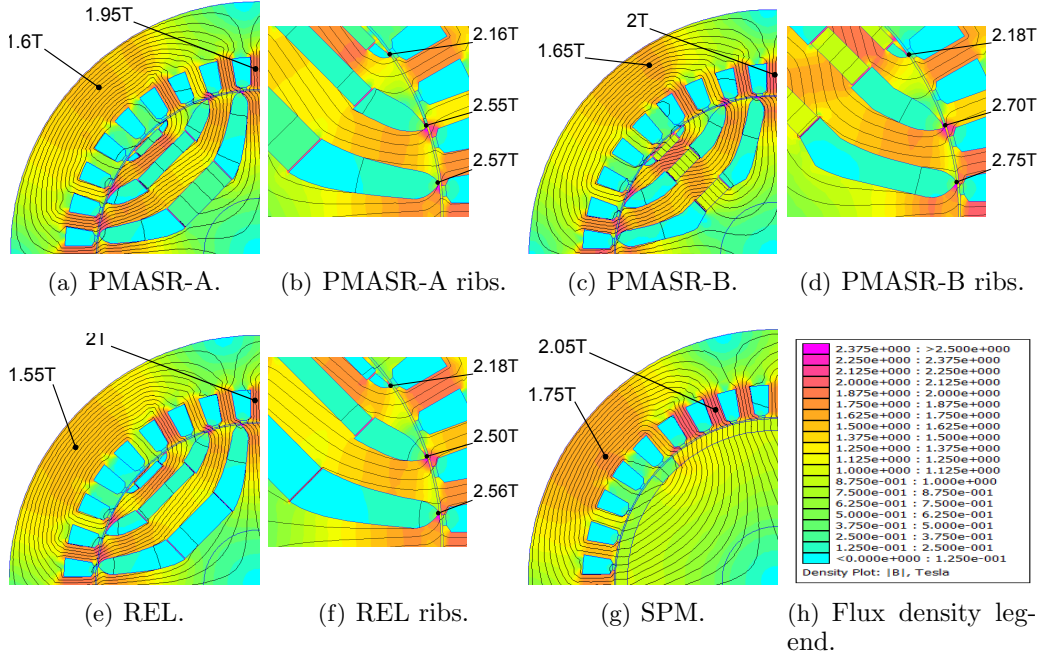


Figure 6.2: Flux density maps at peak load operation.

In order to provide a meaningful comparison, PMASR-B, REL and SPM are characterized by the same number of conductors of PMASR-A. Therefore, they exhibit equal peak current and VA-rating, thus leading to employ the same inverter.

Since the machines are designed in overload operation, a proper cooling system is mandatory. Even if it increases the complexity of the traction system, it yields to reduce the machine mass, improving the car dynamic performance. Conversely to NdFeB, the ferrite has got a positive reversible temperature coefficient of coercivity. This increases the demagnetization strength as the temperature increases, leading to an improvement of the motor performance.

6.3 Comparison of the topologies

The electromechanical performance of the machines have been evaluated on the basis of the synchronous space vector control in the d/q reference frame. The machine is controlled in order to exhibit a constant torque up to the base speed, working along the Maximum Torque per Ampere (MTPA) locus. For speeds higher than the base one, the motor is operated in FW, along the current limit and the Maximum Torque Per Voltage (MPTV) locus, if included [70, 60, 34].

An overload analysis has been performed in order to evaluate the flux density levels at the peak load. The flux density maps are shown in Fig. 6.2.

PMASR-A and PMASR-B motor, in Figs. 6.2(b) and 6.2(d) respectively, show local saturation, especially in the areas corresponding to the stator teeth and the rotor iron ribs,

Table 6.1: Key machine parameters summary

Design	PMASR-A	PMASR-B	REL	SPM	Unit
T_{MAX}	60	61	53	72	Nm
n_B	5738	5981	5853	5632	rpm
n_{MAX}	> 12000	> 12000	> 12000	10626	rpm
I_{MAX}	129	129	129	129	A_{RMS}
PF_B	0.80	0.84	0.72	0.96	—
γ_B	61	60	64	9	$^\circ$
Λ_{PM}	16.3	29.5	0	138	mWb_{peak}
L_{dB}	0.233	0.230	0.239	0.207	mH
L_{qB}	1.52	1.42	1.64	0.325	mH
ξ_B	6.6	6.2	6.9	1.5	—
I_{ch}	42	76	0	263	A_{RMS}
P_{CuB}	2530	2530	2530	2530	W
P_{FeB}	654	697	625	662	W
η_{eB}	91.8	92.1	91.2	93.0	%
n_{cs}	6	6	6	6	—
G_{Cu}	5.8	5.8	5.8	5.8	kg
G_{PM}	0.71	0.45	0	1.1	kg
G_{Fes}	9.0	9.0	9.0	9.0	kg
G_{Fer}	5	5.5	5	6.8	kg
G_{Fe}	14	14.5	14	15.8	kg
G	20.5	20.75	19.8	22.7	kg
$Cost$	1	1.39	0.93	2.08	$p.u.$

as expected at peak load condition. As regards the REL machine, reported in Fig. 6.2(f), the saturation is lower due the absence of PMs in the rotor structure. Conversely, the stator saturation for the SPM motor is higher, due to the higher flux contribution of the PMs which are placed on the rotor surface.

Table 6.1 summarizes the main electromechanical results, masses and cost indexes. They are represented by the peak torque T_{MAX} , the peak current I_{MAX} , the base speed n_B , the maximum speed n_{MAX} , the Power Factor PF_B , the commutation angle γ_B , the PM flux linkage Λ_{PM} , the d -axis synchronous inductance L_{dB} , the q -axis synchronous inductance L_{qB} , the saliency ratio ξ_B and the characteristic current I_{ch} . As regards the losses, the copper losses P_{CuB} , the iron losses P_{FeB} and the electrical efficiency η_B are reported. The subscript B highlights that the quantity has been evaluated at the base point, along the MTPA locus. Finally the mass quantities have been computed as well, including the copper G_{Cu} , PMs G_{PM} , stator iron G_{Fes} , rotor iron G_{Fer} , total iron G_{Fe} and total G .

Let us consider PMASR-A motor as reference machine for the following comparisons. Even if the volume of NdFeB PMs used in the PMASR-B motor is about 40 % lower, the PM flux linkage is almost doubled. The SPM motor instead, which exhibit a volume of rare earth PMs 60 % higher, shows a PM flux linkage about 4.5 times higher.

6.3.1 Constant torque capability

As regards the operation in the constant torque region, PMASR-B and SPM motors exhibit respectively a peak torque of 1 % and 20 % higher than that of PMASR-A. Conversely, the REL motor torque is almost 12 % lower. It is well known that the PMs, assisting a reluctance machine, are using part of their flux to saturate the internal iron bridges and the iron ribs located on the rotor periphery, which are necessary for mechan-

ical reasons. For this reason, REL machines require a higher current in order to provide the same saturation effect ensured by the PMs in the PMASR motors. For the REL motor under study, to reach the peak torque specification of 60 Nm the corresponding current has to be increased up to around $142 A_{RMS}$.

Concerning the anisotropy of the reluctance machines, the results show comparable saliency ratio, in the range $6 - 7$. The highest is achieved by the REL machines, while the lowest is exhibited by the PMASR-B. An analysis of the ratio between the d/q -axis synchronous inductances of PMASR-B shows that the L_{dB} is the lowest among the designs due to the higher rib saturation. On the other hand, the L_{qB} is reduced as well due to the higher saturation of the iron paths between flux barriers, as shown in Figs. 6.2(c) and 6.2(d). It is worth noticing that the SPM machine provides a limited anisotropy, with a saliency ratio in the order of 1.5.

6.3.2 Flux weakening capability

Torque, power and PF trends are reported in Fig. 6.3.

Analysis shows that a characteristic current (given by the ratio between PM flux linkage and d -axis inductance) close to the peak current I_{MAX} , ensures an excellent Constant Power Speed Range (CPSR) capability [34]. Although this condition is not achieved for all the considered motors, as shown in Table 6.1, due to the limited requested Flux Weakening (FW) ratio ($2 : 1$), the performance over the base speed are well suited for the PMASR-A and PMASR-B machines.

The higher value of the characteristic current I_{ch} of PMASR-B motor produces a slightly better CPSR and power factor with respect to the PMASR-A, as shown in Figs. 6.3(b) and 6.3(c), respectively. These results confirm the wide speed range capability of synchronous reluctance machines. The PMASR and REL machines outmatch the maximum speed target of 12000 rpm . Since the characteristic current is lower than the rated one [34], the current space vector is controlled in order to work along the MTPV locus machine in deep FW operation, and the maximum speed is only limited by the mechanical strength of the rotor and bearing design.

Despite the SPM motor exhibits a higher overload torque, in the FW region the torque and power characteristics decrease down quickly to 0 up to a maximum speed $n_{MAX} = 10500 \text{ rpm}$. In fact, the characteristic current of the SPM machine is higher than the peak current, yielding to a torque vs. speed characteristic not suitable for traction application. It is worth noticing that the combination of the SPM with a FSCW is able to provide an optimal FW performance [71].

In order to provide a torque profile which encloses the PMASR motors torque vs. speed curve, the base speed has to be increased to 8900 rpm , reducing the number of conductors per each slot, series configuration n_{cs} down to 4. On the other hand, this measure requires an oversizing of the supply converter. An improvement of the constant torque region is achievable by means of a reduction of the PM flux linkage, i.e. the peak torque, reducing the machine stack length of about 17 %. The base speed and the maximum speed are expected to increase of about 20 %, up to 7200 rpm and 11700 rpm respectively and the same inverter size can be used.

Regarding the PF trends, shown in Fig. 6.3(c), SPM machines provides the highest value in the constant torque region, in the order of 0.95 up to 6000 rpm . Similarly to

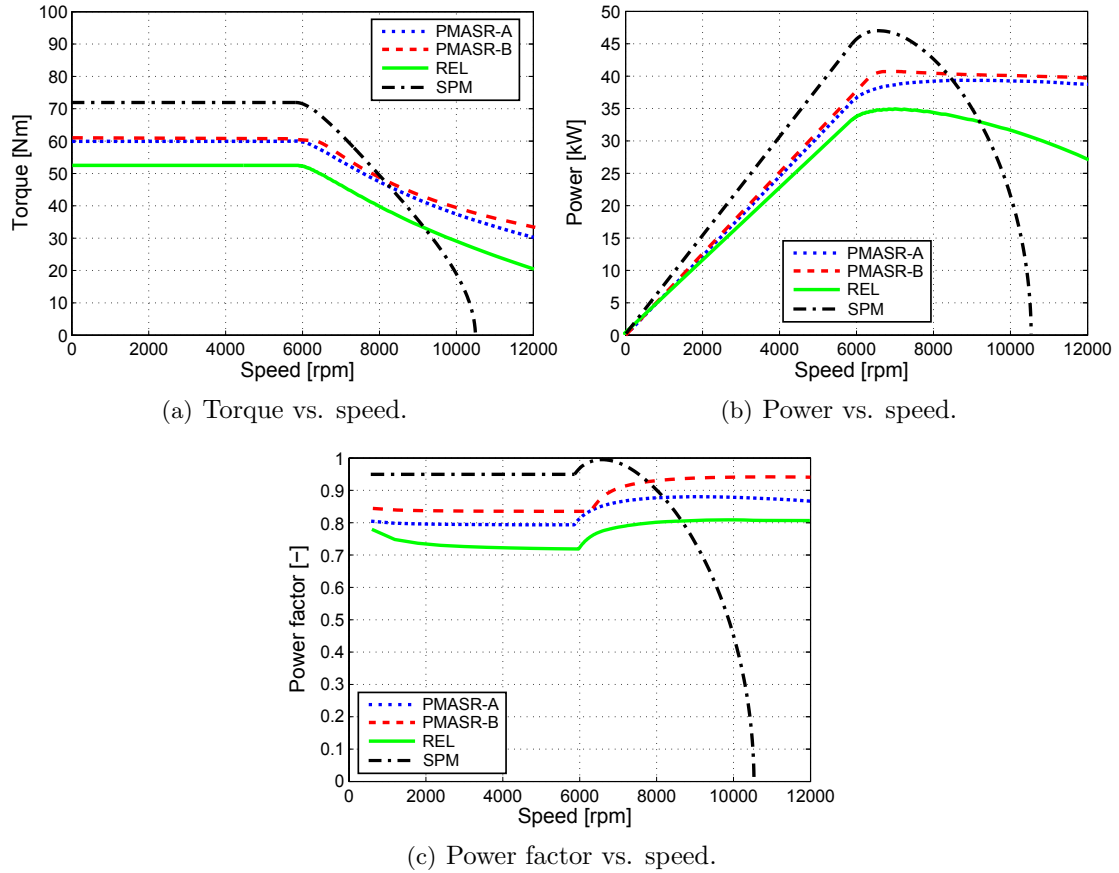


Figure 6.3: Electromechanical performance.

the power trend, the PF falls quickly as the speed increases.

The performance of the REL motor in terms of torque power and PF, are lower than the other motor topologies. The SPM machine, although provides the highest torque density, it is not suitable for the applications considered in this research, which require a wider speed range. However, its behavior in FW operation might be suitable for those application which require a less extended speed range, such as electric vehicle for urban mobility [50].

6.3.3 Losses and efficiency

The computation of the losses and electrical efficiency has been performed, according to the vector control strategy in the $I_d - I_q$ plane, mentioned in Sec. II. The Bertotti's equation is used for the evaluation of the iron losses, on the basis of the hysteresis and eddy current coefficients extracted from the losses curve data available for the lamination.

As reported in Table 6.1, a comparison of the losses at the base point, show similar results among the machines. On the other hand, since the study has been performed at the same overload current and not at the same torque, an analysis of the losses and the

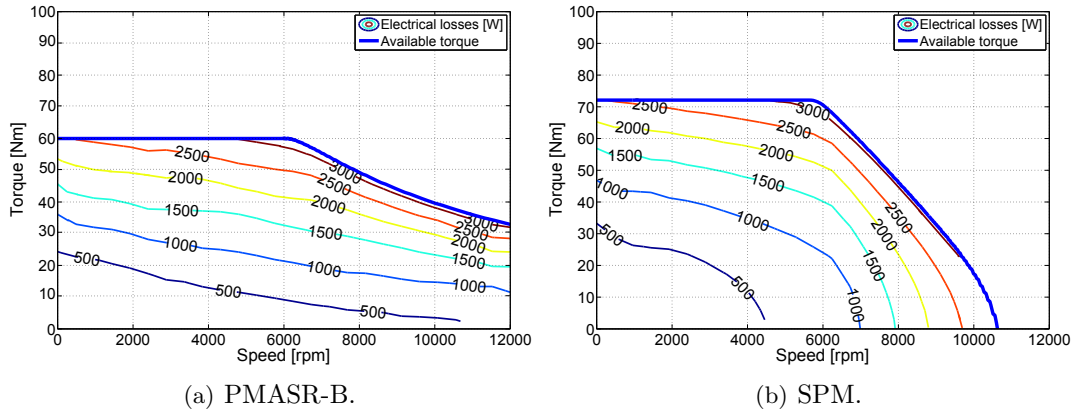


Figure 6.4: Constant electrical losses loci in the torque-speed plane.

efficiency in the whole operating area is more meaningful.

Fig. 6.4 reports the trend of the losses in the torque vs. speed plane for PMASR-B and SPM machine. It is worth noticing that in both cases the losses profile tends to follow the trend of the torque.

Fig. 6.5 shows the comparison of the machines electrical efficiency maps in the torque vs. speed plane. The available overload torque profile is highlighted. The highest electrical efficiency, in the order of 94 %, is provided by the PMASR-B and SPM. Comparing to the PMASR-B, the PMASR-A and REL motors show a lower efficiency due to the worser FW capability.

On the other hand, the distribution of efficiency is different between the reluctance and SPM machines. The SPM machine exhibits an higher efficiency operation in medium speed range, around the base speed. Due to the remarkable reduction of the torque as the speed increases over the base one, the efficiency falls quickly in FW operation.

6.3.4 Economical comparison

As regards the masses, the lowest values are achieved by the REL and PMASR-A motor, due to the absence and lower mass density of the ferrite PMs in comparison to that of NdFeB, respectively. Contrarily to PMASR machines, the rotor mass of SPM motors can be further reduced introducing flux barriers in proximity of the rotor shaft, without affecting the motor performance.

Finally, the total machine costs are evaluated in p.u., considering the average cost of the iron lamination and PMs as for 2014. It is worth noticing that the noticeable increase of about 40 % of the PMASR-B machine cost due to the more valuable NdFeB PM, leads to a negligible increase of the performance in terms of peak torque and PF. While the REL motor exhibit the lowest total cost, about 7 % lower than that of PMASR-A, the SPM solution shows a doubling of the cost.

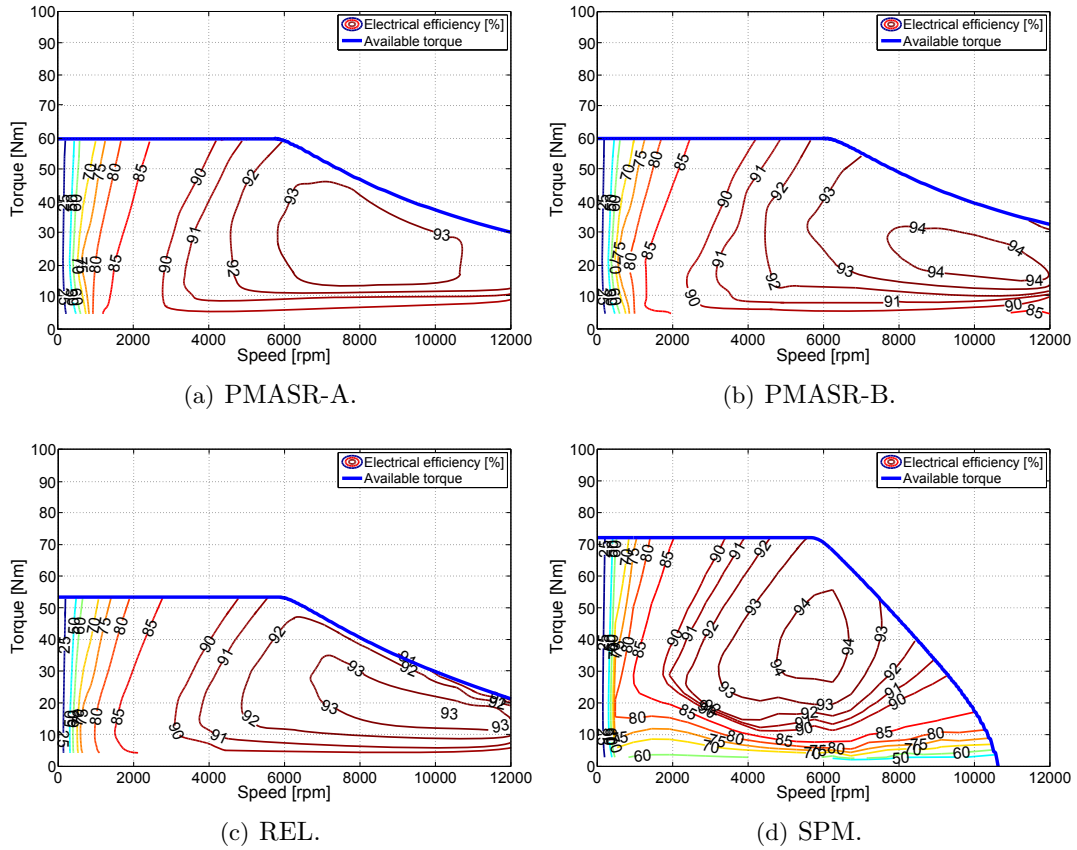


Figure 6.5: Constant electrical efficiency loci in the torque-speed plane.

6.3.5 Overview of the electric supply system

In LEVs mass represents a critical aspect. For this reason, the car power-train architecture considered in this work is quite simple. It is composed by synchronous electric machine (EM) direct connects at the rear wheels by a fixed gearbox, a bi-directional single-stage power converter and an battery packs. Fig. 6.6 reports a block scheme of the considered system architecture.

The power converter, that has been considered for this LEV, is a simple but effective half bridge three-phase inverter. Its DC bus is direct connected to the vehicle energy storage whose voltage, V_{DC} , is fixed to 300 V. The power converter features are summarized in Table 6.2.

As reported in Fig. 6.7, the power converter efficiency maps has been studied for the considered motor topologies, highlighting the overload torque profile. Fig. 6.7 shows that the highest efficiency, about 96%, is provided by all electric machines. As already reported in Fig. 6.7(d), the SPM machine exhibits an higher efficiency around the base speed and medium speed range. Moreover, in FW region the efficiency falls quickly as the speed increases principally due to the high reduction of the torque. Conversely to the PMASR-A, the PMASR-B and REL motors show a higher efficiency in the FW operation.

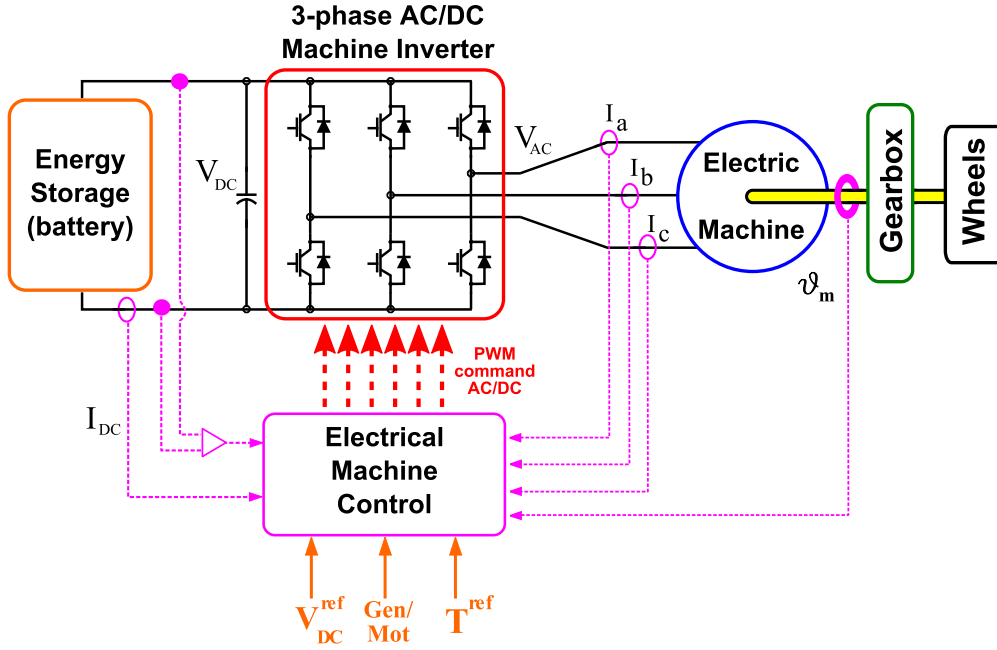


Figure 6.6: LEV power-train sketch overview.

Table 6.2: Three-phase inverter parameters.

Parameter	Value
Number of Phases	3
Type of switch	IGBT
Maximum DC bus voltage	300 V
Rated AC current	200 A_{RMS}
Rated AC voltage	120 V_{RMS}
Type of switch modulation	SVM
Switching frequency	20 kHz
Dead time	2 μs

These losses analysis has been carried out in order to estimate the inverter efficiency in the different EMs working points. The principle reasons of the losses in a power converter are the conduction losses and switching losses in its devices, [36]. The switching losses, p_{sw} , and conduction losses p_{cond} with IGBT devices have been calculated by following formulae, [?, 37]:

$$p_{sw} = (E_{ON} + E_{OFF}) \cdot f_{sw} \quad (6.2)$$

$$p_{cond} = v_D \cdot i_D \quad (6.3)$$

where v_D and i_D are the device voltage and the current, respectively. E_{ON} the turn-on switching energy, E_{OFF} turn-off switching energy and f_{sw} is the switching frequency. As reported in the device characteristics, these energies are roughly proportional to device current and as example are $E_{ON} = 16 \text{ mJ} @ 150 \text{ A}_{RMS}$ and $E_{OFF} = 8000 \text{ mJ} @ 30 \text{ A}_{RMS}$.

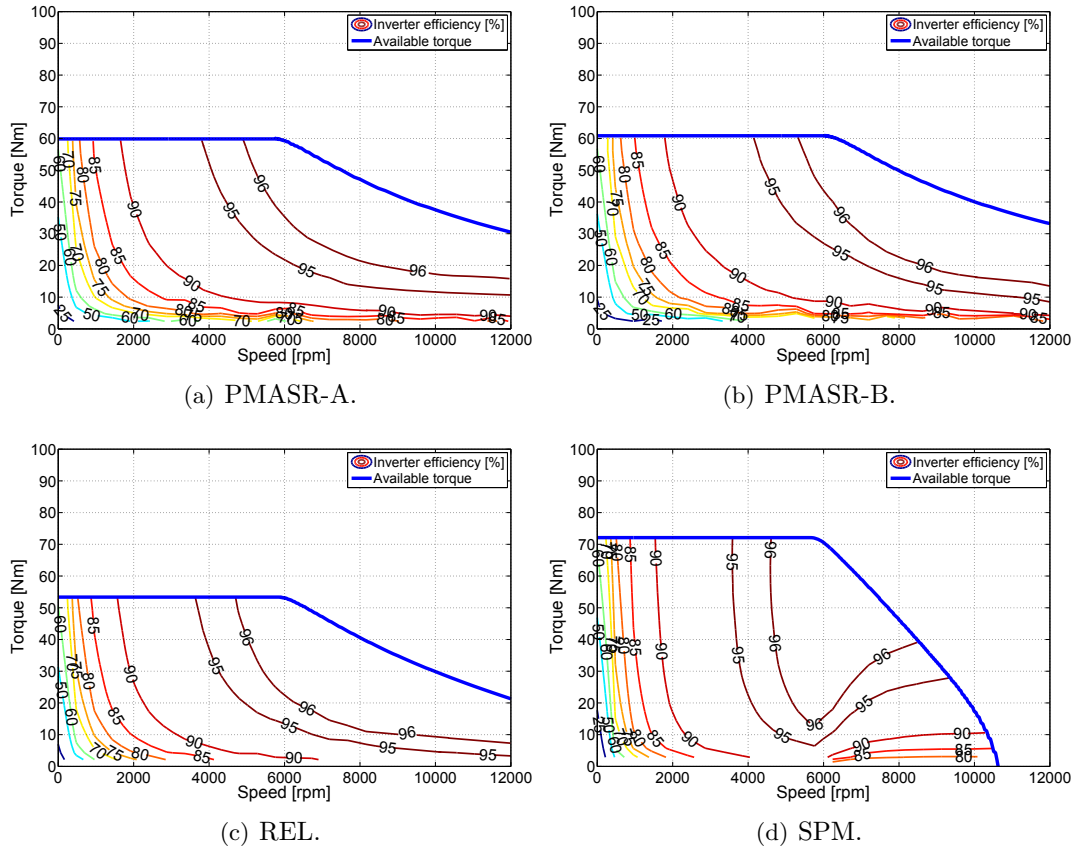


Figure 6.7: Constant inverter efficiency loci in the torque-speed plane.

6.4 Conclusions

This research confirms the feasibility of the realization of an high performance ferrite PMASR for traction applications. The motor capabilities have been computed on the basis of the dynamic performance requested for a LEV. A ferrite PMASR machine has been designed and optimized with the aim of minimizing the torque ripple, PM volume and maximizing the torque density. On the basis of the same stator laminations, winding arrangement and number of poles, four different machine have been analyzed and compared. The results highlight that the proposed PMASR motor exhibits an optimal torque vs. speed behavior for the application.

Even if the proposed SPM machine shows the highest torque density, due to the limited FW area, the electromechanical performance over the base speed are not suitable. In order to satisfy the torque requirements at high operating speed, a reduction of the number of conductors proves to be necessary. This is an important drawback because it yields an increase of the phase current and an oversizing of the power supply system. For these reasons, this research emphasizes that the proposed PMASR machine is an excellent solution. It combines high efficiency in a wide speed range with a cost reduction due the adoption of ferrite PMs or with a small volume of rare-earth PMs. Moreover,

this research shows that the adoption of the NdFeB in PMASR design, does not provide significant advantages requiring a complete redesign of the rotor geometry.

Chapter 7

Synchronous Reluctance and PM Assisted Reluctance Motors for Washing Machines Application

In order to limit the continuous increase of electrical energy demand and consequently to reduce the environment pollution and the greenhouse effect, it has become mandatory to improve the efficiency of electric motors used in many application fields. Nowadays, high-efficiency motors can lead to significant reductions in energy consumption and also reduce the environmental impact. Sustainable use and investment also demands increased motor reliability. Major energy savings are also gained through the use of variable-speed drives (VSDs). Today, in some European Union (EU) countries, this technology is adopted in as much as 30 – 40% of all newly installed motors. This chapter deals with the design and optimization of a Synchronous Reluctance and a Permanent Magnet Assisted Reluctance Motors for washing machines application which, as highlighted in the previous chapters, are one of the best available emerging electric motor technologies. The main purpose of this work is to investigate on the feasibility of SynRel/PMA SynRel motors and how these could suit the application as a valid alternative to commercial motors used so far.

7.1 Introduction

Premium/IE3¹ efficiency class motors are now mandatory in North America and other countries. Super-Premium/IE4 and Ultra-premium/IE5 efficiency classes are to be defined in the 2nd Edition² of the IEC³ 60034-30 standard. For line-start fixed-speed applications, Super-Premium/IE4-class line-start permanent magnet (PM) motors and squirrel-cage induction motors are recent entrances in the industrial motor market. For

¹The designation of the energy-efficiency class in the IEC 60034-30 Standard consists of the letters 'IE' (International Energy-Efficiency), directly followed by a numeral representing the classification.

²The 2nd Edition will be denoted as IEC 60034-30-1 for line-start motors and IEC 60034-30-2 for VSD-fed motors.

³IEC - International Electrotechnical Committee.

variable-speed applications, IE4-class synchronous reluctance motors are also a recent entrance in the market.

An important measure for wide market acceptance of high efficiency motors is the availability of harmonized standards, dealing with motor performance testing, efficiency classification, and display of ratings [72]. This also applies to VSDs. In the United States, Premium/IE3 motors have been mandatory since 2011. In China and EU countries, High-Efficiency/IE2 motors have been mandatory since 2011, and Premium/IE3 motors will be mandatory in 2015 in EU countries [73].

So far, household appliances, such as washing machines, dishwashers, dryers and vacuum cleaners, have been mainly powered by universal motors [74]. The pie chart shown in Fig. 7.1 reports the main electric motors used in Europe Middle East and Africa (EMEA) for washing machine applications:

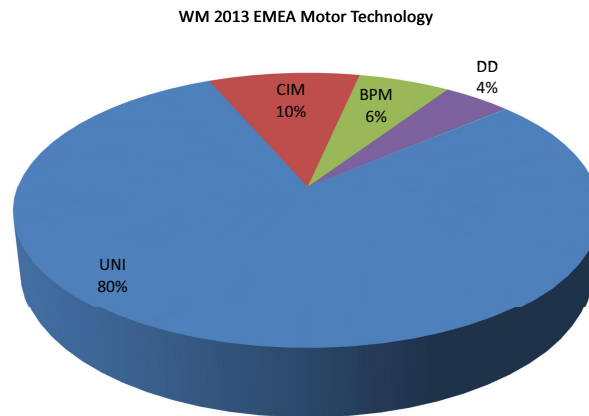


Figure 7.1: Washing Machine Motor Technology.

highlighting the utilization of Universal Motors (*UM*), Cage Induction Machines (*CIM*), Brushless Permanent Magnet (*BPM*) and Direct Drive (*DD*) machines.

It is worth noticing how Universal Motors are still widely used covering the 80% of the worldwide market. Although during the last ten years many other types of electric motors have been considered as alternatives, universal motors are still surviving thanks to such advantages as high power versus size ratio, high speed range, simplicity of regulation and low cost of the simple drive [75].

On the other side, they suffer from low efficiency values compared to other kinds of motors and from reliability issues due to the presence of commutator and brushes [75]. Moreover UMs generates a lot of radio interference due to the current switching in the commutator.

According to the aforementioned consideration it is clear that in the next few years, also low power household appliances will have to satisfy the high efficiency requirements. This will lead to a large scale change in the motor topologies applied for washing machines applications as well.

In Fig. 7.2, the IE1, IE2, IE3, IE4, and IE5 classes of the revised IEC 60034-

30 standard are shown for four-pole 50/60 Hz motors⁴. The motor nominal efficiency should be determined according to IEC 60034-2-1⁵.

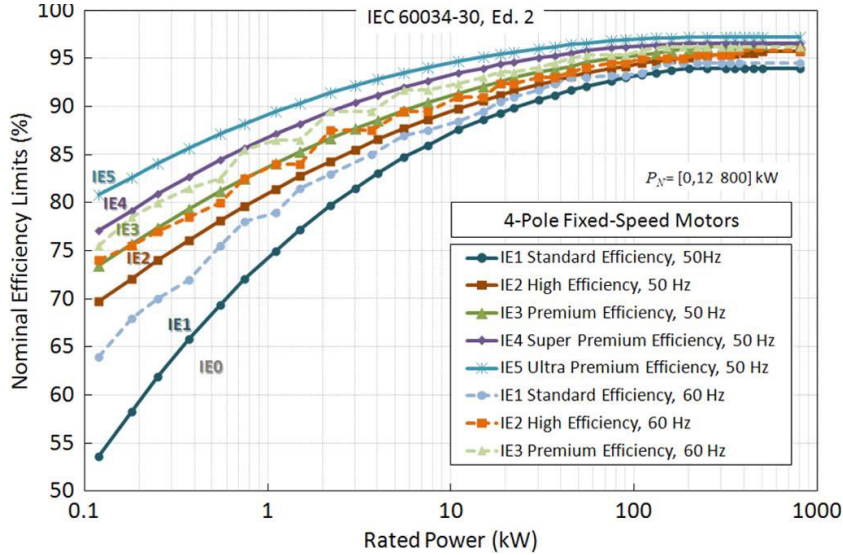


Figure 7.2: Planned revision (second edition)

7.2 Machine Design and Optimization

7.2.1 Electric motor requirements

Electric motors for washing machines are working in a very wide operation speed range, usually up to 18000 *rpm* depending on the coupling ratio between the drive motor to the wash basket (normally connected through a transmission belt).

The specifications, used for the motor design, are determined on the basis of the torque and power characteristics required for this application represented in Fig. 7.3.

The main electromechanical requirements are summarized as follows:

- Rated torque, $T_n = 1 - 1.5 Nm$.
- Base speed, $n_B = 5000 - 6000 rpm$.
- Maximum speed (spinning condition), $n_{MAX} = 16000 - 18000 rpm$.
- Maximum Final Torque, $T_{max} @ n_{MAX} = 0.4 - 0.5 Nm$.
- Power, $P @ n_{MAX} = 700 - 800 W$.
- Flux weakening range, 1 : 3.

⁴Rotating electrical machines-Part 30: Efficiency classes of single-speed, three-phase, cage-induction motors (IE-code), IEC60034 - 30, 1st Ed., 2008.

⁵Rotating Electrical Machines-Part 2-1: Standard Method for Determining Losses and Efficiency From Tests (Excluding Machines for Traction Vehicles), IEC60034-2-1, 1st Ed., 2007.

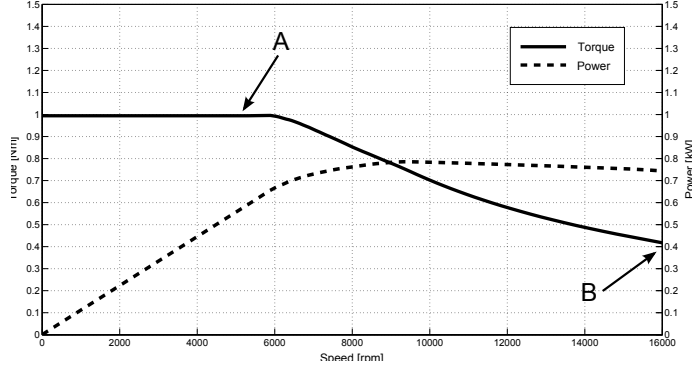


Figure 7.3: SynRel motor torque and power performance

The outer diameter D_e is given as a constraint ($< 110 \text{ mm}$) in order to keep the motor overall dimensions as similar as possible to the most recent traditional induction machine normally used for this application. The stack length is constrained to be lower than 60 mm and an $M470 - 50$ steel grade is considered for the lamination. Furthermore, in order to guarantee a proper saliency ratio an Integral Slot Distributed Winding (ISDW) has been chosen. Since these machines present an high anisotropic rotor, has been demonstrated that this winding arrangement is the most effective solution comparing to Fractional Slot Concentrated winding (FSCW) [33, 32].

The number of poles has been selected to $2p = 4$ to reduce the maximum supply frequency, since the speed at the spinning condition is high.

At first, a 24-slot stator lamination geometry has been designed considering a peak current density in the slot fixed to $J_{MAX} = 4.5 \text{ A}_{RMS}/\text{mm}^2$ and a fill factor is assumed to be $k_{fill} = 0.4$. The geometry has been tuned and analysed by means of $2D$ FEA. The stack length L_{stk} has been scaled in order to achieve the rated torque T_n , taking full advantage of the iron, working up to the knee of the iron $B - H$ characteristics.

In Fig. 7.4(a) a sketch of the initial SynRel motor cross section with three flux barrier per pole is shown. Besides investigating the torque behaviour, it is important to establish the influence of the various design parameters. Fig. 7.4(b) summarize the main geometrical parameters that are going to be considered as optimization variables in the design procedure.

where the main variables in the design space are:

- D is the inner diameter;
- h_{so} is the slot opening height;
- w_{so} is the slot opening width;
- g is the airgap;
- ϑ_{b1} , ϑ_{b2} , and ϑ_{b3} are the flux barrier angles;
- L_{air} is the total thickness of the three flux barriers along the rotor q -axis;
- $L_{air} + L_{fe}$ represents the rotor radius.

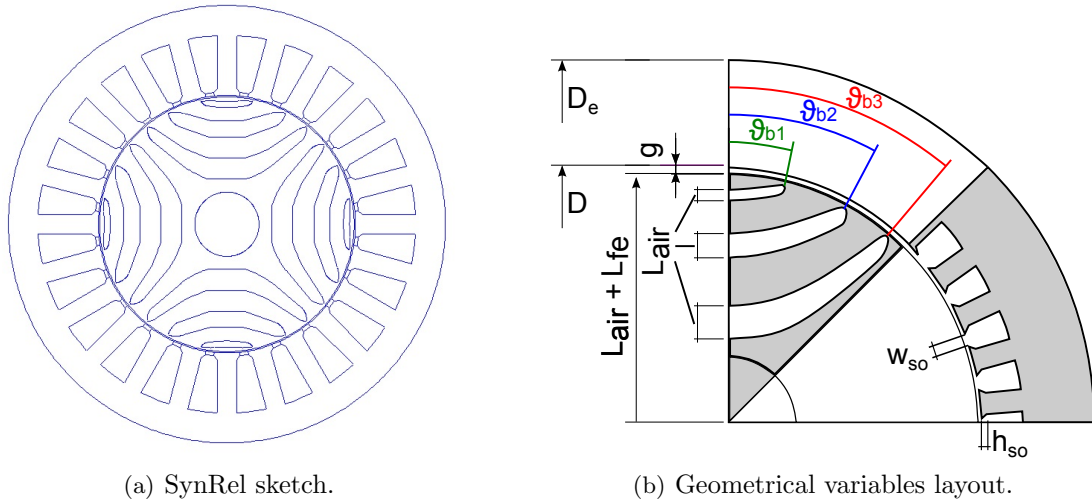


Figure 7.4: Preliminary SynRel motor design.

7.2.2 SynRel motor design and optimization

In the previous chapters the problem of the torque ripple in SynRel machines has been deeply investigated. An example of torque vs. angular position for the SynRel motor presented (Fig. 7.11(a)), is shown in Fig. 7.5(a). A small variation of both second and third flux barriers angle ϑ_{b3} , has been considered.

It can be noticed how the torque ripple is very sensitive to the flux barrier angles (see Tab. 7.1) moving from to 8.5% to 20.2%. Fig. 7.5(b) also shows how the torque varies according to the variation of outer diameter D_e .

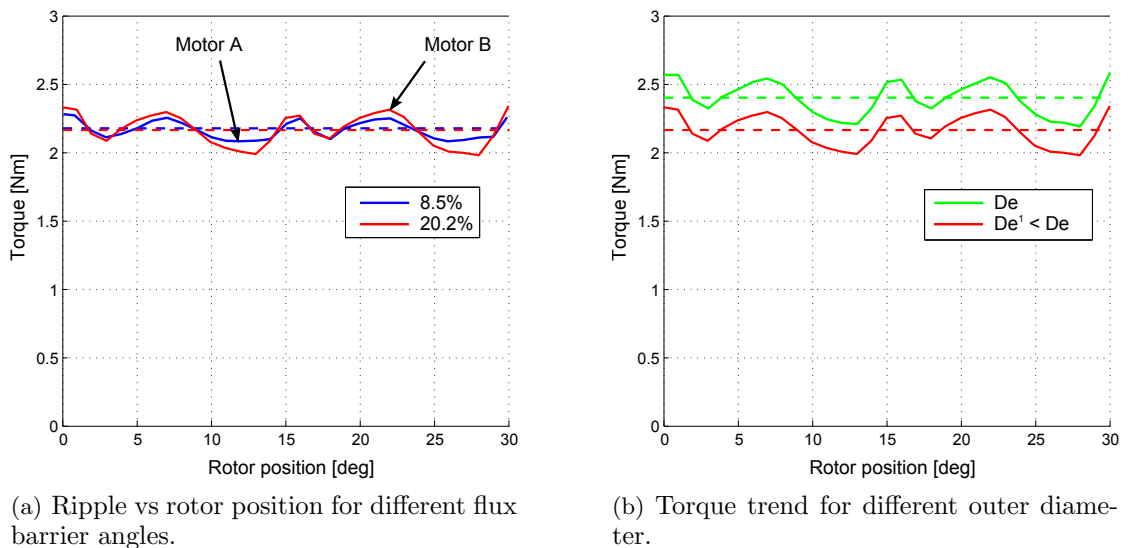


Figure 7.5: SynRel torque ripple.

Table 7.1: Torque ripple for different flux barrier angles

Barrier angle	<i>MotorA</i>	<i>MotorB</i>	<i>unit</i>
ϑ_{b1}	12	13	deg
ϑ_{b2}	27	28	deg
ϑ_{b3}	39.5	40	deg
ΔT	8.5	20.2	%

On the basis of the aforementioned stator lamination and the requested motor specification, a new optimized design has been evaluated.

MOGA-II optimization algorithm has been chosen with the aim of achieving a fast Pareto convergence. It is based on Multi Objective Genetic Algorithm (MOGA) and works on a set of design configurations that are periodically updated when one generation is completed. The algorithm type is a generational evolution.

The optimization algorithm has been performed to the aim of minimizing torque ripple and losses while improving the saliency ration, thus the reluctance torque expressed by the motor.

In this particular case, with the aim of simplify the optimization procedure, the key parameters considered are:

- the flux barriers end angles θ_{b1} , θ_{b2} , θ_{b3} ;
- the air coefficient k_{air} .

The objective functions instead are:

$$\min(\text{Torqueripple}) \quad (7.1)$$

$$\max(\text{Torque}) \quad (7.2)$$

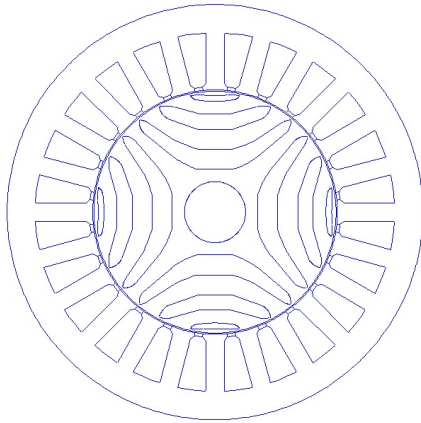
$$\max(\text{SaliencyRatio}) \quad (7.3)$$

As usual, the selection of the best solution is a trade-off between the results that better satisfy all the objective functions. Considering these motor topologies and the application the best compromise, among the solutions lying on the Pareto Front, is the one shown in Fig. 7.11(a), which is robust and presents the lower torque ripple and losses values. Fig. 7.6(b) represent the torque vs. angular position for the optimized motor. The torque ripple achieved is acceptable for the application ($T_r = 11\%$) and results comparable with the torque ripple measured in several induction motors used for the same purpose.

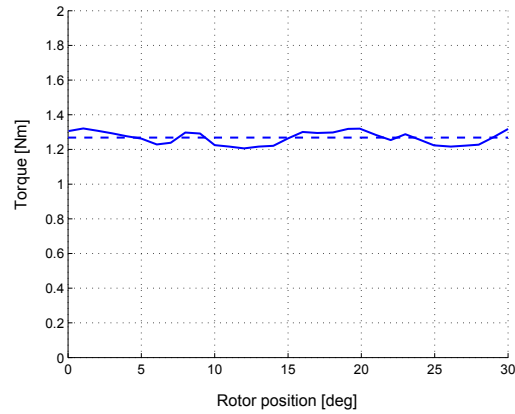
7.2.3 SynRel motor performance

The optimized solution has been analysed in order to determine the motor performance over all the operational speed range.

From the post processing of the FE analysis, the motor parameters has been determined. Figs. 7.7 and 7.8 report the motor inductances-current and magnetic flux-current characteristics that have been calculated from FEA.

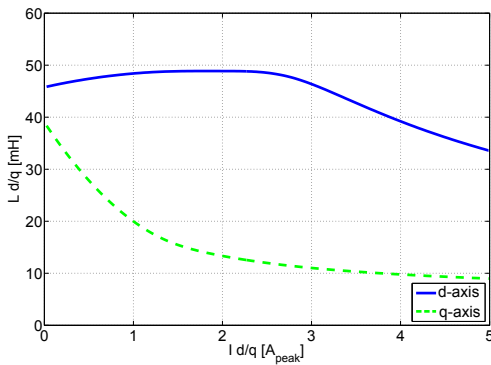


(a) SynRel sketch.

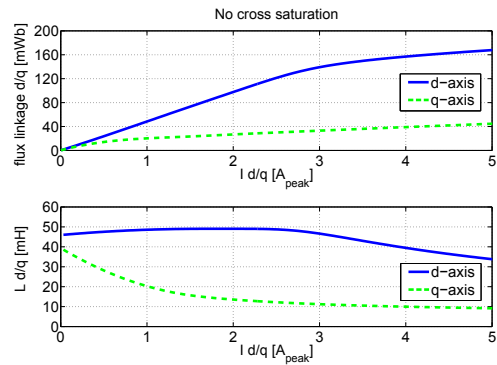


(b) Optimized torque ripple.

Figure 7.6: SynRel motor after optimization.



(a) L_d and L_q inductances.

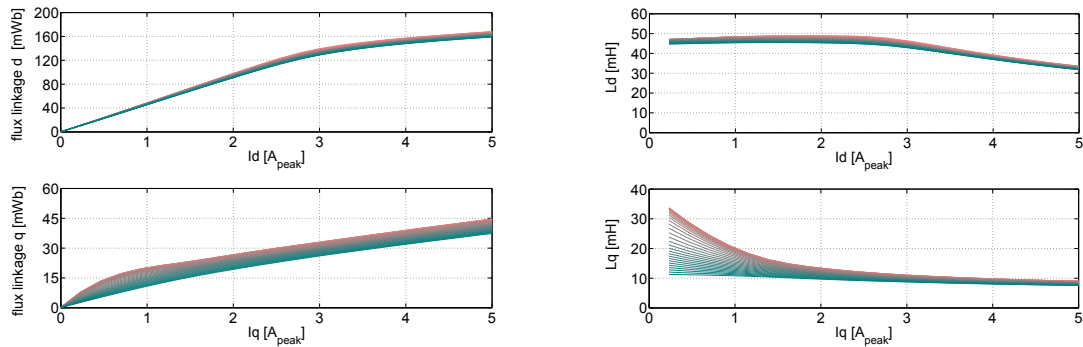


(b) L_d , L_q inductances and dq fluxes.

Figure 7.7: SynRel motor parameters (without considering the cross saturation).

Increasing the iron saturation the flux of one axis depends mainly to the respective current and secondarily to the current of the other axis: this behaviour is called cross saturation effect. As can be noted in Fig. 7.8 the cross saturation effect has an important influence on the motor parameters when saturation occurs. In particular, it can be noticed how the q-axis flux linkage λ_q and inductance L_q trends versus the I_q current, are importantly modified by the I_d current variation. Further details, to better understand the cross saturation phenomena, will be given in Chapter ??.

The current space vector trajectory has been evaluated by means of FEA, changing the d - and q - axis currents and computing the d - and q - axis flux linkages and torque. Fig. 7.9 shows this trajectory for the machines, according to the Maximum Torque Per Ampere (MTPA) locus and Flux Weakening (FW) up to the maximum speed (16000 rpm). It is worth noticing that the FW trajectory for SynRel motor does include the Maximum Torque Per Volt (MTPV) locus in order to reach the desired maximum speed.



(a) L_d and L_q inductances at different q-axis and d-axis currents respectively.

(b) L_d , L_q inductances and dq fluxes at different q-axis and d-axis currents respectively.

Figure 7.8: SynRel motor parameters (considering the cross saturation).

The torque and power vs. speed curves are shown in Fig. 7.10. SynRel machine torque has been determined considering a vector control that implements the strategy highlighted in Fig.7.9, thus trying to maximize the efficiency of the system.

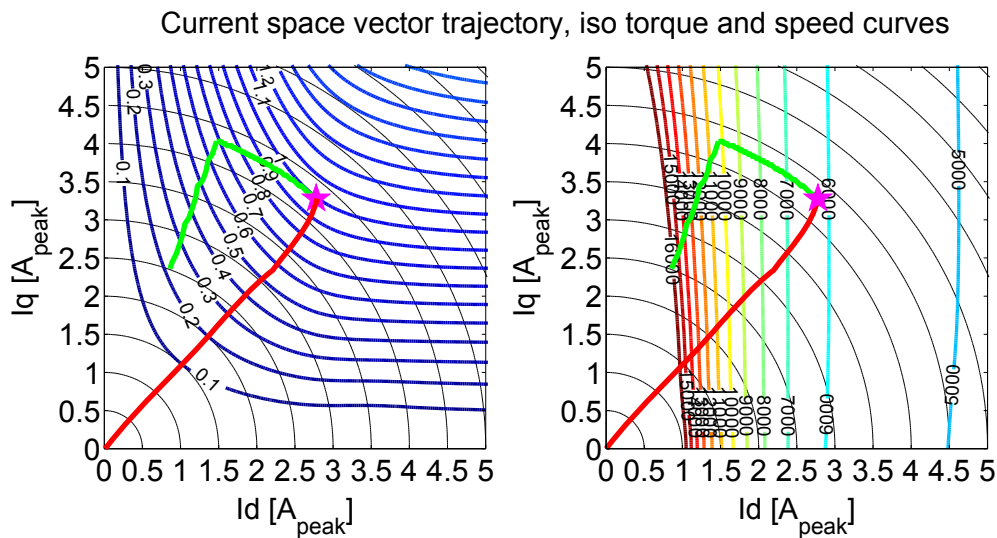


Figure 7.9: Current space vector trajectory: constant torque (left) and speed (right) contour maps.

In this case the resultant rated torque is satisfied and the base speed is around 5500 rpm. Nevertheless, if we consider the speed range over the base speed, the torque decrease considerably down to 0.22 Nm at the maximum speed (point B, Fig. 7.10). The power follows dropping to 400 W. The requirements reported in Fig. 7.3 are than not satisfied.

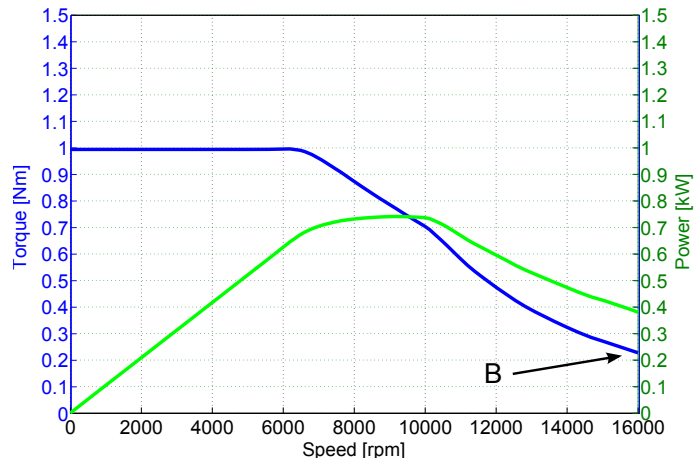


Figure 7.10: SynRel motor torque and power performance

With the aim of overcome to this issue, a few strategies could be applied:

- change the control strategy in order to improve the constant power speed range (at the expense of losing efficiency);
- introducing a certain amount of PMs in the rotor flux barriers with the aim of assisting the reluctance of the machine (PMASynRel machine).

In the next section a PMASynRel will be designed and optimized on the same basis with the aim of improving the performance of the SynRel motor, hence trying to match the application requirements.

7.2.4 Introduction of ferrite PMs in the rotor flux barriers

In Chapter 3 it has been shown how the insertion of the PMs in the SynRel geometry help in improving power factor, the torque and power performance of the machine over a wider speed range, satisfying the rated power requirements at maximum speed, without substantially increase the machine cost, when using ferrite PMs.

Nevertheless, if we consider the introduction of PMs in the SynRel machine analysed in the previous chapter, the field in the machine would be clearly different. Hence, even if the SynRel has been optimised for the reduction of torque ripple and losses, the simple operation of filling, fully or partially, the rotor flux barriers with a certain amount of PMs would not take to the same results. For example, placing ferrite PMs in the rotor structure, maintaining the same flux barrier shape optimized for the SynRel motor presented and optimized in Sec. 7.2.2, the effect on torque ripple is reported in Fig. 7.11(b). The PMASynRel motor electromagnetic torque is improved (22% higher than SynRel machine), however the torque ripple is worsen increasing from 18% to 29.5%.

For these reasons an optimization of the new PMASynRel rotor flux barrier shape is necessary in order to guarantee a lower torque ripple also for the PMASynRel motor.

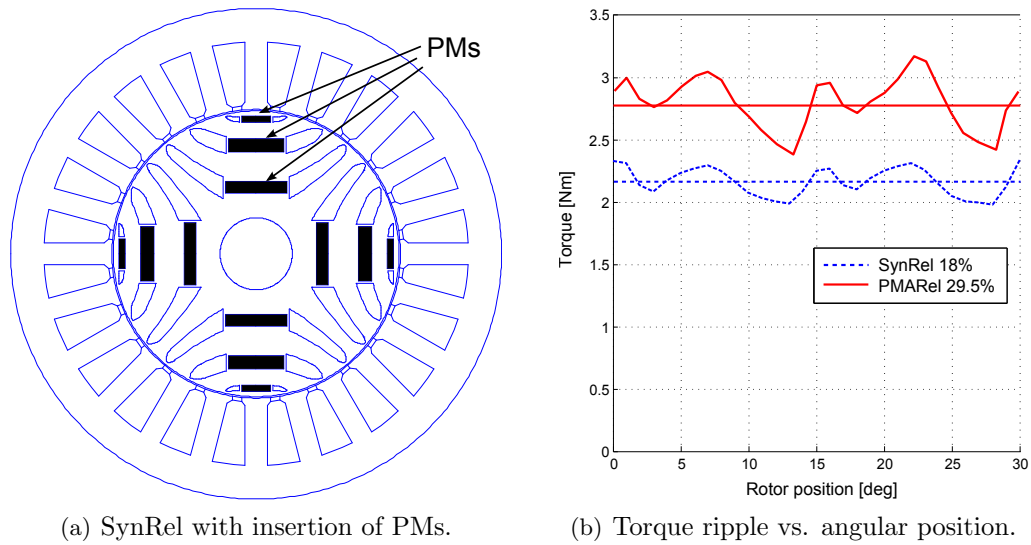


Figure 7.11: PMASynRel motor: permanent magnet effect on torque ripple.

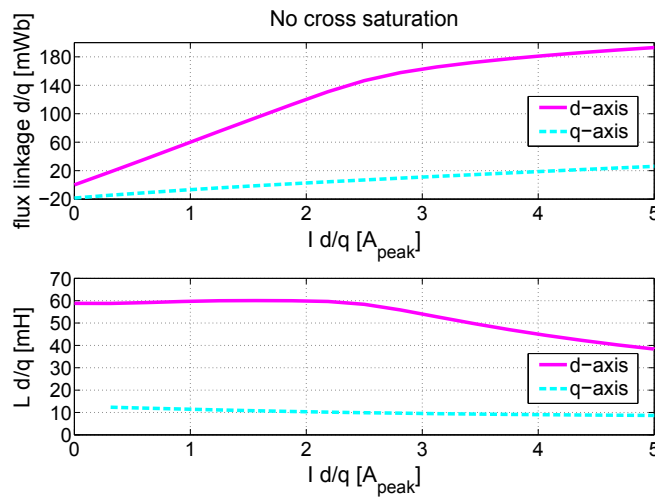


Figure 7.12: PMASynRel motor parameters (without considering the cross saturation).

Increasing the iron saturation the flux of one axis depends mainly to the respective current and secondarily to the current of the other axis: this behaviour is called cross saturation effect. As can be noted in Fig. 7.8 the cross saturation effect has an important effect on the motor parameters when saturation occurs.

The current space vector trajectory has been evaluated by means of FEA, changing the d - and q - axis currents and computing the d - and q - axis flux linkages and torque. Fig. 7.14 shows this trajectory for the machines, according to the Maximum Torque Per Ampere (MTPA) locus and Flux Weakening (FW) up to the maximum speed (16000 rpm). It is worth noticing that the FW trajectory for SynRel motor does include the Maximum Torque Per Volt (MTPV) locus in order to reach the desired maximum

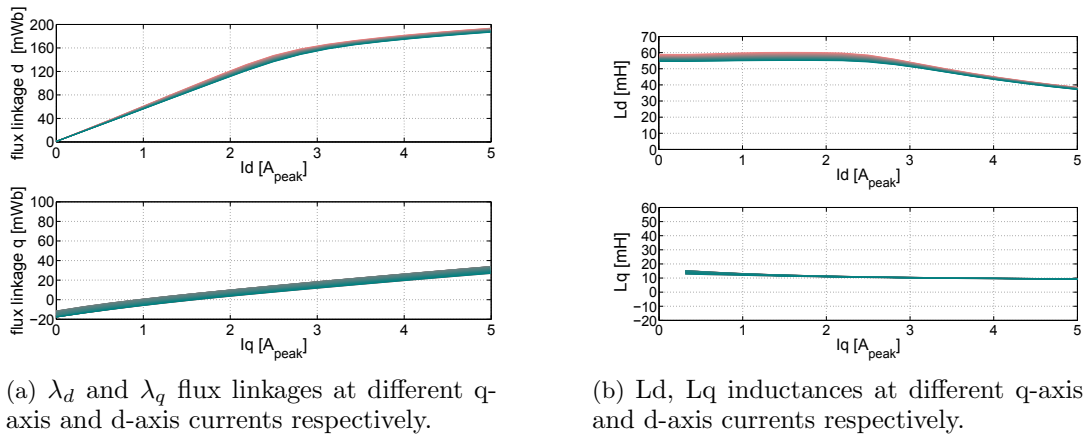


Figure 7.13: PMASynRel motor parameters (considering the cross saturation).

speed.

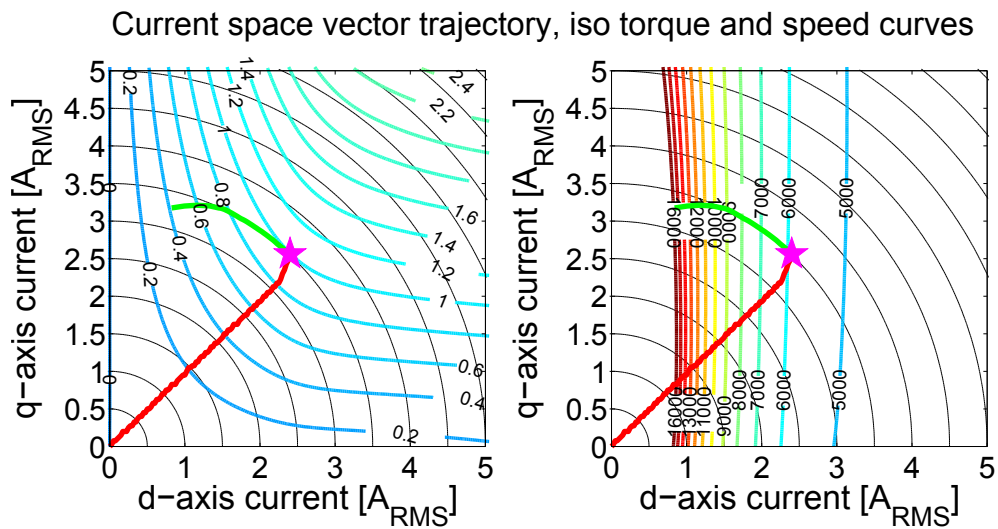


Figure 7.14: Current space vector trajectory: constant torque (left) and speed (right) contour maps.

The torque and power vs. speed curves are shown in Fig. 7.16. SynRel machine torque has been determined considering a vector control that implements the strategy highlighted in Fig.7.14, thus trying to maximize the efficiency of the system.

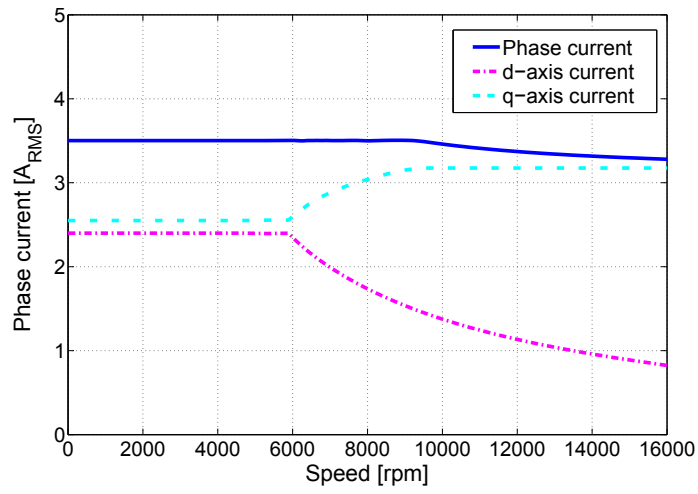


Figure 7.15: Phase current vs. speed.

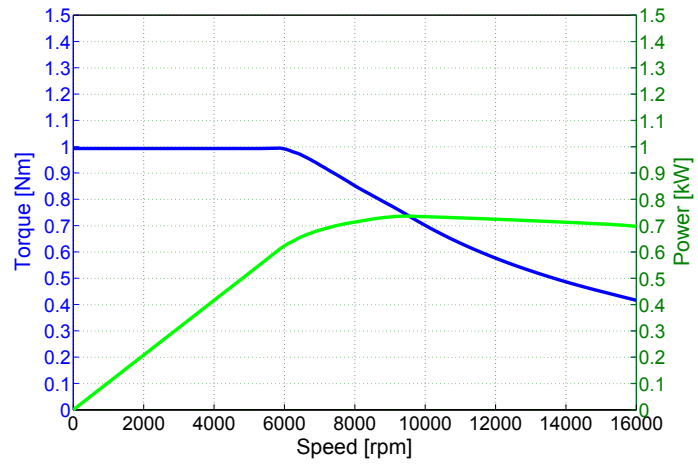


Figure 7.16: PMA SynRel motor torque and power performance

Part II

Synchronous Reluctance Machine: Analytical Modeling

Chapter 8

On the Analytical Estimation of the Airgap Field in Synchronous Reluctance Machine

Synchronous reluctance motors with rotor flux barriers are a promising type of electric machines thanks to various benefits, among the others, the absence of permanent magnets and rotor excitation. A challenge in the study of these motors is the accurate prediction of their air-gap field analytically taking into proper account the effects of rotor flux barriers. In this chapter a technique for this purpose based on reluctance network solution and winding functions is proposed. The reluctance associated to each flux barrier is computed by means of conformal mapping. Furthermore, the slotting effect is also considered through appropriate permeance function definition. Analytical results are compared to finite element analysis showing a good matching for various machine topologies characterized by a different number of flux barriers.

Introduction

Synchronous reluctance (SynRel) motors are interesting types of electric machines as they do not need either rotor excitation circuits or permanent magnets. They therefore feature an interesting technology in terms of robustness, production cost and construction simplicity [76],[77]. In the design of SynRel motors it is important to accurately predict machine performance in a very fast and flexible way so that many design solutions can be explored in a relatively short time. This particularly useful especially when the design is to be accomplished through genetic optimization procedures that require hundreds or thousands of designs to be automatically evaluated in search for the optimal configuration [78], [40]. Finite-element analysis (FEA) is the standard approach used in these cases but it suffers some drawbacks like long computation times and the need for a geometric model construction for each analysis. Hence analytical alternatives are highly desirable for their extremely fast computation times and their intrinsic flexibility. In the analytical evaluation of machine SynRel motor performance the problem mainly relates to a sufficiently accurate prediction of the air-gap magnetic field in all the possible operating conditions and for various rotor topologies, differing by the number and shape

of rotor flux barriers per pole. In fact, once the air-gap field is accurately determined, in fact, other quantities of interest, such as phase inductances, flux linkages and motor torque, can be determined with well-established methods [21], [9]. This chapter reports an analytical method for the estimation of the air-gap field distribution in a SynRel machine, with a rotor configuration including one or more circular-shaped flux barriers per pole. The methodology employs winding functions to determine the stator MMF and reluctance network for determining the flux densities in the air-gap and rotor domain. Reluctances associated to flux barriers are determined by means of conformal mapping. Stator slotting effects are taken into account by including them in the definition of the air-gap permeance function. The results obtained analytically are assessed by comparison with FEA showing a satisfactory matching for various rotor positions (with respect to stator MMF field) and for a different number and shape of rotor flux barriers.

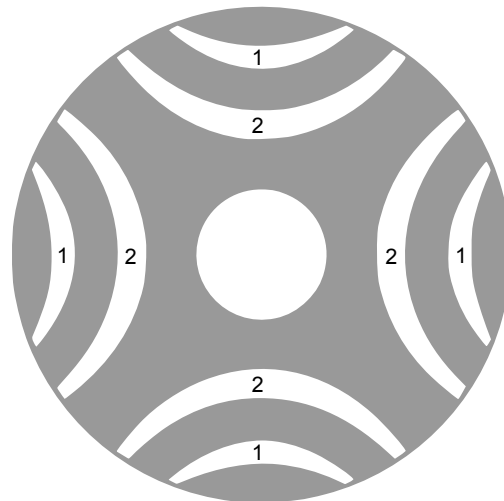


Figure 8.1: SynRel machine example rotor with two flux barriers per pole.

8.1 Modeling Assumption

The standard topology of the SynRel machine rotor which will be considered is sketched in Fig. 1 for the case of a four-pole geometry with two flux barriers per pole. The procedure will cover the case of a generic number of flux barriers. However, the hypothesis is made that the flux barrier contours are circumferential arcs, which is a quite realistic assumption in the most of designs [19], [79]. The geometric variants that the model can take into account regard the curvature radius of the various barrier contours as well as the distance between barriers of the same pole. One more hypothesis consists of neglecting saturation effects. Because iron ribs between flux barriers and rotor periphery are inevitably subject to magnetic saturation, the flux flowing through such ribs is disregarded [80]. As regards the stator winding, it is assumed to be a conventional distributed three-phase one.

8.2 Computing Stator Magneto Motive Force

As a first step, a general method is presented for computing air-gap MMF field due to stator currents as a function of both time and space. For this purpose, let us fix an angular coordinate x measured in electrical radians along the mean air-gap circumference and call $i(t, n)$ the current flowing in phase n (with $n = 0, 1, 2$) at the time instant t . The MMF distribution will be:

$$F(x, t) = \sum_{n=0}^2 w(x, n) \cdot i(t, n) \quad (8.1)$$

where $w(x, n)$ is the winding function of a phase [81] which can be explicitly written as:

$$w(x, n) = \sum_{k=1,3,5,\dots} \left[W_k \cdot \cos \left[k \cdot \left(x - \frac{2}{3}\pi \cdot n + \varphi_0 \right) \right] \right] \quad (8.2)$$

where k is the harmonic order, W_k are winding function Fourier coefficients, n the phase index ($n = 0, 1, 2$) and φ_0 the initial phase angle. Fourier coefficients W_k are:

$$W_k = \frac{4}{\pi} \cdot \frac{N_s}{b} \cdot \frac{\sin(\pi \cdot k \cdot \frac{r}{2})}{k} \cdot \frac{\sin(\alpha_s \cdot q \cdot \frac{k}{2})}{\sin(\alpha_s \cdot \frac{k}{2})} \quad (8.3)$$

where N_s is the number of series-connected turns per phase, b is the number of parallel paths per phase, r is the coil throw to pole pitch ratio, α_s is the slot pitch in electrical radians and q is the number of slots per pole per phase. The currents in each phase n , are assumed to have a sinusoidal waveform, so that they can be expressed as:

$$i(t, n) = I_0 \cdot \cos(\omega_0 \cdot t - \beta \cdot n) \quad (8.4)$$

where I_0 is the peak value of the current distribution, ω_0 the electric pulsation and $\beta = 2\pi/3$ the shift angle between phase currents in electrical radians.

8.3 Modeling of SynRel Motor Through Reluctance Networks

The SynRel motor is modelled through reluctance network approach. To fix ideas, let us refer to the two-pole machine schematic shown in Fig. 8.2, which features two barriers per pole. In this schematic, the slotting effect is preliminary disregarded and the stator is modelled as a smooth hollow cylinder with uniform infinite magnetic permeability. Letters A, B, S, R represent the nodes in the reluctance network and identify machine regions where no MMF drop occurs. These nodes are mutually connected by appropriate reluctances and MMF sources. The geometric topology illustrated in Fig. 8.2 can be naturally mapped into the equivalent reluctance network shown in Fig. 8.3. The nomenclature adopted is the following:

- $F_{i,j}$ are the MMF generators due to the stator currents;

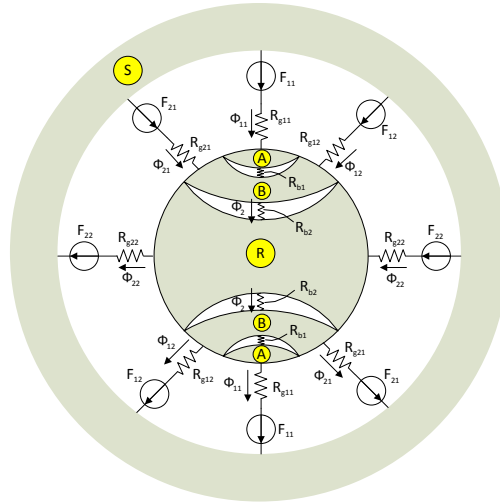


Figure 8.2: Magnetic circuit layout for a two-pole SynRel motor with two barriers per pole.

- $R_{gi,j}$ are air-gap reluctances;
- R_{bi} is the reluctance of the i^{th} flux barrier:
- $\phi_{i,j}$ are the fluxes along various paths as shown in Fig. 8.2.

The details on how the parameters of the reluctance network are to be computed will be given in the next Section. What is next discussed is the possibility to noticeably simplify the complete network shown in Fig. 8.3 by means of reduction techniques derived from electric circuit theory.

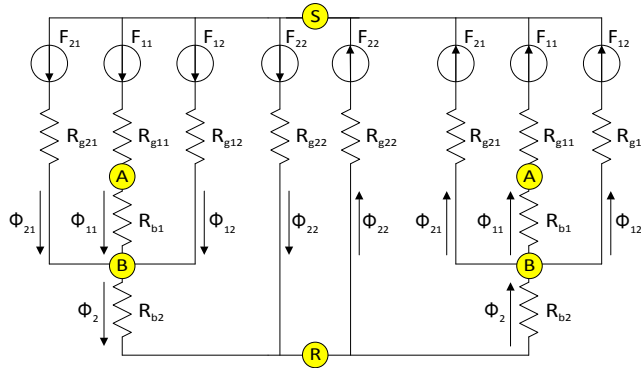


Figure 8.3: Complete reluctance network for a SynRel motor with two poles and two barrier per pole.

A first reduction can be done observing that the central branches that include MMF sources F_{22} in Fig. 8.3 can be disregarded as they give an overall null contribution in terms of fluxes. Furthermore, from obvious symmetry considerations, the equivalent network shown in Fig. 8.3 can be redrawn as shown in Fig. 8.4. As a further step, using

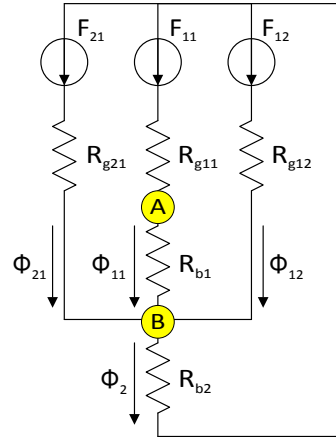


Figure 8.4: Reluctance network resulting from reduction of the circuit shown in Fig. 8.3.

Millman's formula, the equivalent circuit shown in Fig. 8.5(a) is obtained, where

$$F_{eq}(t, x_r) = \left(\frac{F_{11}}{R_{g11} + R_{b1}} + \frac{F_{12}}{R_{g12}} + \frac{F_{21}}{R_{g21}} \right) \cdot R_{eq}^{-1} \quad (8.5)$$

$$R_{eq} = \left(\frac{1}{R_{g11} + R_{b1}} + \frac{1}{R_{g12}} + \frac{1}{R_{g21}} \right)^{-1} \quad (8.6)$$

Finally, the simple equivalent circuit shown in Fig. 8.5(b) is elementarily derived to compute the flux ϕ_2 flowing through the second flux barrier (Fig. 8.2) as:

$$\phi_2 = \frac{F_{eq}}{R_{eq} + R_{b2}} \quad (8.7)$$

Once ϕ_2 has been determined, all the other fluxes $\phi_{i,j}$ can be computed through elementary calculations based on the equivalent circuit shown in Fig. 8.4.

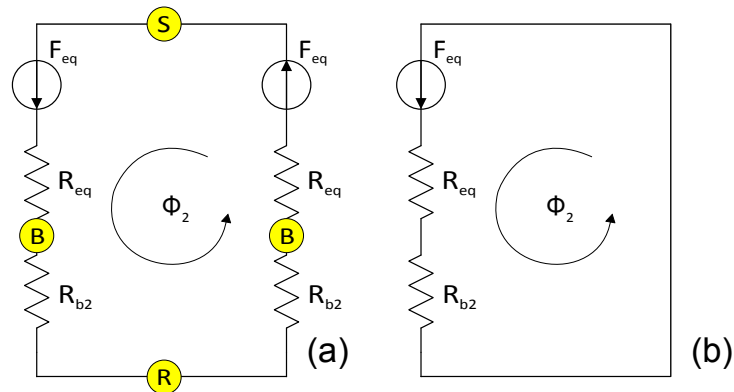


Figure 8.5: Equivalent circuit from reduction of networks shown in Fig. 8.4.

8.4 Computation of Reluctance Network Parameters

In this Section, some formulas are provided to determine the parameters (MMF sources and magnetic reluctances) that appear in the reluctance network models discussed in the previous Section. For the purpose of parameter computation, let us consider the rotor q axis position as $x=x_r$ with respect to an arbitrary stator axis s , (Fig. 8.6), and identify the position of the two flux barriers through the angles x_1 and x_2 as illustrated in Fig. 8.6.

Based on these definitions, the air-gap reluctances can be computed as:

$$R_{g11} = \frac{1}{\mu_0} \cdot \frac{g}{2x_1 \cdot R \cdot L} \cdot p \quad (8.8)$$

$$R_{g12} = R_{g21} = \frac{1}{\mu_0} \cdot \frac{g}{(x_2 - x_1) \cdot R \cdot L} \cdot p \quad (8.9)$$

$$R_{g22} = \frac{1}{\mu_0} \cdot \frac{g}{(\pi - 2x_2) \cdot R \cdot L} \cdot p \quad (8.10)$$

where g is the air-gap width, p is the number of pole pairs, R is the average air-gap radius and L is the core length. The MMF sources are computed from the general MMF

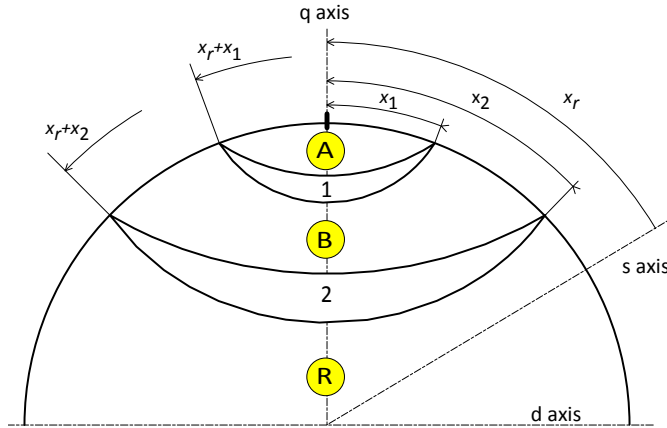


Figure 8.6: Definition of angles x_r , x_1 and x_2 .

field produced by stator currents (Section 8.2) as follows:

$$F_{11}(t, x_r) = \frac{1}{2x_1} \cdot \int_{x_r-x_1}^{x_r+x_1} F(x, t) dx \quad (8.11)$$

$$F_{12}(t, x_r) = \frac{1}{x_2 - x_1} \cdot \int_{x_r+x_1}^{x_r+x_1+x_2} F(x, t) dx \quad (8.12)$$

$$F_{21}(t, x_r) = \frac{1}{x_2 - x_1} \cdot \int_{x_r-x_1-x_2}^{x_r-x_1} F(x, t) dx \quad (8.13)$$

The reluctance associated to each flux barriers, characterized by the dimensions τ , d , h shown in Fig. 7 (w -plane), is computed by applying the conformal map

$$z = atan \frac{2w}{\tau} \quad (8.14)$$

to the physical w -plane where the barrier lies. The result of the conformal mapping in the z -plane is a rectangle having dimensions X , Y . The reluctance of the i -th barrier (which is invariant through the conformal mapping transformation) is therefore computed as:

$$R_{bi} = \frac{1}{\mu_0} \cdot \frac{X}{Y \cdot L} \quad (8.15)$$

where L is the core length and X , Y are the dimensions of the rectangle resulting in the z -plane from applying (8.14) to the i -th barrier geometry drawn in the w -plane (Fig. 8.7).

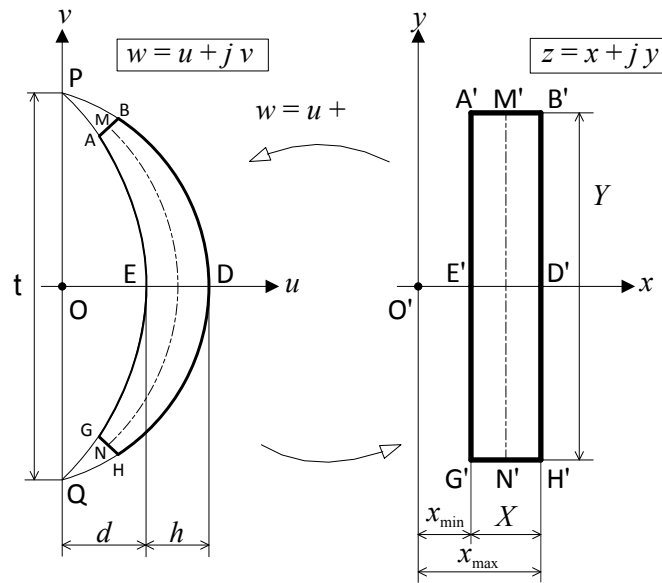


Figure 8.7: Conformal mapping transformation for a flux barrier.

8.5 Airgap Flux Density Computation From Reluctance Network Solution

The general approach for computing the air-gap flux density (radial component) consists of three steps, that are: computing the flux density without slotting and flux-barrier effects; including flux barrier effects; including slotting effects. The three steps are detailed next.

Flux density with no barrier and no slotting effects

The flux density B_{ug} in the hypothesis of perfectly uniform air-gap permeance is simply computed from the MMF as:

$$B_{ug}(x, t) = \frac{\mu_0}{g} \cdot F(x, t) \quad (8.16)$$

where subscript ug stands for *uniform gap*.

Inclusion of flux barrier effects

The approach for including flux-barrier effects is to compute the flux density variation that occurs in various air-gap regions due to the MMF drop across flux barriers. For example, in the air-gap region spanning between $x_r - x_1$ and $x_r + x_1$ (Fig. 8.6) there are two MMF drops to be accounted for, i.e. those occurring in both the flux barriers; instead, in the region spanning between $x_r - x_2$ and $x_r - x_1$, only one MMF, occurring across flux barrier 2 needs to be taken into account. Based on these considerations, the flux density variations $\Delta B_{i,j}$ can be computed as

$$\Delta B_{11}(t, x_r) = \frac{\mu_0}{g} \cdot [F_{11}(t, x_r) \cdot R_{b1} + F_{22}(t, x_r) \cdot R_{b2}] \quad (8.17)$$

$$\Delta B_{12}(t, x_r) = \frac{\mu_0}{g} \cdot [F_{22}(t, x_r) \cdot R_{b2}] \quad (8.18)$$

These variations are to be summed to the flux density (16) that does not account for flux barriers. Thus the equations given in (19) and (20) are obtained, respectively for one and two flux barriers per pole, where gb indicates that the flux density refers to the gap considering flux barriers.

Inclusion of slotting effects

Finally, the flux density distribution $B_{gbs}(x,t)$ is determined including stator slotting effects as well (subscript gbs indicates that the flux density is in the gap including both flux barriers and slotting effects).

$$B_{gb}(x, t, x_r) = \begin{cases} B_g(x, t) - \Delta B_{11}(t, x_r) & \text{if } \begin{aligned} &0 \leq |\text{mod}(x - x_r, 2\pi)| \leq x_1 \\ &\vee \quad 2\pi - x_1 \leq |\text{mod}(x - x_r, 2\pi)| \leq 2 \cdot \pi \end{aligned} \\ B_g(x, t) + \Delta B_{11}(t, x_r) & \text{if } \pi - x_1 \leq |\text{mod}(x - x_r, 2\pi)| \leq \pi + x_1 \\ B_g(x, t) & \text{otherwise} \end{cases} \quad (8.19)$$

$$B_{gb}(x, t, x_r) = \begin{cases} B_g(x, t) - \Delta B_{11}(t, x_r) & \text{if } 0 \leq |\text{mod}(x - x_r, 2\pi)| \leq x_1 \\ & \vee 2\pi - x_1 \leq |\text{mod}(x - x_r, 2\pi)| \leq 2 \cdot \pi \\ B_g(x, t) + \Delta B_{11}(t, x_r) & \text{if } \pi - x_1 \leq |\text{mod}(x - x_r, 2\pi)| \leq \pi + x_1 \\ B_g(x, t) - \Delta B_{12}(t, x_r) & \text{if } x_1 \leq |\text{mod}(x - x_r, 2\pi)| \leq x_2 \\ B_g(x, t) - \Delta B_{12}(t, x_r) & \text{if } x_1 + \pi \leq |\text{mod}(x - x_r, 2\pi)| \leq x_2 + \pi \\ B_g(x, t) - \Delta B_{12}(t, x_r) & \text{if } \pi - x_2 \leq |\text{mod}(x - x_r, 2\pi)| \leq \pi - x_1 \\ B_g(x, t) - \Delta B_{12}(t, x_r) & \text{if } 2\pi - x_2 \leq |\text{mod}(x - x_r, 2\pi)| \leq 2\pi - x_1 \\ B_g(x, t) & \text{otherwise} \end{cases} \quad (8.20)$$

This is done by multiplying the flux density B_{gb} 8.19 - 9.43, that considers flux barriers only, by a suitable non-dimensional permeance function $p_{slot}(x)$ as follows:

$$B_{gbs}(x, t, x_r) = p_{slot}(x) \cdot B_{gb}(x, t, x_r) \quad (8.21)$$

The function p_{slot} is defined using the so called Weber's theory to model slotting effects [82] and takes the form:

$$p_{slot}(x) = \left(1 - 2\gamma \cdot \left| \sin \left(\frac{Z}{2p} \cdot x \right) \right| \right)^{2\alpha} \quad (8.22)$$

where:

$$\gamma = \frac{1 + u^2 - 2u}{2(1 + u^2)} \quad , \quad \alpha = \frac{\tau_t}{\tau_s} \quad (8.23)$$

$$u = \frac{\tau_s}{2g} + \sqrt{1 + \left(\frac{\tau_s}{2g}\right)^2} \quad (8.24)$$

being g the gap width, τ_s is the slot opening width, τ_t the tooth width at the air-gap and Z the number of slots.

8.6 Validation by Finite Element Analysis

Finally, the method proposed in this chapter is assessed by comparison with Finite Element Analysis (FEA) on the example machine whose cross section is given in Fig. 8.1. The machine is characterized by the data given in Table 9.1.

The results of the comparison are shown in Fig. 8 for the case of a machine topology with only one flux barrier per pole (the cross section is the same as shown in Fig. 8.1 without the flux barrier 2). The case studies considered for Fig. 8 are: rotor q -axis aligned with stator MMF axis in (a) and (b); rotor q -axis shifted by 15 mechanical degrees with respect to stator MMF field axis in (c) and (d). In all cases, the stator is

Table 8.1: Characteristic Data of the example SynRel Machine.

Name	Symbol	Value	Unit
Stator bore radius	D_s	30	mm
Air gap width	g	0.3	mm
Number of stator slots	Z	24	–
Number of poles	$2p$	4	–
Number of conductors per slots	N_s	20	–
Slot opening width	τ_s	2	mm
Tooth width at the air gap	τ_t	5.8	mm
Angle x_1 (8.6)	x_1	21.4	mech deg
Angle x_2 (8.6)	x_2	34.2	mech deg
1-st flux barrier width (8.6)	h_1	2.5	mm
2-st flux barrier width (8.6)	h_2	3.0	mm
Stack lenght	L	50	mm

energized with a peak current of 5.6 A per conductor of phase A and a peak current of -2.8 A per conductor of phases B and C. Furthermore, in (a) and (c) the analytical model (8.19) is employed, i.e. slotting effects are disregarded, while the latter are accounted for in (b) and (d) which are plotted based on equation (9.43). Overall, it can be seen that the inclusion of slotting effects brings a moderate but visible benefit in matching FEA results through the analytical approximation. Finally, a comparison

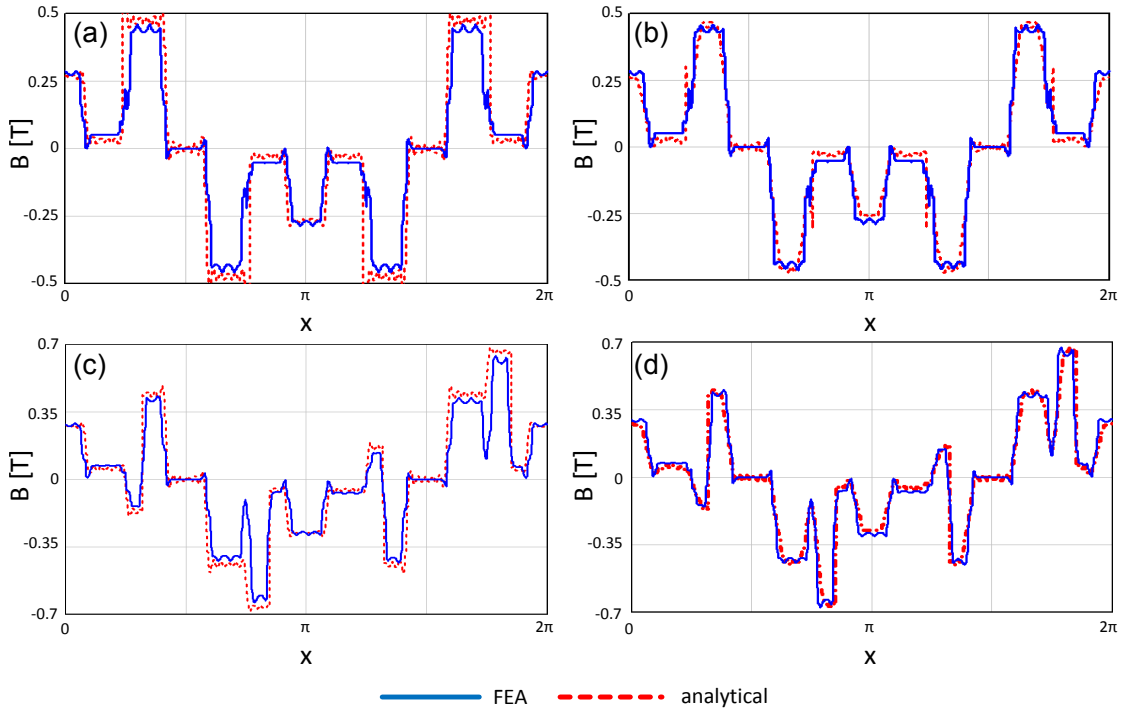


Figure 8.8: Air-gap flux density computed by FEA and analytically for: (a) and (b): rotor position with q axis aligned with stator MMF axis; (c) and (d) with rotor q axis displaced by 15 mechanical degrees with respect to stator MMF axis. In (a), (c) slotting effects are not accounted for, while they are in (b) and (d).

between FEA and analytical simulations is shown in Fig. 9 for the case of the SynRel machine topology with two barriers per pole (Fig. 8.1, Table 9.1). Again, the comparison is plotted in (a) assuming rotor q -axis aligned with stator MMF axis and in (b) with a shift displacement of 15 mechanical degrees.

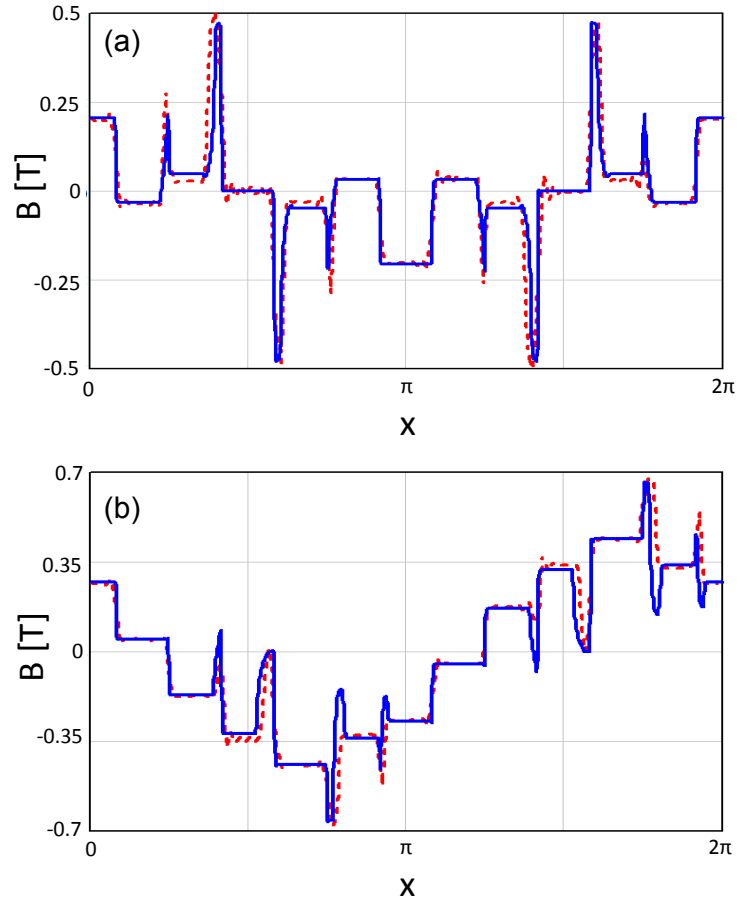


Figure 8.9: Air-gap flux density computed by FEA and analytically for: (a) : rotor position with q axis aligned with stator MMF axis; (c) with rotor q axis displaced by 15 mechanical degrees with respect to stator MMF axis. Both results are including the slotting effects.

8.7 Conclusions

SynRel motors are interesting synchronous electrical machines thanks to various advantageous features, like the absence of permanent magnets and excitation circuits and the structural simplicity and robustness. Due to the relatively complex rotor topology, however, these machines are quite challenging to study with fast analytical methods, i.e. without the use of time-consuming FEA. This study proposes some possibly useful methods to a rapid and precise analytical computation. The proposed approach is based on modeling stator MMF through the winding function theory, while rotor structure is modeled by means of an equivalent reluctance network. The reluctances associated to

flux barriers are computed by means of conformal mapping techniques. Slotting effects are also included in the model through an appropriate non-dimensional permeance function. Based on these techniques, explicit formulas are presented for air-gap field computation in the hypothesis of unsaturated core. The accuracy of the proposed formulations are assessed by comparison with an example SynRel motor characterized by one or two flux barriers per pole. The comparison shows a satisfactory matching between analytical predictions and FEA results.

Chapter 9

Analytical Modeling of Split-Phase Synchronous Reluctance Machines

Synchronous reluctance (SynRel) motors with rotor flux barriers are gaining increasing attractiveness in automotive applications thanks to their cheap, rugged and magnet-free rotor construction. When equipped with a split-phase stator winding and supplied from multiple inverters, these machines can exhibit further merits as traction motors in regard to enhanced fault tolerance compared to conventional three-phase solutions. Since SynRel motors are usually designed through iterative optimization techniques, it is highly desirable to have accurate and fast methods to predict their performance without the need for time-consuming finite element analysis (FEA) simulations. An analytical procedure is set forth in this chapter to analytically model and simulate a SynRel motor with a split-phase stator winding through a magnetic equivalent circuit (MEC) technique. MEC parameters are computed from analytical formulas describing the air-gap magneto-motive force distribution and the magnetic field inside flux barriers. As an output, the air-gap flux density of the SynRel motor can be computed through the presented technique at any operating point. Results are positively assessed by comparison with FEA simulation on a sample SynRel motor including magnetic saturation effects.

Introduction

Synchronous reluctance (SynRel) motors are gaining increasing attractiveness as vehicle traction motor drives thanks to their rugged, cheap and magnet-free rotor construction [1], [15]. Promising applications of SynRel motors, possibly assisted by permanent magnets, in the automotive field have been recently reported in the literature [11], [12]. An effective way to cope with the strict reliability requirements proper to vehicle traction drives is to equip the electric motor with a split-phase (or multiple three-phase) winding, consisting of two or more three-phase winding sections, each fed by an inverter independently [83]. In this chapter, a SynRel motor with a split-phase stator winding is in fact considered as a possible interesting electric machine topology for fault-tolerant magnet-free vehicle traction applications. SynRel motors are usually characterized by

a round rotor in which magnetic anisotropy (required for reluctance torque production) is achieved by suitably shaped flux barriers [19], [84]. Flux barrier geometry is often defined through an iterative optimization procedure [84] with different possible goals, such as torque ripple enhancement [85], [21] and core loss reduction [9] or in a multi-objective framework [84]. In the optimization procedures, hundreds or thousands of design solutions need to be explored within a reasonable timeframe, which calls for very fast methods for machine analysis, possibly avoiding time-consuming FEA simulations. For this purpose, analytical techniques based on magnetic equivalent circuits (MEC) have been proposed in the literature [21], [9] for the study of SynRel motors (or permanent-magnet assisted ones) featuring three-phase stator winding and flux barriers of roughly uniform width. In this work, MEC technique is extended to study split-phase SynRel motors with an arbitrary set of stator windings and with flux barriers having a circular shape, which are widely used for purely reluctance (magnet-free) motors [15], [19], [86]. The MEC parameters (namely MMF sources and magnetic reluctances) are analytically computed based on motor design data. The MEC analytical solution is used to obtain an accurate estimation of SynRel motor air-gap flux for any rotor position and supply currents. Accuracy of results is successfully assessed by comparison with FEA simulations on a sample six-phase SynRel motor including magnetic saturation effects.

9.1 Modeling Assumption

In this section, a SynRel motor with a split-phase stator winding which includes a generic number N of three-phase sets is taken into account. As shown in Fig. 9.1, the phases of the N sets are named (A_0, B_0, C_0) , (A_1, B_1, C_1) , ..., $(A_{N-1}, B_{N-1}, C_{N-1})$ and the three-phase sets are displaced $60/N$ electrical degrees apart. Each three phase set is suitable for being supplied by an inverter independently (Fig. 9.2).

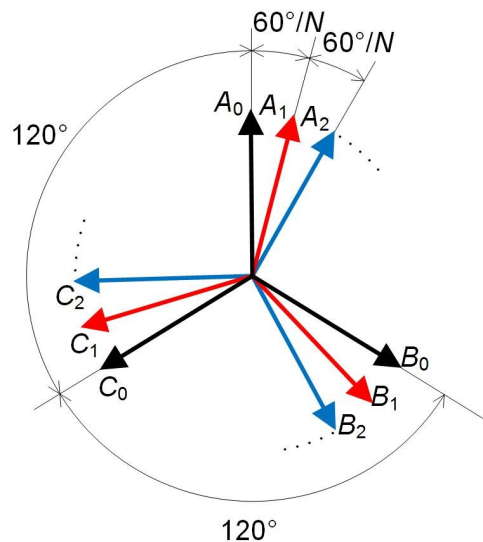


Figure 9.1: Phase arrangement and naming for a split-phase winding configuration with N three-phase sets.

In normal operation, all the winding sets are equally loaded, but under faulty or abnormal conditions it may happen that the output currents I_0, I_1, \dots, I_{N-1} are different in the N inverters (possibly being equal to zero). This brings to the possibility for the

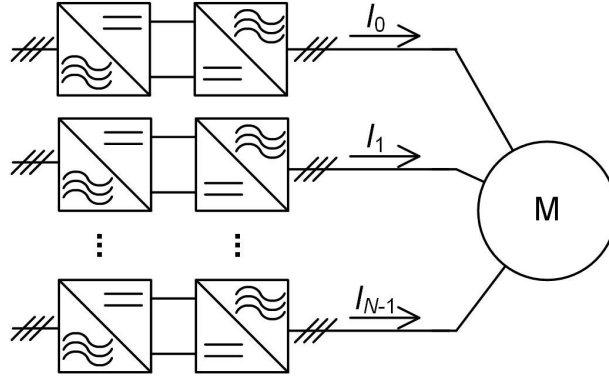


Figure 9.2: Overall drive schematic for a split-phase motor with N independently fed stator sets.

drive to operate at reduced power in case of fault on one or more supplying inverters or winding sections. The way in which phases are physically arranged in stator slots is exemplified in Fig. 9.3, where the case is illustrated of a four-pole dual-three-phase ($N = 2$) winding configuration with a dual-layer short-pitch coils with two slots per pole per phase. Regarding the rotor, a generic number of flux barriers is assumed (Fig.

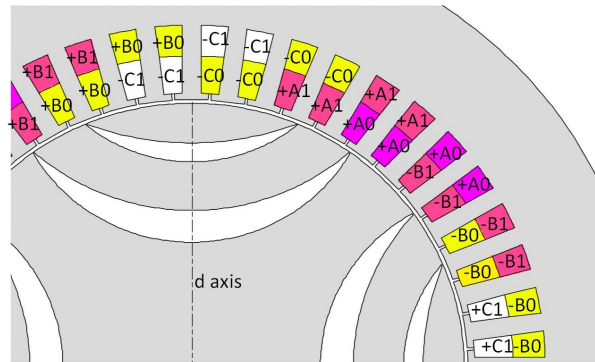


Figure 9.3: Example of a four-pole dual-three-phase SynRel motor with two round barriers per pole. Phase arrangement over a pole span.

9.3 shows the case of two barriers per pole). For the purpose of MEC definition, the case of uniform-width C-shaped barriers is the most simple and is also addressed in [84], [21], [9] for three-phase machines. The most challenging case of circular flux barriers (Fig. 9.3, [87], [19], [14]) will be then assumed in the following as it requires a more complex procedure to analytically find the MEC reluctance associated to each barrier. Furthermore, it will be assumed that flux barriers are delimited by circumferential arcs as depicted in Fig. 9.4. Here, the generic i -th flux barrier is represented for example. Its borders lie on circumferences a_i (of radius r_{ai} and center C_{ai}) and Γ_{bi} (of radius r_{bi}

and center C_{bi}) and intersect the outer rotor circumference (having radius r and center C) at points P_{ai} , Q_{ai} and P_{bi} , Q_{bi} , respectively. These intersection points are identified by the two angles a_i and b_i centered in C , as shown in Fig. 9.4. The geometry of the

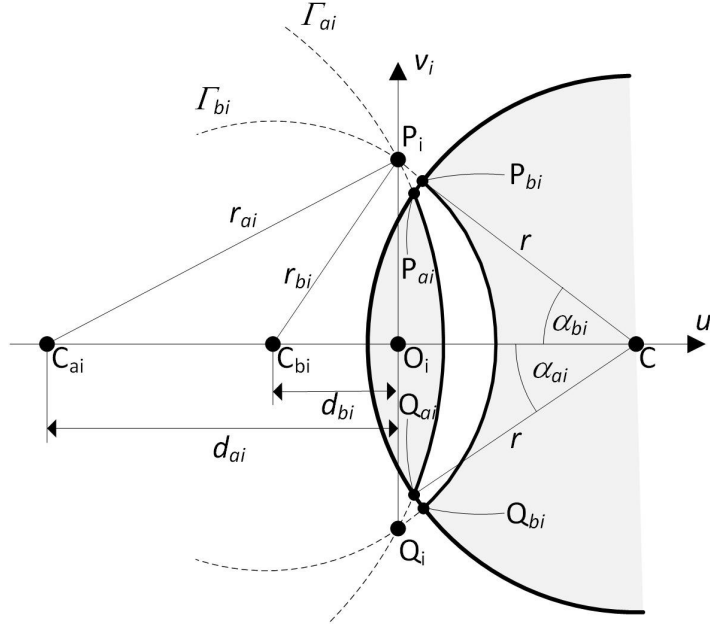


Figure 9.4: Characteristic geometric quantities for the i -th flux barrier.

i -th flux barrier is hence fully determined by the two radii r_{ai} , r_{bi} and by the two angles a_i and b_i . In fact, the centers C_{ai} , C_{bi} are consequently defined by their distance from the rotor center C as follows:

$$\overline{CC_{ai}} = r \cdot \cos(\alpha_{ai}) + \sqrt{r_{ai}^2 - r^2 \cdot \sin^2 \alpha_{ai}} \quad (9.1)$$

$$\overline{CC_{bi}} = r \cdot \cos(\alpha_{bi}) + \sqrt{r_{bi}^2 - r^2 \cdot \sin^2 \alpha_{bi}} \quad (9.2)$$

For the following, it is also useful to observe that the two circumferences Γ_{ai} and Γ_{bi} intersect at points P_i , Q_i placed outside the rotor. The intersection of segment P_iQ_i with the barrier symmetry axis is called O_i in Fig. 9.4 and from elementary geometric calculations one can find the distance of O_i from rotor center C and the length of segment P_iQ_i as follows:

$$\overline{CO_i} = \frac{\overline{CC_{ai}}^2 - \overline{CC_{bi}}^2 - r_{ai}^2 + r_{bi}^2}{2(\overline{CC_{ai}} - \overline{CC_{bi}})} \quad (9.3)$$

$$\overline{P_iQ_i} = \sqrt{\left[(\overline{CC_{ai}} - \overline{CC_{bi}}) - \frac{(r_{ai} - r_{bi})^2}{(\overline{CC_{ai}} - \overline{CC_{bi}})} \right]} \times \quad (9.4)$$

$$\times \sqrt{\left[\frac{(r_{ai} + r_{bi})^2}{(\overline{CC}_{ai} - \overline{CC}_{bi})} - (\overline{CC}_{ai} - \overline{CC}_{bi}) \right]}$$

The geometric relationships mentioned above will be used in Section V for the magnetic field analysis in the flux barriers. Finally, saturation effects are neglected, or, more precisely, supposed to occur only in the iron bridges between flux barriers and the outer rotor periphery in such a way that no flux passes through these bridges. Such hypothesis is normally assumed in the study of SynRel machines through MEC techniques [21], [9] and is very well matched for sufficiently small bridge widths, as later on confirmed by comparing analytical results with FEA simulations where saturation effects are included (Section VII).

9.2 Motor Modeling with MEC Technique

The MEC modeling of the SynRel motor is illustrated in Fig. 5 where, for the sake of clarity and simplicity, the case of a two pole machine with two barriers per pole (indicated as barrier 1 and 2 for one pole, 1' and 2' for the other one) is taken into account. The basic principle for MEC modeling is that the air-gap is subdivided into various regions (sectors), named "11", "12", "21", "22" by the points (Fig. 9.4) where barriers intersect the rotor outer periphery.

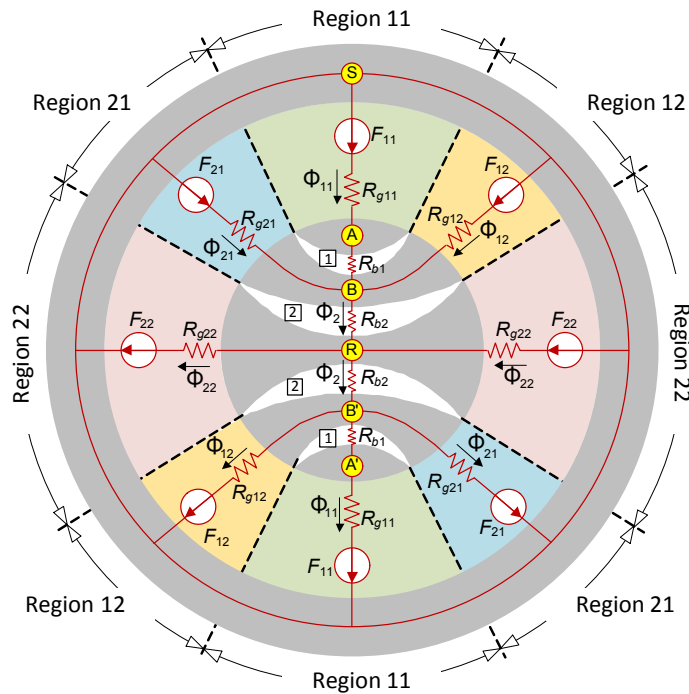


Figure 9.5: Schematic of the SynRel MEC for a two-pole motor with two barriers per pole.

For instance, region "11" is delimited by the end points of barrier 1 (or 1'), regions 12 and 21 are delimited by the end points of barriers 1 and 2 (or 1' and 2'), region "22" is delimited by the end points of barriers 2 and 2'. For the generic air-gap region, the relevant air-gap reluctance (R_g) and MMF (F) is naturally defined and computed as discussed in the next Section. Moreover, the reluctances (R_b) associated to rotor flux barriers are defined and, again, reference is made to the next Section for their analytical computation. The nodes of the MEC are identified as S , A , B , A' , B' , R . Each node represents a portion of the machine (core) where no MMF drop is supposed to occur under the hypothesis (Section 9.1) of disregarding magnetic saturation. The MEC sketched in Fig. 5 can be solved using well-known methods of circuit theory analysis [86]. These give the following solution for the fluxes ϕ_{11} and ϕ_2 passing through barriers 1 and 2:

$$\phi_2 = \frac{F_{eq}}{R_{eq} + R_{b2}} \quad (9.5)$$

$$\phi_{11} = \frac{F_{11} - (F_{eq} - R_{eq} \cdot \phi_2)}{R_{g11} + R_{b1}} \quad (9.6)$$

where:

$$F_{eq}(t, x_r) = \left(\frac{F_{11}}{R_{g11} + R_{b1}} + \frac{F_{12}}{R_{g12}} + \frac{F_{21}}{R_{g21}} \right) \cdot R_{eq} \quad (9.7)$$

$$R_{eq} = \left(\frac{1}{R_{g11} + R_{b1}} + \frac{1}{R_{g12}} + \frac{1}{R_{g21}} \right)^{-1} \quad (9.8)$$

The two fluxes 9.5-9.6 will be used in Section VI to compute machine air-gap flux density distribution.

9.3 Computation of Air-gap MMF Sources

In this Section, the MMF sources of the MEC (e.g. F_{11} , F_{12} , F_{21} , F_{22} in Fig. 9.5) are analytically computed. The computation is based on the analytical expression of the air-gap MMF field produced by a split-phase winding with N three-phase winding sets ([83], Fig. 1). It is assumed that the currents in the w -th three-phase winding ($w=0, 1, \dots, N$) is:

$$i_{p,w}(t) = \sum_{h=1}^{\infty} I_{w,h} \cos \left[h \cdot \left(\omega t - \frac{2\pi \cdot p}{3} - \frac{\pi w}{3N} \right) \right] \quad (9.9)$$

here p is the phase index ranging from 0 to 2 (0 corresponds to phase "A", 1 to phase "B", 2 to phase "C"), h is the time harmonic order, $I_{w,h}$ is the amplitude of the current in the p -th phase of the w -th winding set in regard to the h -th order time harmonic. Calling x the angular position along the air-gap circumference in electrical radians, measured from the symmetry axis of phase "A₀" taken as the zero reference, the air-gap MMF distribution as a function of time (t) and space (x) is [83]:

$$F(t, x) = F^+(t, x) + F^-(t, x) \quad (9.10)$$

where $F^+(t, x)$ and $F^-(t, x)$ are the travelling waves which respectively rotate in the same and opposite sense with respect to the fundamental. They can be written as [83]:

$$F^+(t, x) = \text{Re} \left[\sum_{h,k=1}^{\infty} M_{h,k}^+ \cdot e^{i(h\omega t - kx)} \right], \quad F^-(t, x) = \text{Re} \left[\sum_{h,k=1}^{\infty} M_{h,k}^- \cdot e^{i(h\omega t + kx)} \right] \quad (9.11)$$

where i denotes the imaginary unit, k is the space harmonic order and coefficients $M_{h,k}^+$, $M_{h,k}^-$, are:

$$M_{h,k}^+ = \begin{cases} \frac{6}{\pi} \frac{qnC_k}{k} \sum_{w=0}^{N-1} I_{w,h} e^{-1 \left[\frac{(h-k)\pi w}{3N} \right]} & \text{if } \text{mod}(|h-k|, 3) = 0 \\ 0 & \text{otherwise} \end{cases} \quad (9.12)$$

$$M_{h,k}^- = \begin{cases} \frac{6}{\pi} \frac{qnC_k}{k} \sum_{w=0}^{N-1} I_{w,h} e^{-1 \left[\frac{(h+k)\pi w}{3N} \right]} & \text{if } \text{mod}(|h+k|, 3) = 0 \\ 0 & \text{otherwise} \end{cases} \quad (9.13)$$

In (9.12)-(9.3), q is the number of slots per pole per phase, n the number of series-connected turns per coil and coefficients C_k are defined as:

$$C_k = \sin \left(\frac{\pi k r}{2} \right) \frac{\sin \left(\frac{\alpha_s q k}{2} \right)}{q \sin \left(\frac{\alpha_s k}{2} \right)} \quad (9.14)$$

being $\alpha_s = \pi/(3Nq)$ the slot pitch in electrical radians. From the air-gap MMF distribution function, calling x_r the position (in electrical radians) of the rotor d -axis (taken coincident with flux barrier symmetry axis, Fig. 9.3) with respect to phase "A₀" symmetry axis, we can compute the total MMF that pertain to the various air-gap regions identified in the machine (Fig. 9.5). For instance, in case of two barriers per pole (Fig. 9.5), we have:

$$F_{11}(t, x_r) = \frac{1}{2x_1} \cdot \int_{x_r - x_1}^{x_r + x_1} F(x, t) dx \quad (9.15)$$

$$F_{12}(t, x_r) = \frac{1}{x_2 - x_1} \cdot \int_{x_r + x_1}^{x_r + x_1 + x_2} F(x, t) dx \quad (9.16)$$

$$F_{21}(t, x_r) = \frac{1}{x_2 - x_1} \cdot \int_{x_r - x_1 - x_2}^{x_r - x_1} F(x, t) dx \quad (9.17)$$

where $2x_i$ denotes the length of the rotor outer circumference arc between points P_i and Q_i for the i -th rotor barrier (Fig. 9.4), namely according to Fig. 9.4:

$$x_1 = r\alpha_1 \left(\frac{P}{2} \right), \quad x_1 = r\alpha_1 \left(\frac{P}{2} \right) \quad (9.18)$$

for the two flux barriers ($i=1, i=2$). The coefficient $P/2$ is needed to pass from mechanical radians (α_i) to electrical radians (x_i). From a physical viewpoint, (9.15)-(9.17) represent the average MMF in the three air-gap regions "11", "12", "21". The value of F_{22} is defined in the same way, but it is not worth being computed as it does not appear in the MEC solution for the interesting unknowns ϕ_{11} and ϕ_2 as per (9.6)-(9.8).

9.4 Computation of Air-gap and Barrier Reluctances

The SynRel MEC shown in Fig. 9.5 also includes the reluctances (R_g) associated to the various air-gap regions and the ones (R_b) associated to the flux barriers.

9.4.1 Air-gap reluctances

Taking the example case of a SynRel with two barriers per pole (Fig. 9.3, Fig. 9.5), air-gap reluctances can be trivially computed as follows:

$$R_{g11} = \frac{1}{\mu_0} \cdot \frac{g}{2x_1 \cdot r \cdot L} \cdot p \quad (9.19)$$

$$R_{g12} = R_{g21} = \frac{1}{\mu_0} \cdot \frac{g}{(x_2 - x_1) \cdot r \cdot L} \cdot p \quad (9.20)$$

$$R_{g22} = \frac{1}{\mu_0} \cdot \frac{g}{(\pi - 2x_2) \cdot r \cdot L} \cdot p \quad (9.21)$$

where L is machine core length, r the rotor radius, g is the air-gap width, μ_0 is the magnetic permeability of the air and P is the number of machine poles.

9.4.2 Flux barrier reluctance

While for *C-shaped* flux barriers, with approximately uniform width, the reluctance is easy to compute [21], [9], some complications arise with respect to round or circular-shaped flux barriers (Fig. 9.3, [87], [19], [14]). The detailed mathematical procedure for reluctance computation in this case will be covered in a dedicated publication and is omitted here for the sake of brevity. What is only recalled, for the purpose of this study, is the final expression of the magnetic vector potential in a generic flux barrier and such expression is then used to derive the flux barrier reluctance.

Magnetic vector potential and flux density in the i -th barrier

Let us consider the generic i -th flux barrier domain (Fig. 9.4). To compactly write the vector potential expression inside it, it is convenient to fix a Cartesian reference frame having its origin in point O_i and axes u_i, v_i (Fig. 9.4). In this coordinate system, it is possible to prove that the magnetic vector potential inside the flux barrier can be written in the form:

$$A_{u_i, v_i} = \frac{B_0}{4} \cdot \ln \frac{\left(\frac{\tau_i}{2} + v_i\right)^2 + u_i^2}{\left(\frac{\tau_i}{2} - v_i\right)^2 + u_i^2} + A_0 \quad (9.22)$$

where $\tau_i = \overline{P_i Q_i}$ is given by (9.4), A_0 is an arbitrary additive constant and B_0 is a parameter which depends on the operating point (i.e., in other words, on stator currents and rotor position). The fact that (9.36) is the vector potential inside the i -th flux barrier can be proved by checking that it satisfies Laplace differential equation in the inner points of the flux barrier and the Neumann boundary conditions on the borders [88]. More precisely, Laplace equation

$$\frac{\partial^2 A(u_i, v_i)}{\partial^2 u_i} + \frac{\partial^2 A(u_i, v_i)}{\partial^2 v_i} = 0 \quad (9.23)$$

can be proved to hold by directly substituting the partial derivatives of (9.36) into (9.23). The flux density can be consequently derived as [88]:

$$\begin{aligned} \mathbf{B}(u_i, v_i) &= \begin{pmatrix} B_{ui}(u_i, v_i) \\ B_{vi}(u_i, v_i) \end{pmatrix} = \begin{pmatrix} -\partial A(u_i, v_i)/\partial v_i \\ \partial A(u_i, v_i)/\partial u_i \end{pmatrix} \\ &= \frac{B_0 \tau_i / 2}{\left[(\tau_i / 2 + v_i)^2 + u_i^2 \right] \left[(\tau_i / 2 + v_i)^2 + u_i^2 \right]} \cdot \begin{pmatrix} v_i^2 - u_i^2 - (\tau_i / 2)^2 \\ 2u_i v_i \end{pmatrix} \end{aligned} \quad (9.24)$$

As regards boundary conditions, we can observe that the barrier borders are arcs of circumferences Γ_{ai} and Γ_{bi} whose Cartesian equations in the $u_i O_i v_i$ reference frame are:

$$\Gamma_{ai}: \quad (u_i + d_{ai})^2 + v_i^2 = r_{ai}^2 \quad (9.25)$$

$$\Gamma_{bi}: \quad (u_i + d_{bi})^2 + v_i^2 = r_{bi}^2 \quad (9.26)$$

where

$$d_{ai} = \sqrt{r_{ai}^2 - (\tau_i / 2)^2} \quad , \quad d_{bi} = \sqrt{r_{bi}^2 - (\tau_i / 2)^2} \quad (9.27)$$

which geometrical meaning is given in Fig. 9.4.

Hence, the tangent vectors (\mathbf{t}_{ai} and \mathbf{t}_{bi}) to the two circumferences Γ_{ai} and Γ_{bi} in a point of abscissa u_i are easily found to be:

$$\mathbf{t}_{ai}(u_i) = \begin{pmatrix} \pm 1 & - \frac{d_{ai} + u_i}{\sqrt{r_{ai}^2 - (d_{ai} + u_i)^2}} \end{pmatrix}^t \quad (9.28)$$

$$\mathbf{t}_{bi}(u_i) = \begin{pmatrix} \pm 1 & - \frac{d_{bi} + u_i}{\sqrt{r_{bi}^2 - (d_{bi} + u_i)^2}} \end{pmatrix}^t \quad (9.29)$$

Newmann boundary conditions can be written in the form:

$$\mathbf{t}_{ai}(u_i) \bullet \mathbf{B}(u_i, v_i) = 0 \quad \text{on} \quad \Gamma_{ai} \quad (9.30)$$

$$\mathbf{t}_{bi}(u_i) \bullet \mathbf{B}(u_i, v_i) = 0 \quad \text{on} \quad \Gamma_{bi} \quad (9.31)$$

meaning that the flux density is anywhere orthogonal to the flux barrier border. Actually, (9.30) can be easily checked to hold for all (u_i, v_i) pairs satisfying (9.25) and (9.31) to hold for all (u_i, v_i) pairs satisfying (9.26).

Reluctance calculation for the i -th flux barrier

Once the field inside the i -th flux barrier is known, its reluctance R_{bi} can be computed from Hopkinson law as:

$$R_{bi}(u_i) = \frac{\Delta H_{barr}}{\phi_{barr}} \quad (9.32)$$

where ϕ_{barr} is the flux crossing the barrier and ΔH_{barr} is the MMF drop across it. ϕ_{barr} can be computed directly using the vector potential (9.36) as [88]:

$$\phi_{barr} = L \left[A(u_{Pai}, v_{Pai}) - A(u_{Qai}, v_{Qai}) \right] \quad (9.33)$$

where (u_{Pai}, v_{Pai}) and (u_{Qai}, v_{Qai}) are the coordinates of flux barrier end points P_{ai} , Q_{ai} (Fig. 9.4). From the inspection of Fig. 9.4 we have:

$$v_{Pai} = -v_{Qai} = r \cdot \sin \alpha_{a1} \quad (9.34)$$

and by substitution of (9.34) into (9.25) we have:

$$v_{Pai} = v_{Qai} = \sqrt{r_{ai}^2 - r^2 \cdot \sin^2 \alpha_{a1}} - d_{ai} \quad (9.35)$$

By using (9.36) we can derive an explicit analytical expression for ϕ_{barr} :

$$\phi_{barr} = L \frac{B_0}{2} \cdot \ln \frac{\left(\frac{\tau_i}{2} + r \cdot \sin \alpha_{a1} \right)^2 + \left(\sqrt{r_{ai}^2 - r^2 \cdot \sin^2 \alpha_{a1}} - d_{ai} \right)^2}{\left(\frac{\tau_i}{2} - r \cdot \sin \alpha_{a1} \right)^2 + \left(\sqrt{r_{ai}^2 - r^2 \cdot \sin^2 \alpha_{a1}} - d_{ai} \right)^2} \quad (9.36)$$

The MMF drop ΔH_{barr} across the flux barrier can be computed by integration of the magnetic field (9.24) along a path that goes from one to the other border of the flux barrier. For instance, taking a linear path along the barrier axis of symmetry, we have:

$$\Delta H_{barr} = \frac{1}{\mu_0} \cdot \int_{r_{ai}-d_{ai}}^{r_{bi}-d_{bi}} F(x, t) dx \quad (9.37)$$

Using (9.24) and performing the integral symbolically, this yields:

$$\Delta H_{barr} = \frac{B_0}{\mu_0} \left[\arctan \left(\frac{2(r_{b1} - d_{b1})}{\tau_i} \right) - \left(\frac{2(r_{a1} - d_{a1})}{\tau_i} \right) \right] \quad (9.38)$$

$$R_{bi} = \frac{2 \cdot \left[\arctan \left(\frac{2(r_{b1} - d_{b1})}{\tau_i} \right) - \left(\frac{2(r_{a1} - d_{a1})}{\tau_i} \right) \right]}{L \mu_0 \cdot \ln \frac{\left(\frac{\tau_i}{2} + r \cdot \sin \alpha_{a1} \right)^2 + \left(\sqrt{r_{ai}^2 - r^2 \cdot \sin^2 \alpha_{a1}} - d_{ai} \right)^2}{\left(\frac{\tau_i}{2} - r \cdot \sin \alpha_{a1} \right)^2 + \left(\sqrt{r_{ai}^2 - r^2 \cdot \sin^2 \alpha_{a1}} - d_{ai} \right)^2}} \quad (9.39)$$

We can observe that the analytical expression (9.39) for the reluctance of the i -th flux barrier does not depend on the operating point [parameter B_0 in (9.36) cancel out] and only depends on the barrier geometry and machine core length L .

9.5 Computation of Air-gap Flux

Once the MEC of the SynRel motor has been evaluated and solved (Section III-V), the solution can be used to compute the air-gap flux density distribution in the machine. For this purpose, it is necessary to correct the MMF due to stator currents (Section IV) by adding or subtracting the MMF drops due to the flux flowing across rotor barriers. In particular, in the case of two barriers per pole, the following two MMF drops are to be computed:

$$\Delta F_{11} = \phi_{11}R_{b1} + \phi_2R_{b2} \quad (9.40)$$

$$\Delta F_{12} = \phi_2R_{b2} \quad (9.41)$$

The former contribution is to be applied to region "11" and accounts for the MMF drop due to the flux passing through both barriers 1 and 2. The contribution (9.41) instead, applies to the regions "12" and "21" and accounts for the MMF due to the flux passing across barrier 2 only. Finally, no correction to stator current MMF is to be applied in region "22" because all the flux flowing in such region does not cross any rotor barrier. The total MMF (including stator current contribution and MMF drops through rotor barriers) can be written in the form given in (??) at the bottom of the page. Since (??) represents a total (resultant) MMF acting in the air-gap, the flux density immediately derives from it as:

$$B_{tot}(t, x, x_r) = \frac{\mu_0}{g} \cdot F_{tot}(t, x, x_r) \quad (9.42)$$

$$F_{tot}(t, x, x_r) = \begin{cases} F(t, x) - \Delta F_{11}(t, x_r) & \text{if } \begin{aligned} &0 \leq |\text{mod}(x - x_r, 2\pi)| \leq x_1 \\ &\vee \quad 2\pi - x_1 \leq |\text{mod}(x - x_r, 2\pi)| \leq 2\pi \end{aligned} \\ F(t, x) + \Delta F_{11}(t, x_r) & \text{if } \pi - x_1 \leq |\text{mod}(x - x_r, 2\pi)| \leq \pi + x_1 \\ F(t, x) - \Delta F_{12}(t, x_r) & \text{if } \begin{aligned} &x_1 \leq |\text{mod}(x - x_r, 2\pi)| \leq x_2 \\ &\vee \quad 2\pi - x_2 \leq |\text{mod}(x - x_r, 2\pi)| \leq 2\pi - x_1 \end{aligned} \\ F(t, x) + \Delta F_{12}(t, x_r) & \text{if } \begin{aligned} &x_1 + \pi \leq |\text{mod}(x - x_r, 2\pi)| \leq x_2 + \pi \\ &\vee \quad \pi - x_2 \leq |\text{mod}(x - x_r, 2\pi)| \leq \pi - x_1 \end{aligned} \\ F(t, x) & \text{otherwise} \end{cases} \quad (9.43)$$

9.6 Assessment Against FEA Simulation

The methodology proposed in this chapter is next applied to the four-pole dual-three-phase SynRel motor whose cross section is shown in Fig. 9.3. Its characteristic data

Table 9.1: Characteristic Data of the example SynRel Machine.

Name	Symbol	Value	Unit
Stator bore radius	D_s	30	mm
Air gap width	g	0.3	mm
Number of stator slots	Z	24	–
Number of poles	$2p$	4	–
Number of conductors per slots	N_s	20	–
Slot opening width	τ_s	2	mm
Tooth width at the air gap	τ_t	5.8	mm
Angle x_1 (8.6)	x_1	21.4	mech deg
Angle x_2 (8.6)	x_2	34.2	mech deg
1-st flux barrier width (8.6)	h_1	2.5	mm
2-st flux barrier width (8.6)	h_2	3.0	mm
Stack lenght	L	50	mm

are provided in Table 9.1. Stator and rotor cores are characterized by a ferromagnetic material having an ordinary BH curve with a saturation knee located at around $H=15.000 A/m$ and $B=1.65 T$. As a first study case, both machine windings are energized with a peak current of 50 A taking its maximum value in phase A_0 . The currents in the other phases are set according to (9) taking the instant $t = 0$ and setting all current harmonics different from the fundamental to zero ($I_{w,h}=0$ for $h(??)$). For such a current distribution, the rotor is placed at different positions x_r with respect to phase A_0 axis and, for each position, a FEA simulation is run (Fig. 6a). The resulting air-gap field is then plotted and compared to that obtained analytically from (41) where $t = 0$. The comparisons for $x_r=0^\circ$, $x_r=15^\circ$, $x_r=30^\circ$ and $x_r=60^\circ$ electrical degrees are shown in Fig. 7, showing an excellent agreement with analytical predictions. As a second study case, one of the two winding sets is again energized with a 50 A current (the maximum current value being in phase A_0), while the other set is at no load [$I_w, h=50$ for $h = 1$ and $w = 0$, while $I_{w,h}=0$ for any other w and h in (9)]. FEA simulations are also run in this case for different rotor positions (Fig. 6b). The air-gap flux density obtained from FEA is then compared to the analytical prediction, as depicted in Fig. 8, showing a very good agreement.

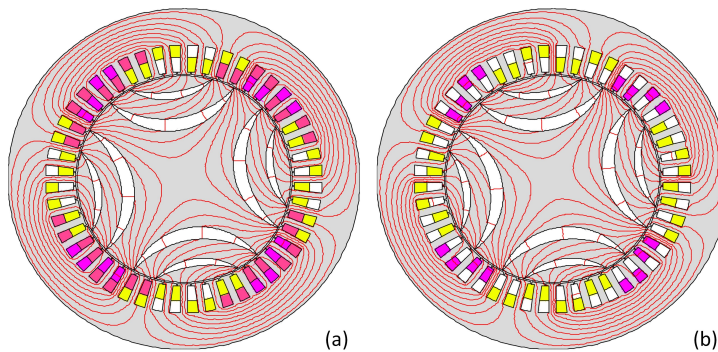


Figure 9.6: FEA simulation output for rotor position $x_r=15^\circ$ and for (a) both winding sets energized; (b) only one winding set energized.

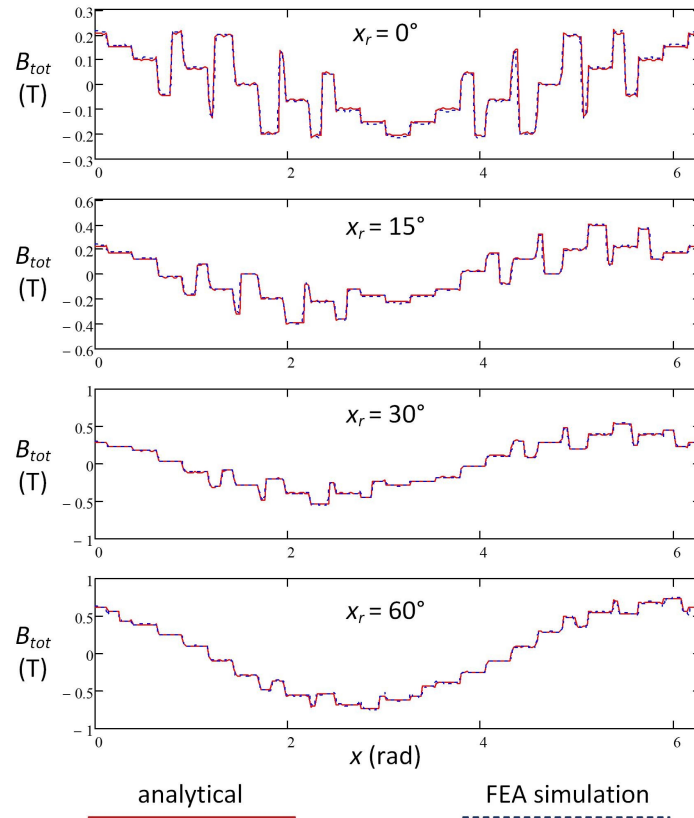


Figure 9.7: Air-gap flux density over a pole span, computed analytically and by FEA simulation for both windings energized with 50 A current.

9.7 Conclusions

SynRel motors with split-phase stator winding sets supplied by multiple inverters have been investigated in this chapter as an increasingly attractive solution for fault-tolerant, rugged, magnet-free vehicle traction drives. These machines are typically designed through iterative optimization techniques in which thousands of alternatives are evaluated in search for an optimum. This calls for very fast computation approaches to keep optimization procedures within acceptable time frames. In response to such a need, this work has proposed an analytical method for the air-gap computation of split-phase SynRel motors equipped with an arbitrary number of stator three-phase sets and with circular-shaped rotor barriers. The MEC model of the motor has been first defined and analytical procedures have been presented to compute its parameters. The flux density distribution in the air-gap has been then derived based on MEC solution. The

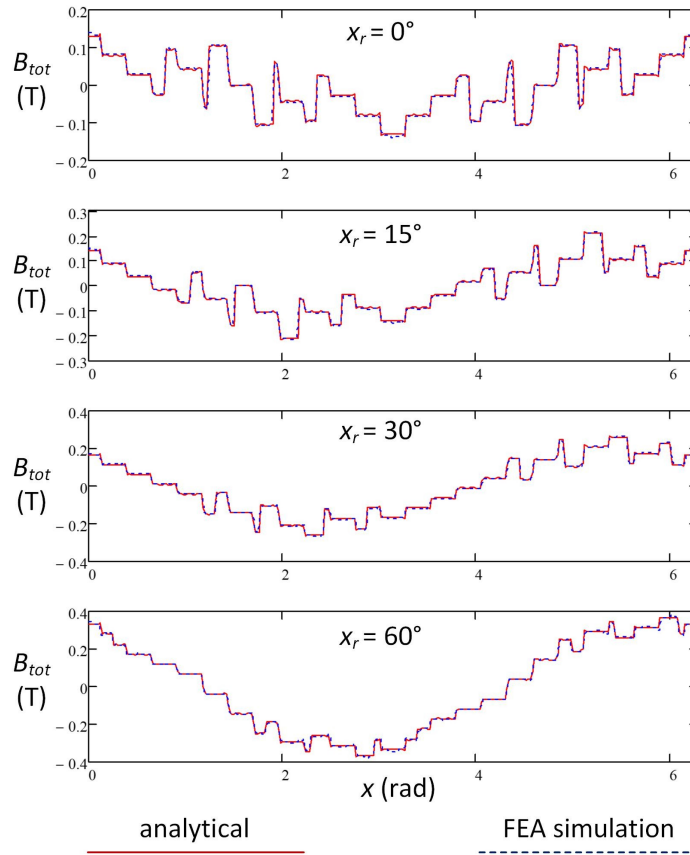


Figure 9.8: Air-gap flux density over a pole span, computed analytically and by FEA simulation for unbalanced SynRel motor operation (one winding energized with 50 A current, the other at no load).

accuracy of the proposed methodology has been assessed against FEA simulations (including magnetic saturation) showing a very good agreement between numerical and analytical predictions. This suggests that the proposed approach can be a fast, accurate and reliable alternative to time-consuming FEA simulations for the analysis of the electric machine topology under study. Future investigations, presently in progress or in publication, will address the extensions of the presented model for electromagnetic torque computation and for machine transient analysis and operation with arbitrary (non-sinusoidal) current waveforms.

Part III

**Prototypes and Experimental
Results**

References

- [1] J. Kostko, "Polyphase reaction synchronous motors," *American Institute of Electrical Engineers, Journal of the*, vol. 42, no. 11, pp. 1162–1168, Nov 1923. [13](#), [14](#), [105](#)
- [2] A. Vagati, "The synchronous reluctance solution: a new alternative in ac drives," in *Industrial Electronics, Control and Instrumentation, 1994. IECON '94., 20th International Conference on*, vol. 1, Sep 1994, pp. 1–13 vol.1. [13](#)
- [3] T. Matsuo, A. El-Antably, and T. Lipo, "A new control strategy for optimum-efficiency operation of a synchronous reluctance motor," *Industry Applications, IEEE Transactions on*, vol. 33, no. 5, pp. 1146–1153, Sep 1997. [13](#), [14](#)
- [4] Y. C. Choi, H.-S. Kim, and J.-H. Lee, "Optimum design criteria for maximum torque density and minimum torque ripple of synrm according to the rated wattage using response surface methodology," *Magnetics, IEEE Transactions on*, vol. 44, no. 11, pp. 4135–4138, Nov 2008. [13](#), [14](#)
- [5] J. M. Park, S. I. Kim, J.-P. Hong, and J.-H. Lee, "Rotor design on torque ripple reduction for a synchronous reluctance motor with concentrated winding using response surface methodology," *Magnetics, IEEE Transactions on*, vol. 42, no. 10, pp. 3479–3481, Oct 2006. [13](#)
- [6] M. Sanada, K. Hiramoto, S. Morimoto, and Y. Takeda, "Torque ripple improvement for synchronous reluctance motor using asymmetric flux barrier arrangement," in *Conference Record of the 38th IAS Annual Meeting*, vol. 1, Oct 2003, pp. 250–255 vol.1. [13](#)
- [7] S. Zhao, O. Wallmark, and M. Leksell, "Low-speed sensorless control with reduced copper losses for saturated pmsynrel machines," *Energy Conversion, IEEE Transactions on*, vol. 28, no. 4, pp. 841–848, Dec 2013. [13](#), [14](#)
- [8] M. Barcaro, N. Bianchi, and F. Magnussen, "Rotor flux-barrier geometry design to reduce stator iron losses in synchronous ipm motors under fw operations," *Industry Applications, IEEE Transactions on*, vol. 46, no. 5, pp. 1950–1958, Sept 2010. [13](#), [14](#)
- [9] M. Barcaro and N. Bianchi, "Air-gap flux density distortion and iron losses in anisotropic synchronous motors," *Magnetics, IEEE Transactions on*, vol. 46, no. 1, pp. 121–126, Jan 2010. [13](#), [94](#), [106](#), [107](#), [109](#), [112](#)

- [10] S. Yamamoto, H. Hirahara, J. Adawey, T. Ara, and K. Matsuse, "Maximum efficiency drives of synchronous reluctance motors by a novel loss minimization controller with inductance estimator," *Industry Applications, IEEE Transactions on*, vol. 49, no. 6, pp. 2543–2551, Nov 2013. [13](#), [14](#)
- [11] S. Taghavi and P. Pillay, "A sizing methodology of the synchronous reluctance motor for traction applications," *Emerging and Selected Topics in Power Electronics, IEEE Journal of*, vol. 2, no. 2, pp. 329–340, June 2014. [13](#), [14](#), [105](#)
- [12] A. Arkadan, N. Al-Aawar, and A. Hanbali, "Design optimization of synrm drives for hev power train applications," in *Electric Machines Drives Conference, 2007. IEMDC '07. IEEE International*, vol. 1, May 2007, pp. 810–814. [13](#), [105](#)
- [13] H. Nam, S. Park, G. Kang, J. Hong, J. Eom, and T. Jung, "Design to improve starting performance of line-start synchronous reluctance motor for household appliances," in *Industry Applications Conference, 2004. 39th IAS Annual Meeting. Conference Record of the 2004 IEEE*, vol. 1, Oct 2004, pp. –85. [13](#)
- [14] H. Kiriya, S. Kawano, Y. Honda, T. Higaki, S. Morimoto, and Y. Takeda, "High performance synchronous reluctance motor with multi-flux barrier for the appliance industry," in *Industry Applications Conference, 1998. Thirty-Third IAS Annual Meeting. The 1998 IEEE*, vol. 1, Oct 1998, pp. 111–117 vol.1. [13](#), [14](#), [107](#), [112](#)
- [15] P. Niazi, H. Toliyat, D.-H. Cheong, and J.-C. Kim, "A low-cost and efficient permanent-magnet-assisted synchronous reluctance motor drive," *Industry Applications, IEEE Transactions on*, vol. 43, no. 2, pp. 542–550, March 2007. [13](#), [14](#), [105](#), [106](#)
- [16] Y.-H. Im, S.-I. Hwang, S.-M. Jang, J.-Y. Choi, and J.-H. Choi, "Analysis of torque pulsation considering interior permanent magnet rotor rib shape using response surface methodology," *Magnetics, IEEE Transactions on*, vol. 48, no. 2, pp. 979–982, Feb 2012. [13](#)
- [17] J. Wang, V. Patel, and W. Wang, "Fractional-slot permanent magnet brushless machines with low space harmonic contents," *Magnetics, IEEE Transactions on*, vol. 50, no. 1, pp. 1–9, Jan 2014. [13](#), [14](#)
- [18] M. Barcaro and N. Bianchi, "Interior PM machines using ferrite to substitute rare-earth surface pm machines," in *20th International Conference on Electrical Machines (ICEM)*, 2012, pp. 1339–1345. [13](#), [15](#), [33](#), [55](#), [68](#)
- [19] G. Pellegrino, F. Cupertino, and C. Gerada, "Barriers shapes and minimum set of rotor parameters in the automated design of synchronous reluctance machines," in *Electric Machines Drives Conference (IEMDC), 2013 IEEE International*, May 2013, pp. 1204–1210. [14](#), [94](#), [106](#), [107](#), [112](#)
- [20] R.-R. Moghaddam and F. Gyllensten, "Novel high-performance synrm design method: An easy approach for a complicated rotor topology," *Industrial Electronics, IEEE Transactions on*, vol. 61, no. 9, pp. 5058–5065, Sept 2014. [14](#)

- [21] N. Bianchi, S. Bolognani, D. Bon, and M. Pre?, “Rotor flux-barrier design for torque ripple reduction in synchronous reluctance and pm-assisted synchronous reluctance motors,” *Industry Applications, IEEE Transactions on*, vol. 45, no. 3, pp. 921–928, May 2009. [14](#), [33](#), [40](#), [94](#), [106](#), [107](#), [109](#), [112](#)
- [22] A. V. A. Fratta and F. Villata, “Permanent magnet assisted synchronous reluctance drive for constant-power application: Drive power limit.” ser. Proc. of Intelligent Motion European Conference, PCIM, Nurnberg, Germany, April 1992, pp. 196–203. [15](#)
- [23] W.-H. Kim, K.-S. Kim, S.-J. Kim, D.-W. Kang, S.-C. Go, Y.-D. Chun, and J. Lee, “Optimal pm design of pma-synrm for wide constant-power operation and torque ripple reduction,” *Magnetics, IEEE Transactions on*, vol. 45, no. 10, pp. 4660–4663, Oct 2009. [15](#)
- [24] A. Vagati, B. Boazzo, P. Guglielmi, and G. Pellegrino, “Ferrite assisted synchronous reluctance machines: A general approach,” in *20th International Conference on Electrical Machines (ICEM)*, 2012, pp. 1315–1321. [15](#), [55](#), [68](#)
- [25] A. Fratta, G. Troglia, A. Vagati, and F. Villata, “Evaluation of torque ripple in high performance synchronous reluctance machines,” in *Conference Record of the IEEE Industry Applications Society Annual Meeting*, 1993, pp. 163–170 vol.1. [15](#), [39](#), [55](#), [67](#)
- [26] N. Bianchi, *Permanent Magnet Synchronous Motors*, ser. Industrial Electronics Handbook, Power Electronics and Motor Drives. 2nd edition, CNC Press, 2011, no. Chapt. 6, 2011. [15](#), [33](#)
- [27] A. Vagati, M. Pastorelli, G. Francheschini, and S. Petrache, “Design of low-torque-ripple synchronous reluctance motors,” *IEEE Transactions on Industry Applications*, vol. 34, no. 4, pp. 758–765, 1998. [15](#), [33](#), [40](#), [55](#), [68](#)
- [28] M. Morandin, “Electric drives with permanent magnet synchronous machines connected to internal combustion engines,” Ph.D. dissertation, Ph.D. School in Electrical Engineering, University of Padova, 31 July 2013. [Online]. Available: <http://paduaresearch.cab.unipd.it> [19](#)
- [29] E. Carraro, M. Degano, M. Morandin, and N. Bianchi, “Formula SAE electric competition: Electrical motor design,” in *IEEE International Electric Machines Drives Conference (IEMDC)*, May 2013, pp. 1142–1148. [21](#), [68](#)
- [30] M. Morandin, S. Bolognani, R. Petrella, A. Pevere, and S. Calligaro, “Mild-hybrid traction system based on a bidirectional half-bridge interleaved converter and a three-level active npc inverter-fed pmsm,” in *Applied Power Electronics Conference and Exposition (APEC), 2012 Twenty-Seventh Annual IEEE*, Feb 2012, pp. 1644–1651. [22](#)
- [31] A. Fratta, P. Guglielmi, F. Villata, and A. Vagati, “Efficiency and cost-effectiveness of ac drives for electric vehicles improved by a novel, boost dc-dc conversion structure,” in *Power Electronics in Transportation, 1998*, Oct 1998, pp. 11–19. [22](#)

- [32] J. Tangudu and T. Jahns, "Comparison of interior PM machines with concentrated and distributed stator windings for traction applications," in *IEEE Vehicle Power and Propulsion Conference (VPPC)*, 2011, pp. 1–8. **23, 33, 42, 67, 68, 82**
- [33] L. Chong and M. Rahman, "Saliency ratio derivation and optimisation for an interior permanent magnet machine with concentrated windings using finite-element analysis," *IET Electric Power Applications*, vol. 4, no. 4, pp. 249–258, April 2010. **23, 33, 42, 68, 82**
- [34] W. Soong and T. J. E. Miller, "Field-weakening performance of brushless synchronous ac motor drives," *IEE Proceedings Electric Power Applications*, vol. 141, no. 6, pp. 331–340, Nov 1994. **26, 36, 70, 72**
- [35] airgp4066d1 IGBT, International Rectifier, www.irf.com/product-info/datasheets/data/airgp4066d1.pdf, September 2012. **28**
- [36] N. Mohan, T. Undeland, and W. Robbins, *Power Electronics: Converters, Applications, and Design*, 3rd ed., W. John and Sons, Eds., 2003. **28, 76**
- [37] M. Morandin, M. Ferrari, and S. Bolognani, "Power-train design and performance of a hybrid motorcycle prototype," *IEEE Transactions on Industry Applications*, vol. PP, no. 99, pp. 1–1, 2014. **30, 76**
- [38] E. Carraro, M. Degano, and N. Bianchi, "Permanent magnet volume minimization in permanent magnet assisted synchronous reluctance motors," in *Ecological Vehicles and Renewable Energies (EVER), 2013 8th International Conference and Exhibition on*, March 2013, pp. 1–4. **33, 52**
- [39] J. Tangudu, T. Jahns, and A. El-Refaie, "Unsaturated and saturated saliency trends in fractional-slot concentrated-winding interior permanent magnet machines," in *Energy Conversion Congress and Exposition (ECCE), 2010 IEEE*, Sept 2010, pp. 1082–1089. **33**
- [40] M. Degano, N. Bianchi, and E. Fornasiero, "Sensitivity analysis of torque ripple reduction of synchronous reluctance and interior pm motors," *Industry Applications, IEEE Transactions on*, vol. PP, no. 99, pp. 1–1, 2014. **39, 58, 60, 93**
- [41] T. Jahns and W. Soong, "Pulsating torque minimization techniques for permanent magnet ac motor drives-a review," *Industrial Electronics, IEEE Transactions on*, vol. 43, no. 2, pp. 321–330, Apr 1996. **40**
- [42] S.-H. Han, T. Jahns, W. Soong, M. Guven, and M. Illindala, "Torque ripple reduction in interior permanent magnet synchronous machines using stators with odd number of slots per pole pair," *Energy Conversion, IEEE Transactions on*, vol. 25, no. 1, pp. 118–127, March 2010. **40**
- [43] N. Bianchi and S. Bolognani, "Reducing torque ripple in pm synchronous motor by pole shifting," in *Proceedings of International Conference on Electrical Machines (ICEM)*, 2000. **40**

- [44] M. Sanada, K. Hiramoto, S. Morimoto, and Y. Takeda, "Torque ripple improvement for synchronous reluctance motor using an asymmetric flux barrier arrangement," *Industry Applications, IEEE Transactions on*, vol. 40, no. 4, pp. 1076–1082, July 2004. 40
- [45] T. Li and G. Slemon, "Reduction of cogging torque in permanent magnet motors," *IEEE Transactions on Magnetics*, vol. 24, no. 6, pp. 2901–2903, Nov 1988. 40
- [46] P. D. Barba, *Multiobjective Shape Design in Electricity and Magnetism*, ser. Lecture Notes in Electrical Engineering. Springer, 2010, vol. 47. 51
- [47] P. Lazari, J. Wang, and L. Chen, "A computationally efficient design technique for electric vehicle traction machines," *IEEE Transactions on Industry Applications*, vol. PP, no. 99, pp. 1–1, 2014. 55
- [48] L. Chen, J. Wang, P. Lombard, P. Lazari, and V. Leconte, "Design optimisation of permanent magnet assisted synchronous reluctance machines for electric vehicle applications," in *20th International Conference on Electrical Machines (ICEM)*, Sept 2012, pp. 2647–2653. 55
- [49] L. Chen, J. Wang, P. Lazari, and X. Chen, "Optimizations of a permanent magnet machine targeting different driving cycles for electric vehicles," in *IEEE International Electric Machines Drives Conference (IEMDC)*, May 2013, pp. 855–862. 55
- [50] E. Carraro, M. Morandini, and N. Bianchi, "Optimization of a traction PMSM motor according to a given driving cycle," in *IEEE Transportation Electrification Conference and Exposition (ITEC)*, 2014. 55, 73
- [51] E. Armando, P. Guglielmi, M. Pastorelli, G. Pellegrino, and A. Vagati, "Performance of IPM-PMSM motors with ferrite injection for home appliance washing machine," in *IEEE Industry Applications Society Annual Meeting (IAS)*, 2008, pp. 1–6. 55
- [52] S. Chino, S. Ogasawara, T. Miura, A. Chiba, M. Takemoto, and N. Hoshi, "Fundamental characteristics of a ferrite permanent magnet axial gap motor with segmented rotor structure for the hybrid electric vehicle," in *IEEE Energy Conversion Congress and Exposition (ECCE)*, 2011, pp. 2805–2811. 55
- [53] N. Bianchi, *Industrial Electronics Handbooks, Power Electronics and Motor Drives, 2nd edition*. CRC Press, 2011, ch. Permanent Magnet Synchronous Motors, pp. 6.1–6.35. 55, 67, 68
- [54] M. Degano, E. Carraro, and N. Bianchi, "Robust optimization of a traction pmsm motor according to given driving cycles," in *Electrical Machines (ICEM), 2014 International Conference on*, Sept 2014, pp. 270–276. 56
- [55] United States Environmental Protection Agency (USEPA). [Online]. Available: <http://www.epa.gov/nvfel/testing/dynamometer.htm> 56

- [56] M. Ehsani, Y. Gao, and A. Emadi, *Modern electric, hybrid electric, and fuel cell vehicles : fundamentals, theory, and design*. CRC Press, 2010, ch. Fundamentals of Vehicle Propulsion and Brake, Ch. 2, pp. 21–65. 56
- [57] M. Ferrari, N. Bianchi, and E. Fornasiero, “Rotor saturation impact in synchronous reluctance and PM assisted reluctance motors,” in *IEEE Energy Conversion Congress and Exposition (ECCE)*, 2013, pp. 1235–1242. 57, 58, 60
- [58] S. Brisset, F. Gillon, S. Vivier, and P. Brochet, “Optimization with experimental design: an approach using Taguchi’s methodology and finite element simulations,” *IEEE Transactions on Magnetics*, vol. 37, no. 5, pp. 3530–3533, Sep 2001. 58
- [59] A. Omekanda, “Robust torque and torque-per-inertia optimization of a switched reluctance motor using the Taguchi methods,” *IEEE Transactions on Industry Applications*, vol. 42, no. 2, pp. 473–478, March 2006. 58
- [60] T. Jahns, “Flux-weakening regime operation of an interior permanent-magnet synchronous motor drive,” *IEEE Transactions on Industry Applications*, vol. IA-23, no. 4, pp. 681–689, 1987. 62, 70
- [61] W. Soong, P. Reddy, A. El-Refaie, T. Jahns, and N. Ertugrul, “Surface pm machine parameter selection for wide field-weakening applications,” in *42nd IAS Annual Meeting Conference Record of the IEEE Industry Applications Conference, 2007.*, Sept 2007, pp. 882–889. 67
- [62] P. Reddy, T. Jahns, P. McCleer, and T. Bohn, “Design, analysis and fabrication of a high-performance fractional-slot concentrated winding surface PM machine,” in *IEEE Energy Conversion Congress and Exposition (ECCE)*, 2010, pp. 1074–1081. 67
- [63] P. Reddy, A. EL-Refaie, K.-K. Huh, J. Tangudu, and T. Jahns, “Comparison of interior and surface PM machines equipped with fractional-slot concentrated windings for hybrid traction applications,” *IEEE Transactions on Energy Conversion*, vol. 27, no. 3, pp. 593–602, 2012. 67
- [64] J. Tangudu, T. Jahns, and T. Bohn, “Design, analysis and loss minimization of a fractional-slot concentrated winding IPM machine for traction applications,” in *IEEE Energy Conversion Congress and Exposition (ECCE)*, 2011, pp. 2236–2243. 67
- [65] A. El-Refaie, J. Alexander, S. Galioto, P. Reddy, K.-K. Huh, P. de Bock, and X. Shen, “Advanced high-power-density interior permanent magnet motor for traction applications,” *IEEE Transactions on Industry Applications*, vol. 50, no. 5, pp. 3235–3248, Sept 2014. 67
- [66] E. Carraro and N. Bianchi, “Design and comparison of interior permanent magnet synchronous motors with non-uniform airgap and conventional rotor for electric vehicle applications,” *IET Electric Power Applications*, vol. 8, no. 6, pp. 240–249, July 2014. 67

- [67] J. Malan and M. Kamper, "Performance of a hybrid electric vehicle using reluctance synchronous machine technology," *IEEE Transactions on Industry Applications*, vol. 37, no. 5, pp. 1319–1324, Sep 2001. 67
- [68] M. Barcaro and N. Bianchi, "Torque components in integral- and fractional-slot ipm machines," in *IEEE International Electric Machines Drives Conference (IEMDC)*, May 2011, pp. 1340–1345. 68
- [69] M. Ferrari, N. Bianchi, and E. Fornasiero, "Analysis of rotor saturation in synchronous reluctance and pm assisted reluctance motors," *IEEE Transactions on Industry Applications*, vol. PP, no. 99, pp. 1–1, 2014. 69
- [70] B. Sneyers, D. Novotny, and T. Lipo, "Field weakening in buried permanent magnet ac motor drives," *IEEE Transactions on Industry Applications*, vol. IA-21, no. 2, pp. 398–407, 1985. 70
- [71] A. EL-Refaie and T. Jahns, "Optimal flux weakening in surface PM machines using fractional-slot concentrated windings," *IEEE Transactions on Industry Applications*, vol. 41, no. 3, pp. 790–800, 2005. 72
- [72] A. De Almeida, F. Ferreira, and G. Baoming, "Beyond induction motors 2014; technology trends to move up efficiency," in *Industrial Commercial Power Systems Technical Conf (I CPS), 2013 IEEE/IAS 49th*, April 2013, pp. 1–13. 80
- [73] A. De Almeida, F. Ferreira, and A. Quintino Duarte, "Technical and economical considerations on super high-efficiency three-phase motors," *Industry Applications, IEEE Transactions on*, vol. 50, no. 2, pp. 1274–1285, March 2014. 80
- [74] R. Tuncay, M. Yilmaz, and C. Onculoglu, "The design methodology to develop new-generation universal-motors for vacuum cleaners," in *Electric Machines and Drives Conference, 2001. IEMDC 2001. IEEE International*, 2001, pp. 926–930. 80
- [75] G. Papa, B. Korousic-Seljak, B. Benedicic, and T. Kmecl, "Universal motor efficiency improvement using evolutionary optimization," *Industrial Electronics, IEEE Transactions on*, vol. 50, no. 3, pp. 602–611, June 2003. 80
- [76] A. Boglietti, A. Cavagnino, M. Pastorelli, and A. Vagati, "Experimental comparison of induction and synchronous reluctance motors performance," in *Industry Applications Conference, 2005. Fourtieth IAS Annual Meeting. Conference Record of the 2005*, vol. 1, Oct 2005, pp. 474–479 Vol. 1. 93
- [77] E. Rashad, T. Radwan, and M. Rahman, "A maximum torque per ampere vector control strategy for synchronous reluctance motors considering saturation and iron losses," in *Industry Applications Conference, 2004. 39th IAS Annual Meeting. Conference Record of the 2004 IEEE*, vol. 4, Oct 2004, pp. 2411–2417 vol.4. 93
- [78] R. Moghaddam, F. Magnussen, and C. Sadarangani, "Novel rotor design optimization of synchronous reluctance machine for high torque density," in *Power Electronics, Machines and Drives (PEMD 2012), 6th IET International Conference on*, March 2012, pp. 1–4. 93

- [79] N. Bianchi, S. Bolognani, D. Bon, and M. Dai Pre, “Torque harmonic compensation in a synchronous reluctance motor,” *Energy Conversion, IEEE Transactions on*, vol. 23, no. 2, pp. 466–473, June 2008. [94](#)
- [80] M. Ferrari, N. Bianchi, A. Doria, and E. Fornasiero, “Design of synchronous reluctance motor for hybrid electric vehicles,” in *Electric Machines Drives Conference (IEMDC), 2013 IEEE International*, May 2013, pp. 1058–1065. [94](#)
- [81] A. Tessarolo, “Accurate computation of multiphase synchronous machine inductances based on winding function theory,” *Energy Conversion, IEEE Transactions on*, vol. 27, no. 4, pp. 895–904, Dec 2012. [95](#)
- [82] A. Tessarolo, M. Mezzarobba, and M. Degano, “Analytical calculation of air-gap armature reaction field including slotting effects in fractional-slot concentrated-coil spm multiphase machines,” in *Power Engineering, Energy and Electrical Drives (POWERENG), 2011 International Conference on*, May 2011, pp. 1–6. [101](#)
- [83] A. Tessarolo, “Analysis of split-phase electric machines with unequally-loaded stator windings and distorted phase currents,” in *Electrical Machines (ICEM), 2010 XIX International Conference on*, Sept 2010, pp. 1–7. [105](#), [110](#), [111](#)
- [84] R.-R. Moghaddam and F. Gyllensten, “Novel high-performance synrm design method: An easy approach for a complicated rotor topology,” *Industrial Electronics, IEEE Transactions on*, vol. 61, no. 9, pp. 5058–5065, Sept 2014. [106](#), [107](#)
- [85] J. M. Park, S. I. Kim, J.-P. Hong, and J.-H. Lee, “Rotor design on torque ripple reduction for a synchronous reluctance motor with concentrated winding using response surface methodology,” *Magnetics, IEEE Transactions on*, vol. 42, no. 10, pp. 3479–3481, Oct 2006. [106](#)
- [86] S. R. J.W. Nilsson, *Electric Circuits*, 9th ed. Prentice Hall, 2011. [106](#), [110](#)
- [87] P. Niazi, H. Toliyat, D.-H. Cheong, and J.-C. Kim, “A low-cost and efficient permanent-magnet-assisted synchronous reluctance motor drive,” *Industry Applications, IEEE Transactions on*, vol. 43, no. 2, pp. 542–550, March 2007. [107](#), [112](#)
- [88] J. Jackson, *Classical Electrodynamics*. New York: John Wiley and Sons, 1999. [113](#), [114](#)

List of Figures

1.1	(a) SynRel rotor with C-shaped barriers; (b) SynRel rotor with circular barriers; (c) example of SynRel motor with circular barriers.	14
1.2	Permanent Magnets price trend during the past decade.	16
1.3	Frame size versus efficiency and power density in SynRel motors.	17
1.4	Same stator size, different rotor type: loss reduction (note: stator copper losses slightly increase, and rotor losses are reduced to zero).	18
1.5	Magnetic flux trajectory according to the direct and quadrature axes in a 4 poles SynRel rotor configuration.	18
1.6	4 poles SynRel rotor prototype photos.	19
1.7	Magnetic d- and q-axes flux linkages as functions of I_d and I_q current respectively, in ideal and real cases.	20
2.1	MG0712, formula SAE car, year 2012, Race UP team, University of Padova, Italy. <i>Courtesy of Prof. Giovanni Meneghetti.</i>	22
2.2	IPM designs.	23
2.3	IPM machines: flux density map at rated load.	24
2.4	Performance comparison.	25
2.5	SPM designs.	27
2.6	SPM machines: flux density map at rated load.	28
2.7	Performance comparison.	29
2.8	EV power-train sketch overview.	29
2.9	Power converter efficiency map.	31
2.10	Batteries comparison.	31
3.1	Sketch of SynR and PMASynR motors equipped with three flux barriers per pole and different PM dimensions.	34
3.2	Current space vector trajectory: constant torque contour map.	36
3.3	Current and Torque vs. speed behavior.	36
3.4	Power and Power Factor vs. speed behavior.	37
4.1	Sketch of a four-pole synchronous reluctance rotor with three flux barriers per pole. The synchronous PM assisted reluctance motor is achieved when PMs are inset in the flux barriers.	40
4.2	Photo of a Machaon rotor lamination, characterized by the combination of two and three flux barriers per pole.	41
4.3	Layout of the variable parameters.	41

4.4	Torque versus rotor position: experimental results (continuous line) vs FE simulation (dashed line), motor B).	43
4.5	Ripple torque due to a variation of the flux barrier angles in the airgap region (motor A).	44
4.6	Torque ripple harmonics comparison due to a variation of ϑ_{b3} harmonic order refer to an electrical period, Motor A of Fig. 4.5	45
4.7	Torque ripple harmonics comparison due to a variation of ϑ_{b2} and ϑ_{b3} . Motor C, with symmetrical rotor.	45
4.8	Torque ripple harmonics comparison due to variation of the airgap. Harmonic content of ripple torque referred to an electrical period: different airgap considered (Motor C).	46
4.9	Percentage torque ripple (a) and average torque (b) as a function of the design variables ϑ_{b1} and ϑ_{b2} , with $\vartheta_{b3} = 38.8 \text{ deg}$ (Motor C).	47
4.10	Percentage torque ripple for different design variables: ϑ_{b2} and ϑ_{b3} with $\vartheta_{b1} = 14.8 \text{ deg}$ (Motor C).	48
4.11	Percentage torque ripple (a) average torque (b) as a function of the airgap and the iron ribs thicknesses (motor C).	48
4.12	Torque vs. rotor position behaviors before and after optimization (motor C): initial and final geometry.	49
4.13	Optimization direction of the flux barrier angles referring to the torque ripple (motor A).	50
4.14	Optimization direction of the flux barrier angles referring to the torque ripple (motor C).	50
4.15	Torque ripple vs distance for a symmetric configuration (motor A).	51
4.16	Torque ripple vs distance for a Machaon configuration (motor C).	51
4.17	Design vector centered in the hypercube space of the feasible solutions.	52
4.18	Torque ripple sensitivity versus the percentage torque ripple.	53
4.19	PM dimensions effect on torque ripple.	53
5.1	Driving cycle speed vs. time profiles.	56
5.2	Electromechanical characteristics.	57
5.3	PMASR motor prototype.	59
5.4	PMASR geometrical variables.	60
5.5	Optimization Process flow chart with MOGA-II.	62
5.6	Concept of the robustness for a 2 - objective functions design space.	63
5.7	Torque ripple distribution in UDDS and HWFET cycle.	63
5.8	Distance of the solution from the robustness locus in UDDS and HWFET cycles.	64
5.9	Mean torque ripple (blue squares) and losses (green points) trend of the most robust solutions.	65
6.1	Motor sketches.	69
6.2	Flux density maps at peak load operation.	70
6.3	Electromechanical performance.	73
6.4	Constant electrical losses loci in the torque-speed plane.	74
6.5	Constant electrical efficiency loci in the torque-speed plane.	75
6.6	LEV power-train sketch overview.	76

6.7	Constant inverter efficiency loci in the torque-speed plane.	77
7.1	Washing Machine Motor Technology.	80
7.2	Planned revision (second edition)	81
7.3	SynRel motor torque and power performance	82
7.4	Preliminary SynRel motor design.	83
7.5	SynRel torque ripple.	83
7.6	SynRel motor after optimization.	85
7.7	SynRel motor paramters (without considering the cross saturation).	85
7.8	SynRel motor paramters (considering the cross saturation).	86
7.9	Current space vector trajectory: constant torque (left) and speed (right) contour maps.	86
7.10	SynRel motor torque and power performance	87
7.11	PMASynRel motor: permanent magnet effect on torque ripple.	88
7.12	PMASynRel motor paramters (without considering the cross saturation).	88
7.13	PMASynRel motor paramters (considering the cross saturation).	89
7.14	Current space vector trajectory: constant torque (left) and speed (right) contour maps.	89
7.15	Phase current vs. speed.	90
7.16	PMASynRel motor torque and power performance	90
8.1	SynRel machine example rotor with two flux barriers per pole.	94
8.2	Magnetic circuit layout for a two-pole SynRel motor with two barriers per pole.	96
8.3	Complete reluctance network for a SynRel motor with two poles and two barrier per pole.	96
8.4	Reluctance network resulting from reduction of the circuit shown in Fig. 8.3.	97
8.5	Equivalent circuit from reduction of networks shown in Fig. 8.4.	97
8.6	Definition of angles x_r , x_1 and x_2	98
8.7	Conformal mapping transformation for a flux barrier.	99
8.8	Air-gap flux density computed by FEA and analytically for: (a) and (b): rotor position with q axis aligned with stator MMF axis; (c) and (d) with rotor q axis displaced by 15 mechanical degrees with respect to stator MMF axis. In (a), (c) slotting effects are not accounted for, while they are in (b) and (d).	102
8.9	Air-gap flux density computed by FEA and analytically for: (a) : rotor position with q axis aligned with stator MMF axis; (c) with rotor q axis displaced by 15 mechanical degrees with respect to stator MMF axis. Both results are including the slotting effects.	103
9.1	Phase arrangement and naming for a split-phase winding configuration with N three-phase sets.	106
9.2	Overall drive schematic for a split-phase motor with N independently fed stator sets.	107
9.3	Example of a four-pole dual-three-phase SynRel motor with two round barriers per pole. Phase arrangement over a pole span.	107
9.4	Characteristic geometric quantities for the i -th flux barrier.	108
9.5	Schematic of the SynRel MEC for a two-pole motor with two barriers per pole.	109

9.6	FEA simulation output for rotor position $xr=15^\circ$ and for (a) both winding sets energized; (b) only one winding set energized.	116
9.7	Air-gap flux density over a pole span, computed analytically and by FEA simulation for both windings energized with 50 A current.	117
9.8	Air-gap flux density over a pole span, computed analytically and by FEA simulation for unbalanced SynRel motor operation (one winding energized with 50 A current, the other at no load).	118